THE UNIVERSITY *of* EDINBURGH

Molecular Dynamics Modelling of Gas–Surface Interactions

Yichong Chen

Doctor of Philosophy

THE UNIVERSITY OF EDINBURGH

2024

Abstract

The advancement of engineering fluid flow systems operating at the micro/nanoscale, alongside the exploration of ultra-low vacuum environments, presents unprecedented challenges and opportunities in the field of rarefied gas dynamics. In such scenarios, gas flows are no longer in quasi-thermodynamic equilibrium, necessitating a shift to a modelling approach that goes beyond standard continuum fluid dynamics. The fluid behaviour must then be modelled using the Boltzmann equation or a kinetic model equation, supplemented by boundary conditions that model gas–surface interactions (GSIs). It is to these GSIs that one can trace the origin of the drag and lift exerted by gas on bodies and the heat transfer between gas and walls. Accordingly, GSIs determine the velocity slip and temperature jump at the surface, which are macroscopic manifestations of fluid non-equilibrium conditions and significantly influence the overall flow field. Furthermore, GSIs may be regarded as a bridge between the kinetic theory of gases and solid-state physics, accounting for the fluid flow inhomogeneity introduced by solid wall atoms. Despite this, the study of GSIs within the kinetic theory often needs a more direct connection with the properties of real walls. This thesis aims to bridge this gap, offering a detailed exploration of GSIs by considering the effects of surface characteristics like porosity, physisorption, and nanoscale roughness on gas scattering and transport phenomena. The use of soft, continuous Lennard-Jones fluids in molecular dynamics (MD) simulations enables the capture of the essential physics of real-world systems, providing a detailed insight into the complex interplay of gas and surface interactions.

The transport of gas inside organic/inorganic matter in underground geological reservoirs, important to shale extraction, introduces factors like porosity, adsorption, roughness, low-speed flows, elevated pressures and temperatures, differing significantly from the controllable metal surfaces typically investigated in GSI studies. This thesis begins with a systematic investigation of the scattering and transport process for methane molecules within a pore slit confined by two parallel walls composed of the organic matter called kerogen, found in shale. It is demonstrated that tight matrix porosities have a negligible effect on the timescale and lengthscale of the scattering process, consistent with the assumptions of conventional scattering kernels (SKs). Subsequently, the effectiveness of commonly used scattering models is evaluated by examining reflected velocity distributions. These evaluations indicate that although these models do not fully capture the scattering intricacies, especially at higher incident molecular speeds, the Maxwell model captures the observed scattered angular beam pattern and overall reflected velocity distribution most accurately. These aspects are more crucial for transport studies than merely modelling individual velocity component fluxes. Furthermore, a Maxwell model adjusted with a tangential momentum accommodation coefficient (TMAC) — nearing unity with increased

surface roughness up to approximately 2 nm — sufficiently predicts velocity profiles and mass flow rates in moderately confined kerogen mesopores. Discrepancies between the Maxwell model and MD simulations are noted only in cases of highly rarefied transport, which are outside the typical scope of shale reservoir applications.

Although it is widely recognised that there is a layer of physically adsorbed gas adjacent to surfaces, the development of scattering models that incorporate adsorption has received relatively little attention. Neglecting the presence of adsorbed molecules oversimplifies the complexity of scattering dynamics since impinging gas molecules interact not only with wall atoms, but also with other gas molecules next to the surface. To address this problem, a new SK has been developed that considers the influence of physisorption, which results from van der Waals interactions, on the dynamics of molecules impinging on solid, smooth surfaces. This SK is a linear combination of the Cercignani–Lampis (CL) and Maxwell fully diffuse models, with the Langmuir adsorption isotherm serving as a weighting factor. The rationale behind this model is that the CL component is designed to account for the scattering process from a clean, smooth surface in thermal equilibrium, while the fully diffuse component accurately describes gas–gas interactions within an adsorbed gas layer. This proposed scattering model successfully replicates observed molecular scattering patterns, along with the prediction of momentum and energy accommodation coefficients (ACs) in the entire range of explored conditions.

Another elusive aspect of GSIs originates from nanoscale surface roughness or irregularities, attributed to the height variation of wall atoms on the order of a few nanometres. Significant research efforts have been devoted to understanding how these irregularities impact scattering dynamics and rarefied gas transport, but the emphasis has been predominantly on oversimplified geometrical constructions and is thus not general. To include more detailed surface irregularities, a SK for surfaces possessing random roughness has been developed, using a similar technique as the adsorption SK. Here, a linear combination of the CL and Maxwell fully diffuse models is proposed. The weighting coefficient is derived by making an analogy between wave scattering near surfaces and gas–surface scattering, conceptualising random roughness as wave-like distortions on flat surfaces. The resulting SK enables a quantitative relationship between ACs, the gas scattering patterns and random surface roughness, revealing how the thermal motion of wall atoms and nanoscale roughness influence complex fluid behaviour in GSIs. The accuracy of various SKs has been evaluated through high-fidelity MD simulations. It is demonstrated that the newly proposed SK achieves the best agreement with benchmark MD simulations across the range of tested systems with varied roughness, temperature, and gas–surface combinations.

Altogether, these results provide a physically grounded understanding of GSIs as the boundary condition in kinetic theory. They have significant implications for modern technological applications, such as designing micro/nanofluidic devices, engineering systems in low vacuum environments, and CO_2 sequestration or hydrogen storage in underground reservoirs.

Lay Summary

Micro and nano-electro-mechanical systems (MEMS/NEMS) are miniature engineering marvels, underpinning many next-generation technologies in healthcare, environment sensors, and aerospace. These compact systems, found in our daily smartphones and life-saving medical devices, enhance our lives in countless ways. However, as we venture into engineering devices with geometries smaller than a grain of sand, we confront a perplexing challenge: the air and gases that flow through or around these tiny systems behave unexpectedly, revealing physical phenomena unfamiliar at macroscopic scales. This challenge extends beyond Earth into the low Earth orbits, where satellites and re-entry vehicles navigate through the thin veil of the atmosphere in extremely low-pressure conditions. Conventional gas flow principles falter in both these conditions, making it crucial to understand gas dynamics and demand new models to ensure these sophisticated technologies function correctly.

Despite all the unconventional gas flow behaviours, it may be surprising that accurate descriptions can often be obtained using elegant approximations. These simplified models, although idealised, have proven to be remarkably useful in many practical applications, as they capture the very essence of the processes at stake. In the case of rarefied gases, i.e., when confined or at low pressures as encountered in MEMS/NEMS and space technologies, the most general governing equation is the Boltzmann equation. This equation, which treats the many particles as points that move rapidly and collide very frequently with each other, allows us to model the motion of fluids at large scales, such as predicting the lift and drag around the space vehicles. Yet, how gases interact with the surfaces of these vehicles or nano-devices adds another layer of complexity. Just like a ball bouncing off a wall or a magnet sticking to a fridge, gas particles can bounce off, stick to, or even react with the surfaces they encounter. These interactions can change dramatically based on the texture and temperature of the surface and play a crucial role in accurately predicting how gases move. This intricate interplay between gas and surface, with its myriad possibilities and outcomes, presents a fascinating and challenging field of study.

This thesis focuses on the study of gas–surface interactions (GSIs). Specifically, it examines how gas molecules interact with impermeable walls with a well-defined geometrical boundary. Typically, the average velocity of gas at a solid surface is expected to match the velocity of the wall itself, which would become zero for a stationary wall. However, this does not hold for gases at very low pressures or very small scales, leading to the so-called velocity slip. This phenomenon can significantly enhance flow, especially in extreme cases like pressure-driven flow in nanotubes, where it can dominate the response to driving forces. Therefore,

understanding GSIs is essential from both scientific and practical perspectives. It challenges the applicability of long-held assumptions in fluid boundary conditions and opens up new avenues for research and application, particularly in the design and operation of nanoscale and low-vacuum devices.

Molecular dynamics (MD) simulations are used in this thesis to explicitly construct wall atoms and abstract the fundamental mechanisms of fluid behaviours, enabling the capture of the essential physics of real-world systems. MD simulations are virtual experiments used to mimic and observe how tiny particles, like atoms or molecules, move and interact with each other over time. MD simulations require substantial computational resources, often run on advanced supercomputers, and results are limited to the nano-realm in length and time. Yet, it is at this molecular scale that the intricacies of GSIs reveal themselves.

This thesis reveals how the physical nuances of molecular landscapes significantly influence GSIs. Through the application of MD simulations, it captures the fundamental physics of gas molecules interacting with solid surfaces in thermal equilibrium. A notable insight is the applicability of the Maxwell model for representing methane scattering behaviours and their transport processes near organic kerogen surfaces, which are markedly distinct from more predictable metal surfaces due to factors like porosity and roughness. Moreover, this thesis introduces refined scattering models that balance the effects of physically adsorbed gas molecules onto the surface and nanoscale surface irregularities, providing a closer match to real-world phenomena and improving gas flow predictions near surfaces. By incorporating realistic physics into scattering theories, this work simplifies the complexity of GSIs, paving the way for future research in rarefied flow transport.

Acknowledgements

This PhD journey has been both long and challenging, yet profoundly enriched and eased by the enthusiastic help and unwavering encouragement of many. The insightful knowledge and warm guidance I have received have illuminated my path and propelled me forward.

Firstly, my deepest appreciation goes to my principal supervisor, Matthew. I was fortunate to have met him through his lectures before commencing my postgraduate journey, where he consistently emphasised the importance of simplicity and clarity in imparting knowledge. This valuable principle followed me into my doctoral studies, where I was further inspired by his professional work ethic and genuine care for his students. Equally, my sincere thanks extend to my second supervisor, Livio, who generously devoted his time to discussions, weekly meetings, and constructive criticism. He shared his exceptional academic skills, experience, and passion for research, all of which have been a continuous source of inspiration and motivation. The invaluable lessons and experiences I've gained from them, extending even to interpersonal interactions, are treasures that will enrich my journey through life.

Secondly, I express my heartfelt thanks to my friends and colleagues, in the Multiscale Flow X group, at IMT and beyond. Despite being an introvert with a self-professed lack of knack for small talk, I've been continually uplifted by their warmth and kindness. The moments we've shared, from hangouts to sports activities, have created some of my most cherished memories of Edinburgh.

Last but not least, I want to extend my deepest gratitude to my family and close friends back home, especially my parents, for their unwavering emotional and financial support over the years. They have created an environment that allows me to focus on my pursuits without distractions. In the same vein, my thanks go to my partner, who is pursuing her PhD in a different field. Together, we have navigated countless challenges and shared myriad joys in this foreign land; experiences that constantly remind me that the life journey extends well beyond the office, into a world filled with wonders.

Declaration

I declare that this thesis was composed by myself, that the work contained herein is my own except where explicitly stated otherwise in the text, and that this work has not been submitted for any other degree or professional qualification except as specified.

Yichong Chen

Contents

Figures and Tables

Figures

Tables

Chapter 1

Introduction

1.1 Non-equilibrium Gas Flow in Engineering

In his visionary 1959 lecture, "There's Plenty of Room at the Bottom", Richard Feynman predicted the dramatic miniaturisation that underpins contemporary technological progress. This prediction has come to fruition with the widespread development of micro-/nano-electro-mechanical systems (MEMS/NEMS), showcasing complex engineering on a tiny scale. These systems find applications in various fields, from micro-heat exchangers that enhance electronic cooling to micropumps facilitating precise drug delivery and accelerometers used in vehicle airbags. However, the rapid advancements in MEMS/NEMS have not been matched by our understanding of the unconventional physics that governs these devices. This discrepancy becomes particularly evident upon examining their flow dynamics (Gad-el Hak, 1999; Karniadakis, Beskok & Aluru, 2005), where gas molecules typically lack the time necessary to adjust and settle into a homogeneous and stable state, a consequence of extreme spatial confinement. Such a condition implies the breakdown of local quasi-thermodynamic equilibrium and leads to complex gas flow behaviours, which traditional models fail to capture adequately. Central to this discussion is the flow characteristic length L, which often represents the smallest length dimension of a physical system. It is along this dimension that the gradients of macroscopic quantities become most pronounced, underscoring the need for a refined modelling approach to micro/nanoscale flow phenomena.

Simultaneously, technological progress has propelled us into realms of ultra-low vacuum conditions, notably in satellite technology encountered in very low Earth orbits. From the basic capabilities of Russia's Sputnik 1 to the complex functionalities of modern satellites in meteorology, telecommunications, and global surveillance, it is clear that satellites have significantly transformed societal operations. These advancements also prompt a reevaluation of traditional fluid dynamics principles, as in vacuum pressures, gas particles travel significant distances between collisions, again challenging the establishment of a homogeneous and stable state of fluid flows. Central to this analysis is the mean free path λ, defined as the average distance a particle travels between successive collisions, which becomes a critical factor in modelling gas transport and aerodynamic phenomena under such extreme physical conditions.

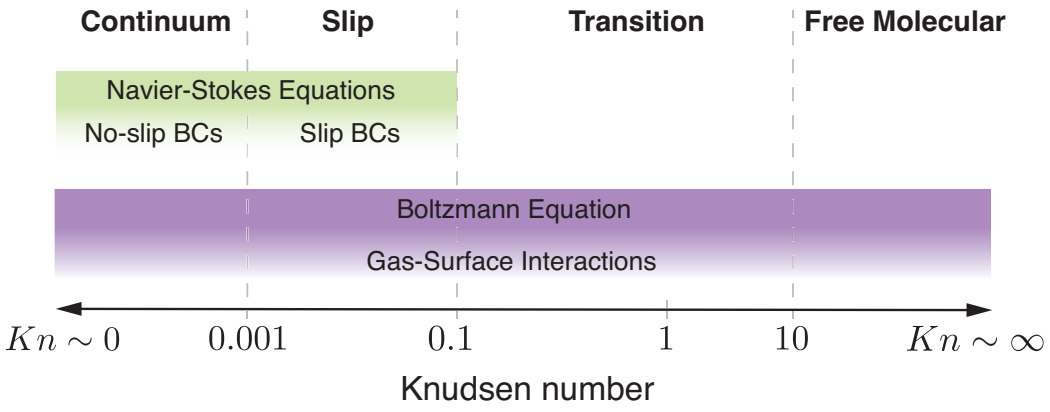

Figure 1.1: Classification of flow regimes based on the Knudsen number.

1.2 Flow Regimes Classification

In the engineering flow systems under discussion, deviations from local equilibrium are primarily attributed to the relative infrequency of particle collisions compared to the relevant time and length scales of the flow. The extent of these non-equilibrium phenomena thus can be quantified by the ratio of the mean free path λ to the characteristic length scale of the flow L, leading to the definition of an important dimensionless parameter, the Knudsen number:

$$Kn = \frac{\lambda}{L}. \tag{1.1}$$

The Knudsen number is pivotal in classifying gas flows into distinct regimes, as illustrated in Fig. 1.1. In the continuum regime, where $Kn \lesssim 0.001$, frequent particle collisions ensure homogeneity within each fluid element, maintaining local thermodynamic equilibrium. In this context, the gas is treated as a continuum, and the flow is effectively described by traditional Navier–Stokes hydrodynamics, complemented by no-slip boundary conditions (BCs). In the slip flow regime ($0.001 \lesssim Kn \lesssim 0.1$), the gas becomes slightly rarefied, allowing for slippage along confining surfaces. This necessitates a shift from the no-slip to a slip boundary condition, with the effectiveness of the slip-flow model diminishing as Kn increases. Typically, $Kn \approx 0.1$ is considered the upper limit for its valid application, although the actual threshold varies based on the acceptable error margin. In smaller-scale systems or more dilute conditions, Navier–Stokes descriptions become inadequate, necessitating a kinetic approach rooted in the molecular perspective. This approach typically involves solving the Boltzmann equation or a kinetic model equation in the transition regime ($0.1 \lesssim Kn \lesssim 10$), or approximating transport as ballistic in the free molecular regime ($Kn \gtrsim 10$), all while incorporating boundary conditions that model gas–surface interactions (GSIs).

The kinetic approach delivers a comprehensive description across the entire range of Kn, effectively bridging the gap between broad hydrodynamic theories and the intricate realm of molecular interactions. The transition from the Boltzmann equation to Navier–Stokes descriptions is elegantly demonstrated via the well-known Chapman–Enskog expansion (Cercignani, 1988; Chapman & Cowling, 1952; Vincenti & Kruger, 1965). This expansion, however, assumes the bulk of the gas to be infinite and thus offers no insight into gas behaviour at boundaries. The emergence of slip boundary conditions marks a stride towards recognising the complexities at the interface, and necessitates a separate treatment. These conditions can be rigorously derived using asymptotic analysis for $Kn \ll 1$ (Sone, 2007), where the system is large enough for the Navier–Stokes description to remain valid in the bulk of the domain, with boundary presence treated as a perturbation to this solution.

1.3 Boundary Conditions and Gas–Surface Interactions (GSIs)

In formulating kinetic problems involving gases and solid bodies, it is required to specify boundary conditions for the Boltzmann equation or a kinetic model equation, necessitating an understanding of gas molecular behaviours upon impinging with the wall. As the rarefaction of gas increases, the significance of interactions between gas molecules and wall atoms becomes more pronounced. In the free molecular regime, the behaviour of gas flows is almost exclusively governed by these GSIs. Additionally, this understanding is crucial for refining hydrodynamic slip models, where challenges at boundaries can be traced to detailed molecular physics, including GSIs and gas–gas interactions (Hadjiconstantinou, 2024).

The first observations of gas interactions with solid surfaces can be attributed to Kundt and Warburg (1875), who noted that the mass flow rate through tubes at very low pressures was significantly higher than the values predicted by the well-known Poiseuille formula. This discrepancy was attributed to a slip at the boundary, a discrepancy between the tangential velocity of the flow and the velocity of the solid surface in contact. Following this, Maxwell (1879) suggested that such slip could result from the dynamics of gas molecules upon impinging the wall. He boldly assumed the absence of intermolecular collisions in a thin region next to the surface, and computed the amount of slip based on a conceptualised model of GSIs. This model, alongside the derived slip boundary condition, remains very popular and bears his name. Serving as the thermal analogue to the velocity slip, the temperature jump was similarly characterised by Smoluchowski (1898). The thin region, spanning a few mean free paths and containing all non-equilibrium effects induced by the surface, became known as the Knudsen layer, named after a more systematic exploration of boundary effects that started with Knudsen (1934). Comprehensive research in this field (see Section 2.2), however, only gained momentum in the late 1960s, closely associated with the advancements of aforementioned MEMS/NEMS and space technologies.

Being pivotal in boundary effects, GSIs also serve as a bridge between the kinetic theory of gases and solid-state physics (Cercignani, 1988; Kuščer, 1978). The complexity of GSIs primarily arises from solid-state physics, mainly due to our limited understanding of the interaction potential between gas molecules and the wall. This lack of clarity extends to the structures of surface layers, which contain all the surface-induced inhomogeneities. When a molecule collides with a surface, it may undergo various processes, including direct scattering, adsorption, chemical reaction, dissociation, ionisation, or even sputtering, which results in the displacement of surface atoms. These processes are naturally influenced by the surface finish, cleanliness, and temperature, with temporal changes from outgassing and the cleansing effect of preheating—emitting previously adsorbed molecules—adding extra complexities (Billing, 2000; Kuščer, 1978). Moreover, the presence of adsorbed layers means the interaction can also depend on the distribution of impinging molecules on a given surface element. This sophistication of wall physics stands in stark contrast with the relatively simple boundary conditions currently in use, highlighting the need for advanced models that capture the intricate physics of GSIs (Aoki, Giovangigli, Golse & Kosuge, 2024; Aoki, Giovangigli & Kosuge, 2022). The noticeable impact on slip when modifying the GSI model emphasises this requirement (Sharipov, 2003), urging the development and integration of more sophisticated models within the framework of kinetic theory.

1.4 Thesis Outline

The remaining chapters of the thesis are as follows:

Chapter 2 — **Theoretical Background** provides an overview of GSIs, introducing various frameworks for their exploration. It begins with GSIs within kinetic theory, emphasising fundamental concepts such as scattering kernels (SKs) and accommodation coefficients (ACs), followed by a review of kinetic treatments near surfaces. The chapter subsequently delves into the phenomenological aspects of GSIs, elucidating the impact of wall physics on these interactions.

Chapter 3 — **Molecular Dynamics for Modelling GSIs** introduces molecular dynamics (MD) as the primary simulation approach for this research. It details the scattering experiment setup that was adopted in this work, including strategies to maintain the system within the desired regime and techniques for analysing molecular motions near surfaces.

Chapter 4 — **Methane Scattering and Mesopore Transport on Porous Kerogen Surfaces** presents original research, carrying out the first scattering study on porous and rough kerogen surfaces, with application to shale reservoir modelling. The findings of this work reveal that porosity in large nanochannels negligibly impacts the residence time and displacement of

re-emitted methane molecules, supporting the use of conventional SKs for shale reservoirs. Moreover, although common SKs have difficulty in fully capturing scattering behaviours, the Maxwell model best captures observed overall reflection patterns and effectively predicts macroscopic transport properties.

Chapter 5 — **On the Impact of Surface Physisorption** presents new research on the role of surface physisorption in scattering dynamics and its integration into conventional SKs. Initially, MD simulations confirm the density dependence of scattering dynamics, closely correlating with adsorption isotherms. A new SK is then formulated, factoring in physisorption effects from van der Waals interactions on the behaviour of molecules interacting with smooth surfaces in thermal equilibrium.

Chapter 6 — **On the Impact of Random Nanoscale Roughness** is the final chapter presenting new results. It clarifies the relationship between ACs and surface roughness, examining how random nanoscale roughness affects scattering dynamics. An analogy between wave–surface and gas–surface scattering is drawn in this work, likening rough surface to thermal motion-induced deviations of wall atoms of a smooth surface. A new SK is proposed to include the effect of roughness on gas scattering, attributed to the height variation of wall atoms at the nanoscale, on the behaviour of molecules interacting with surfaces at thermal equilibrium.

Chapter 7 — **Concluding Remarks** summarises the main findings and discusses several avenues for continuing the work initiated in this thesis, proposing research directions that may be of interest for future investigation.

Chapter 2

Theoretical Background

This chapter provides an overview of the theoretical background and classical models for the characterisation of GSIs. Section 2.1 introduces the elementary concepts of the kinetic theory of gases. In Section 2.2, GSIs are presented within the framework of kinetic theory. This includes an analytical manner, which utilises SKs with adjustable ACs, alongside a concise review of how transport equations are employed to describe scattering dynamics. Finally, Section 2.3 shifts focus to the phenomenological aspects of GSIs, grounded in solid-state physics, which shed light on the inherent properties of GSIs.

2.1 Elementary Kinetic Theory of Gases

The kinetic theory of gases provides a framework for understanding gaseous behaviour from a molecular standpoint. To maintain brevity of this thesis, the discussion from here onward is limited to single, monatomic particle species. For further information on kinetic theory, readers are directed to key textbooks (Bird, 1994; Cercignani, 1988, 2000; Chapman & Cowling, 1952; Kogan, 1969; Kremer, 2010; Sharipov, 2015; C. Shen, 2006; Sone, 2007; Struchtrup, 2005).

2.1.1 Distribution Function and Basic Quantities

Even in ultra-high vacuum conditions within a confined space, a considerable number of interacting gas particles remain. Every particle is characterised by its spatial position, denoted by $\boldsymbol{r}$, and velocity $\boldsymbol{\xi}$, at any specific time t. While solving the equations of motion to capture the deterministic motion of every particle is essential for understanding the behaviour of molecular flows, it often becomes more practical to describe the macroscopic properties through a statistical approach to the microscopic variables. To this end, a particle distribution function, also called a phase density, $f(\boldsymbol{r},\boldsymbol{\xi},t)$, is defined such that:

$$N_{\boldsymbol{r},\boldsymbol{\xi},t} = f(\boldsymbol{r},\boldsymbol{\xi},t)\mathrm{d}\boldsymbol{r}\mathrm{d}\boldsymbol{\xi}. \tag{2.1}$$

Eq. (2.1) quantifies the number of particles $N_{\boldsymbol{r},\boldsymbol{\xi},t}$ that are located in the interval $[\boldsymbol{r}+\mathrm{d}\boldsymbol{r}]$ within a small velocity range $[\boldsymbol{\xi}+\mathrm{d}\boldsymbol{\xi}]$ at time t. Notably, this definition assumes not only a large number of particles, but also the absence of correlation between their movements, implying that the particles move independently of one another at practically all times.

The distribution function $f(\boldsymbol{r},\boldsymbol{\xi},t)$ is the cornerstone of kinetic theory, encapsulating intricate microscopic details about a gas. Macroscopic quantities can be calculated by taking velocity-weighted moments of the distribution function, such as number density n, mean velocity of the gas $\boldsymbol{u}$, and temperature T of common interest:

$$n(\boldsymbol{r},t) = \int f(\boldsymbol{r},\boldsymbol{\xi},t)\mathrm{d}\boldsymbol{\xi}, \tag{2.2a}$$

$$\boldsymbol{u}(\boldsymbol{r},t) = \frac{1}{n(\boldsymbol{r},t)}\int \boldsymbol{\xi} f(\boldsymbol{r},\boldsymbol{\xi},t)\mathrm{d}\boldsymbol{\xi}, \tag{2.2b}$$

$$T(\boldsymbol{r},t) = \frac{m}{3k_B n(\boldsymbol{r},t)}\int \boldsymbol{c}^2 f(\boldsymbol{r},\boldsymbol{\xi},t)\mathrm{d}\boldsymbol{\xi}, \tag{2.2c}$$

where m signifies the particle mass and k_B the Boltzmann constant. It is conventional to decompose the microscopic particle velocity $\boldsymbol{\xi}$ into the mean velocity $\boldsymbol{u}$ and a thermal velocity component $\boldsymbol{c} = \boldsymbol{\xi} - \boldsymbol{u}$, also referred to as a peculiar velocity. This decomposition is often employed to evaluate other macroscopic quantities like the pressure tensor and heat flux density due to thermal agitation:

$$p_{ij} = m\int c_i c_j f(\boldsymbol{r},\boldsymbol{\xi},t)\mathrm{d}\boldsymbol{\xi} = p\delta_{ij} + \sigma_{ij}, \tag{2.2d}$$

$$q_i = \frac{m}{2}\int \boldsymbol{c}^2 c_i f(\boldsymbol{r},\boldsymbol{\xi},t)\mathrm{d}\boldsymbol{\xi}, \tag{2.2e}$$

where the indices $i, j \in \{1,2,3\}$ correspond to components of thermal (peculiar) velocity, δ_{ij} is the Kronecker delta and σ_{ij} is the stress tensor.

2.1.2 The Boltzmann Equation and Kinetic Models

The central objective of kinetic theory is to determine $f(\boldsymbol{r},\boldsymbol{\xi},t)$ for a given problem, enabling the calculation of macroscopic quantities as described earlier. However, this is generally a challenging undertaking, as the evolution of f is governed not just by the free flight of particles but also by collisions among them, leading to an exchange of momentum and energy. The equation that comprehensively accounts for these dynamics was first formulated by Boltzmann (1872) and is named eponymously. To derive the Boltzmann equation, several assumptions are made (Kremer, 2010):

- The probability of binary collisions is significantly greater than that of collisions involving more than two molecules.

- The effect of external forces on molecules during the mean free time, that is, the average time interval between collisions, is negligible when compared to the impact of intermolecular forces.
- The velocities and positions of two asymptotic molecules, as well as those of their post-collisional pair, are uncorrelated, a premise known as the *molecular chaos hypothesis*.

The Boltzmann equation reads (Cercignani, 1988; Struchtrup, 2005):

$$\underbrace{\frac{\partial f}{\partial t}}_{\text{change in time}} + \underbrace{\boldsymbol{\xi}\cdot\frac{\partial f}{\partial \boldsymbol{r}}}_{\text{free flight of particles}} + \underbrace{\frac{\boldsymbol{F}}{m}\cdot\frac{\partial f}{\partial \boldsymbol{\xi}}}_{\text{acceleration due to external forces } \boldsymbol{F}} = \underbrace{Q_{\text{Boltz}}(f,f)}_{\text{change due to collisions}} , \tag{2.3}$$

which is a non-linear integro-differential equation for the evolution of f in space and time. Its left-hand side describes free molecular transport of particles and acceleration due to non-self-consistent external forces $\boldsymbol{F}$ exerted per molecule, such as gravitational forces. In the case where molecular interactions are governed by weak, long-range forces, the influence of $\boldsymbol{F}$ can be encapsulated by the so-called Vlasov term (Cercignani, 1988):

$$\int n(\boldsymbol{r}_*,t)\boldsymbol{X}(\boldsymbol{r}_*,\boldsymbol{r})\mathrm{d}\boldsymbol{r}_*\cdot\frac{\partial f}{\partial \boldsymbol{\xi}}. \tag{2.4}$$

Here, $\boldsymbol{X}(\boldsymbol{r}_*,\boldsymbol{r})$ denotes the long-range force (per unit mass) exerted by a representative molecule of the interaction partner at position $\boldsymbol{r}_*$, upon on a gas molecule at position $\boldsymbol{r}$ with velocity $\boldsymbol{\xi}$, and $n(\boldsymbol{r}_*,t)$ is the number density of the interaction partner in physical space.

In a typical rarefied gas, however, molecular interactions become rather strong when molecules are in close proximity, which forms the basis for deriving the Boltzmann equation. This situation makes the collision operator Q_{Boltz}, which accounts for the effects of intermolecular collisions on f, a more significant descriptor than a term based on continuous, weak forces (Cercignani, 1988). The non-linear collision operator Q_{Boltz} reads (Chapman & Cowling, 1952; Sharipov, 2015):

$$Q_{\text{Boltz}}(f,f) = \int\int\int (f\, f_* - f'\, f'_*)\mathscr{W}(\boldsymbol{\xi},\boldsymbol{\xi}_*;\boldsymbol{\xi}',\boldsymbol{\xi}'_*)\mathrm{d}\boldsymbol{\xi}'_*\mathrm{d}\boldsymbol{\xi}\mathrm{d}\boldsymbol{\xi}_*. \tag{2.5}$$

Here, $\boldsymbol{\xi}_*$ denotes the velocity of the collision partner, $f'(\boldsymbol{\xi},\boldsymbol{r},t)$ and $f'_*(\boldsymbol{\xi},\boldsymbol{r},t)$ are the pre-collision distribution functions, f and f_* the post-collision distribution functions. The transition probability $\mathscr{W}(\boldsymbol{\xi},\boldsymbol{\xi}_*;\boldsymbol{\xi}',\boldsymbol{\xi}'_*)$ is determined by the intermolecular potential, and its dependence on $\{\boldsymbol{r},t\}$ has been left implicitly. If only binary collisions are considered, $\mathscr{W}$ adheres to the reciprocity relation $\mathscr{W}(\boldsymbol{\xi}',\boldsymbol{\xi}'_*;\boldsymbol{\xi},\boldsymbol{\xi}_*) = \mathscr{W}(-\boldsymbol{\xi},-\boldsymbol{\xi}_*;-\boldsymbol{\xi}',-\boldsymbol{\xi}'_*)$ associated with microreversibility (Sharipov, 2015).

The Boltzmann collision operator fulfils several fundamental properties:

$$\int \varphi \, Q_{\text{Boltz}}(f,f) \, \mathrm{d}\boldsymbol{\xi} = 0 \text{ for any } f \text{ when } \varphi \in \left\{1, \boldsymbol{\xi}, \boldsymbol{\xi}^2\right\}, \tag{2.6a}$$

$$\int \log f \, Q_{\text{Boltz}}(f,f) \, \mathrm{d}\boldsymbol{\xi} \leq 0 \text{ for the space-homogeneous case}, \tag{2.6b}$$

$$Q_{\text{Boltz}}(f,f) = 0 \Longleftrightarrow f = f^{\text{M}}. \tag{2.6c}$$

Eq. (2.6a) is directly related to the conservation of mass, momentum and energy — the so-called collision invariants in elastic particle collisions. Eq. (2.6b) stands as the *Boltzmann inequality*, further implies the $\mathscr{H}$-theorem in the case of space-homogeneous, which physically expresses the fact that entropy production is strictly non-negative (Cercignani, 1988, 2000). The equality in Eq. (2.6b) holds if and only if f is in equilibrium — a state where no changes will occur when the gas is left undisturbed. Moreover, Eq. (2.6c) ensures that the local equilibrium condition will not be influenced by molecular collisions, which is generally observed in continuum flows, i.e., when the Knudsen number approaches zero, and the corresponding local Maxwellian distribution reads:

$$f^{\text{M}}(\boldsymbol{r},\boldsymbol{\xi},t) = \frac{n(\boldsymbol{r},t)}{[2\pi RT(\boldsymbol{r},t)]^{3/2}} \exp\left\{ - \frac{[\boldsymbol{\xi} - \boldsymbol{u}(\boldsymbol{r},t)]^2}{2RT(\boldsymbol{r},t)} \right\}, \tag{2.7}$$

where $R = k_B/m$ is the specific gas constant.

Although the Boltzmann equation is valid for all Knudsen numbers due to its detailed microscopic characterisation, the exact/direct solution of the collisional integral Q_{Boltz} presents considerable computational challenges. As a result, simplified alternatives, known as collision models, have been utilised to approximate the qualitative and average properties of Q_{Boltz}.

The so-called BGK model, proposed independently by Bhatnagar, Gross and Krook (1954) and Welander (1954), serves as the cornerstone for the development of collision models. This model posits a straightforward relaxation behaviour: the rate of change of the distribution function $f(\boldsymbol{r},\boldsymbol{\xi},t)$ is proportional to its deviation from the local Maxwellian distribution f^{M}. Mathematically, this implies that the exact collision integral, Eq. (2.5), is substituted with:

$$Q_{\text{BGK}} = -\frac{f - f^{\text{M}}}{\tau_{\text{BGK}}}, \tag{2.8}$$

where f^{M} encapsulates local values of number density n, temperature T and bulk velocity $\boldsymbol{u}$ that are computed via the distribution function $f(\boldsymbol{r},\boldsymbol{\xi},t)$, and the relaxation time τ_{BGK} is of the order of the mean free time.

Instead of aiming to approximate the non-linear behaviour of Q_{Boltz}, particle interactions can also be treated as independent and linear in specific contexts, such as neutron transport, radioactive transfer and GSIs (Cercignani, 1988). This simplification leads to the linear Boltzmann equation that features the case of a two-component mixture, where collisions within a low dens-

ity species N are negligible compared to those within the high density species, M. Furthermore, collisions involving M dominate, rendering the state of N inconsequential to M's evolution. In other words, the linear Boltzmann equation describes the evolution of f (for species N) that does not incorporate the interactions between particles, but only with a given background medium, and the collision integral for species N reads (Cercignani, 1972):

$$Q_{\text{Linear Boltz}} = \int \mathscr{K}(\boldsymbol{\xi}' \to \boldsymbol{\xi}) f(\boldsymbol{\xi}') \mathrm{d}\boldsymbol{\xi}' - \int \mathscr{K}(\boldsymbol{\xi} \to \boldsymbol{\xi}') \mathrm{d}\boldsymbol{\xi}' f(\boldsymbol{\xi}). \tag{2.9}$$

In this context, $\mathscr{K}(\boldsymbol{\xi}' \to \boldsymbol{\xi})$ is a volume kernel function and satisfies the reciprocity relation (Cercignani, 1988) that is analogous to the property that will be discussed in Section 2.2.1.

In contrast to Q_{Boltz}, which models two-body collisions using a cutoff intermolecular potential, another model accounts for grazing collisions through multiple non-cutoff potentials. This model, statistically addressing the resultant continuous and quasi-random velocity variations, is embodied in the Fokker–Planck (FP) collision term. As proposed by J. Lebowitz, Frisch and Helfand (1960), this integro-differential FP term is similar to the equation used in the theory of Brownian motion (Kuščer, Mozina & Krizamič, 1971). It approximates the impact of particle collisions by simulating diffusive processes in phase space. Specifically, the FP term includes diffusion and friction components, capturing the many simultaneous deflections behaviour of particles and their tendency towards relaxation to a steady-state or equilibrium distribution. This term can be written as (Cercignani, 1972, 1988, 2000; Kuščer et al., 1971):

$$Q_{\text{FP}} = \sum_{i,j=1}^{3} \left[\frac{\partial}{\partial \xi_i} \left(D_{ij} \frac{\partial f}{\partial \xi_i} \right) + \frac{\partial}{\partial \xi_i} (F_{ij} \xi_i f) \right], \tag{2.10}$$

where D_{ij} and F_{ij} are the diffusion and friction tensors in velocity space.

2.2 GSIs — Under the Framework of Kinetic Theory

2.2.1 GSIs and Their Properties

The Boltzmann equation or its kinetic model necessitates boundary conditions characterised by GSIs. It is to these interactions that one can trace the origin of velocity slip and temperature jump at the surface — macroscopic manifestations of fluid non-equilibrium conditions that significantly influence the overall flow field.

In general, determining the behaviour of a gas molecule upon surface impact requires precise calculations of its trajectory near/within the wall. However, this is a complex task depending on various factors, such as the positions and speeds of wall atoms and an accurate understanding of the interaction potential. It is, therefore, more practical to conceptualise these GSIs as a probabilistic event and formulate them via the so-called scattering kernel (SK), which establishes a connection between the incident and reflected molecular fluxes at the surface.

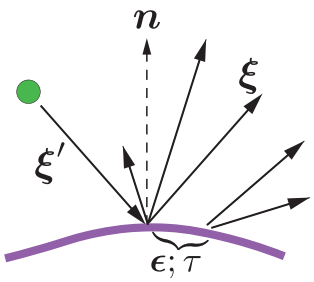

Figure 2.1: A schematic illustrating the surface scattering process. Notably, the velocity $\boldsymbol{\xi}$ of a molecule upon reflection is not strictly determined by the velocity it held prior to colliding with the wall. Moreover, a slight displacement $\boldsymbol{\epsilon}$, and a residence time τ may be observed during the scattering process.

The SK, $\mathscr{R}(\boldsymbol{\xi}' \to \boldsymbol{\xi}; \boldsymbol{r}, t; \boldsymbol{\epsilon}, \tau)$, provides the probability density of a gas molecule striking the surface at a given location $\boldsymbol{r} - \boldsymbol{\epsilon}$ and time $t - \tau$, with a velocity range of $[\boldsymbol{\xi}', \boldsymbol{\xi}' + \mathrm{d}\boldsymbol{\xi}']$, and subsequently rebounding from the surface at location $\boldsymbol{r}$ and time t, within a velocity range of $[\boldsymbol{\xi}, \boldsymbol{\xi} + \mathrm{d}\boldsymbol{\xi}]$, where $\boldsymbol{\epsilon}$ symbolises the displacement and τ indicates the residence time (Cercignani, 1988). The equation that relates the incident $f(\boldsymbol{\xi}', \boldsymbol{r} - \boldsymbol{\epsilon}, t - \tau)$ and reflected $f(\boldsymbol{\xi}, \boldsymbol{r}, t)$ distribution functions can be obtained through a mass balance at the surface (Cercignani, 1969), leading to:

$$\xi_n f(\boldsymbol{\xi}, \boldsymbol{r}, t) = \int_{-\infty}^{\infty} \mathrm{d}\boldsymbol{\epsilon} \int_{0}^{\infty} \mathrm{d}\tau \int_{\boldsymbol{\xi}_n' < 0} |\xi_n'| \mathscr{R}(\boldsymbol{\xi}' \to \boldsymbol{\xi}; \boldsymbol{r}, t; \boldsymbol{\epsilon}, \tau) f(\boldsymbol{\xi}', \boldsymbol{r} - \boldsymbol{\epsilon}, t - \tau) \mathrm{d}\boldsymbol{\xi}', \tag{2.11}$$

where $\xi_n = \boldsymbol{\xi} \cdot \boldsymbol{n} > 0$ with $\boldsymbol{n}$ being the unit vector normal to the surface pointing into the gas phase (as seen in Fig. 2.1). This equation is regarded as a linear integral transformation acting upon functions defined in the velocity half space, and usually represents the boundary condition for gas kinetic problems.

A general SK involves information on both the local wall temperature T_w and the wall velocity $\boldsymbol{u}_w$, while this thesis will focus solely on walls at rest, i.e., where $\boldsymbol{u}_w = 0$. More importantly, a general SK, $\mathscr{R}(\boldsymbol{\xi}' \to \boldsymbol{\xi}; \boldsymbol{r}, t; \boldsymbol{\epsilon}, \tau)$, must satisfy the basic properties of

(i) Positiveness; that is, $\mathscr{R}$ being a probability density function, cannot take negative values:

$$\mathscr{R}(\boldsymbol{\xi}' \to \boldsymbol{\xi}; \boldsymbol{r}, t; \boldsymbol{\epsilon}, \tau) \geq 0. \tag{2.12}$$

(ii) Normalisation; if the surface is impermeable and permanent adsorption is excluded:

$$\int_{-\infty}^{\infty} d\boldsymbol{\epsilon} \int_{0}^{\infty} d\tau \int_{\xi_n > 0} \mathscr{R}(\boldsymbol{\xi}' \to \boldsymbol{\xi}; \boldsymbol{r}, t; \boldsymbol{\epsilon}, \tau) \mathrm{d}\boldsymbol{\xi} = 1, \tag{2.13}$$

indicating that the normal component of the bulk velocity of the gas vanishes at the wall.

(iii) Reciprocity; it implies that microscopic scattering dynamics are time-reversible, and the surface is assumed to be in a state of local equilibrium, undisturbed by the impinging molecules (Cercignani, 1988; Kuščer, 1971). Specifically, the number of molecules scattered from a velocity range $[\boldsymbol{\xi}', \boldsymbol{\xi}' + \mathrm{d}\boldsymbol{\xi}']$ to $[\boldsymbol{\xi}, \boldsymbol{\xi} + \mathrm{d}\boldsymbol{\xi}]$ (per unit area and unit time) is equal to the number of molecules scattered from $[-\boldsymbol{\xi}, -\boldsymbol{\xi} - \mathrm{d}\boldsymbol{\xi}]$ to $[-\boldsymbol{\xi}', -\boldsymbol{\xi}' - \mathrm{d}\boldsymbol{\xi}']$:

$$|\xi_n'| f_w(\boldsymbol{\xi}') \mathscr{R}(\boldsymbol{\xi}' \to \boldsymbol{\xi}; \boldsymbol{r}, t; \epsilon, \tau) = |\xi_n| f_w(\boldsymbol{\xi}) \mathscr{R}(-\boldsymbol{\xi} \to -\boldsymbol{\xi}'; \boldsymbol{r}, t; \epsilon, \tau), \tag{2.14}$$

where $f_w(\boldsymbol{\xi})$ is the non-drifting Maxwellian distribution having the temperature of the wall:

$$f_w(\boldsymbol{\xi}) = \frac{1}{2\pi (RT_w)^2} \exp\left\{ -\frac{\boldsymbol{\xi}^2}{2RT_w} \right\}. \tag{2.15}$$

A consequence of reciprocity, together with the use of normalisation, Eq. (2.13), imply another property known as preservation of equilibrium/Maxwellian:

$$|\xi_n| f_w(\boldsymbol{\xi}) = \int_{-\infty}^{\infty} \mathrm{d}\epsilon \int_0^{\infty} \mathrm{d}\tau \int_{\xi_n' < 0} |\xi_n'| \mathscr{R}(\boldsymbol{\xi}' \to \boldsymbol{\xi}; \boldsymbol{r}, t; \epsilon, \tau) f_w(\boldsymbol{\xi}') \mathrm{d}\boldsymbol{\xi}'. \tag{2.16}$$

However, reciprocity is not necessary for the preservation of the Maxwellian, i.e., Eq. (2.14) is more restrictive than Eq. (2.16). For instance, if we consider the bulk of the solid as a heat bath, non-equilibrium phenomena due to small perturbations, such as slow drifts and slight temperature differences, may still occur within a thin layer near the surface. This situation could indicate the failure of reciprocity while preserving the Maxwellian distribution. A detailed discussion on the conditions under which reciprocity becomes invalid, including factors like low surface temperatures and electronic excitation and relaxation in metals, is provided by Bärwinkel and Schippers (1989).

Transitioning from general to conventional SKs requires two further assumptions (Cercignani, 1988):

- The displacement ϵ and effective adsorption time τ during the scattering are typically small compared to the mean free path and characteristic time of gas molecules in bulk collisions. In other words, τ is negligible relative to any relevant time scales in the evolution of f, which is particularly valid for steady flow problems.
- Even though gas molecules could disturb the single atoms of the wall, these atoms are considered to be in local thermal equilibrium at a temperature T_w. This temperature may exhibit macroscopic variations across the system. $\mathscr{R}(\boldsymbol{\xi}' \to \boldsymbol{\xi})$ hence depends solely on T_w and the chemical composition of the wall, eliminating the need to include $\boldsymbol{r}$ and t as arguments.

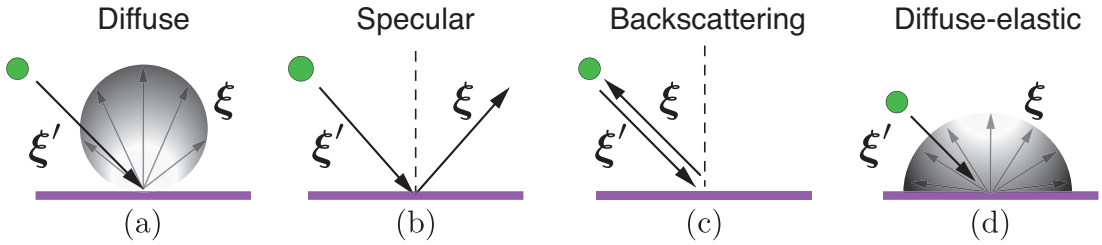

Figure 2.2: Schematics illustrating elementary gas molecule scattering patterns: (a) diffuse scattering; (b) specular reflection; (c) perfect backscattering; (d) diffuse-elastic reflection.

Following these assumptions, the basic properties of a SK, Eqs. (2.12)-(2.14) and (2.16), thus can be simplified as:

$$\mathscr{R}(\boldsymbol{\xi}' \to \boldsymbol{\xi}) \geq 0, \tag{2.17a}$$

$$\int_{\xi_n>0} \mathscr{R}(\boldsymbol{\xi}' \to \boldsymbol{\xi}) \mathrm{d}\boldsymbol{\xi} = 1, \tag{2.17b}$$

$$|\xi_n'| f_w(\boldsymbol{\xi}') \mathscr{R}(\boldsymbol{\xi}' \to \boldsymbol{\xi}) = |\xi_n| f_w(\boldsymbol{\xi}) \mathscr{R}(-\boldsymbol{\xi} \to -\boldsymbol{\xi}'), \tag{2.17c}$$

$$\int_{\xi_n'<0} |\xi_n'| \mathscr{R}(\boldsymbol{\xi}' \to \boldsymbol{\xi}) f_w(\boldsymbol{\xi}') \mathrm{d}\boldsymbol{\xi}' = |\xi_n| f_w(\boldsymbol{\xi}). \tag{2.17d}$$

Elementary Scattering Models

It is important to emphasise that the three properties, positiveness, normalisation, and in particular, reciprocity, impose stringent constraints on the possible choices of SKs. Here, shown in schematic Figs. 2.2(a-d), are four straightforward and intuitive models that meet these constraints.

(i) Diffuse scattering (or cosine law):

$$\mathscr{R}_{\mathrm{d}}(\boldsymbol{\xi}' \to \boldsymbol{\xi}) = \mathscr{R}_{\mathrm{d}}(\xi_{t_1}' \to \xi_{t_1}) \mathscr{R}_{\mathrm{d}}(\xi_{t_2}' \to \xi_{t_2}) \mathscr{R}_{\mathrm{d}}(\xi_n' \to \xi_n) \tag{2.18a}$$

$$= f_w(\boldsymbol{\xi}) |\boldsymbol{\xi} \cdot \boldsymbol{n}| = \frac{\xi_n}{2\pi (RT_w)^2} \exp\left\{ -\frac{\boldsymbol{\xi}^2}{2RT_w} \right\}, \tag{2.18b}$$

which indicates that gas molecules are fully accommodated to the wall (at a temperature T_w); hence, gases can be scattered into any direction with a uniform probability distribution, independent of their velocity before the collision with a surface. Such a scattering pattern is well justified for low-speed flows over engineering surfaces that exhibit roughness and are covered with adsorbed gases (Arkilic, Breuer & Schmidt, 2001; Chew, 2009; Graur, Perrier, Ghozlani & Méolans, 2009; Sharipov, 2003; Wenski, Olson, Rettner & Garcia, 1998), making it relevant in many practical applications.

(ii) Specular reflection:

$$\mathscr{R}_{\mathrm{s}}(\boldsymbol{\xi}' \to \boldsymbol{\xi}) = \delta(\boldsymbol{\xi}_t' - \boldsymbol{\xi}_t) \delta(\xi_n' + \xi_n) = \delta(\boldsymbol{\xi}' - \boldsymbol{\xi} + 2\boldsymbol{n}\xi_n), \tag{2.19}$$

where δ denotes the Dirac delta function. Physically, a specular reflection means that the tangential velocity component $\boldsymbol{\xi}_t = \{\xi_{t_1}, \xi_{t_2}\}$ does not change, while the normal component ξ_n merely reverses its direction.

(iii) Perfect backscattering (or "bounce-back" scattering):

$$\mathscr{R}_{\mathrm{b}}(\boldsymbol{\xi}' \to \boldsymbol{\xi}) = \delta(\boldsymbol{\xi}' + \boldsymbol{\xi}), \tag{2.20}$$

which indicates that the molecules reverse their speed upon collision with a wall. Notably, a complete backscattering does not exist in practice (Cercignani, 1989), while a partial backscattering evidenced by the so-called rainbow effects (refer to Section 2.3.1 for details), may occur on rough surfaces (Sharipov, 2015).

(iv) Diffuse-elastic reflection with Lambert's cosine law (Klinc & Kuščer, 1972; Kuščer et al., 1971):

$$\mathscr{R}_{\mathrm{e}}(\boldsymbol{\xi}' \to \boldsymbol{\xi}) = \frac{1}{\pi} \frac{|\xi_n|}{{\xi'}^3} \delta(\xi' - \xi), \tag{2.21}$$

which implies molecules will be scattered into arbitrary directions when colliding with a rough and rigid wall, while their absolute velocities are preserved.

2.2.2 Accommodation Coefficients (ACs)

The formulation of more detailed and practical SKs requires the incorporation of adjustable parameters, which are deduced based on general properties, such as particle conservation and time-reversal invariance (Kuščer, 1974). An inadequate understanding of these parameters can result in ambiguity, poorly defined concepts, and misinterpretation of experimental data. These key parameters, known as ACs, characterise how physical properties of the impinging molecular flux, such as momentum and energy, accommodate to the state of the wall.

The general ACs are defined as (Cercignani, 1988; Knudsen, 1911, 1934; Kuščer, 1974):

$$\alpha(\varphi) = \frac{\int_{\xi_n'<0} \varphi(\boldsymbol{\xi}')|\xi_n'| f(\boldsymbol{\xi}')\mathrm{d}\boldsymbol{\xi}' - \int_{\xi_n>0} \varphi(\boldsymbol{\xi})|\xi_n| f(\boldsymbol{\xi})\mathrm{d}\boldsymbol{\xi}}{\int_{\xi_n'<0} \varphi(\boldsymbol{\xi}')|\xi_n'| f(\boldsymbol{\xi}')\mathrm{d}\boldsymbol{\xi}' - \int_{\xi_n>0} \varphi(\boldsymbol{\xi})|\xi_n| f_w(\boldsymbol{\xi})\mathrm{d}\boldsymbol{\xi}}. \tag{2.22}$$

Physically, the numerator of Eq. (2.22) is the difference between the impinging and emerging fluxes of the quantity $\varphi(\boldsymbol{\xi})$. The denominator signifies the same difference but with the reflected distribution function f replaced by the wall Maxwellian f_w, implying that molecules are fully accommodated to the wall. By setting $\varphi(\boldsymbol{\xi})$ as momentum and energy, one obtains ACs of common interest, such as $\alpha_t(\xi_{t_1})$ and $\alpha_t(\xi_{t_2})$ for the two components of tangential momentum (TMAC), $\alpha_{E_n}(\xi_n^2)$ for normal kinetic energy (NEAC) and $\alpha_E(\xi^2)$ for total kinetic energy (EAC). However, due to the different pointing directions of impinging and emerging fluxes, it is convenient to restrict the quantity to contain the property $\varphi(\boldsymbol{\xi}) = \varphi(\boldsymbol{\xi} - 2\boldsymbol{n}[\boldsymbol{n}\cdot\boldsymbol{\xi}])$, thereby accommodation for normal momentum (NMAC) has to take the form $\varphi(\boldsymbol{\xi}) = |\boldsymbol{\xi}\cdot\boldsymbol{n}|$.

It is noteworthy that the general definition of $\alpha(\varphi)$ possesses inherent limitations when employed for a parametric characterisation of the SK; $\alpha(\varphi)$ proves to be dependent on the distribution function of impinging molecules (Cercignani, 1988; Kuščer, 1974). Additionally, when the system approaches an equilibrium state, i.e. $f(\boldsymbol{\xi}') \approx f(\boldsymbol{\xi}) \approx f_w(\boldsymbol{\xi})$, both the numerator and denominator in Eq. (2.22) veer towards zero and computational inaccuracies arise. A specialised procedure, which circumvents these limitations, is to obtain specific coefficients by selecting standard incident distributions (Kuščer, 1974). Specialists in experiments often examine monoenergetic molecular beams, expressed as $f(\boldsymbol{\xi}') = n_b \delta(\boldsymbol{\xi}' - \boldsymbol{\xi}_b)$, where n_b denotes the beam density and $\boldsymbol{\xi}_b$ a specified velocity. The resulting beam ACs, $\alpha^b(\varphi)$, though dependent on the incident velocity, can subsequently be averaged over the incident flux distribution, providing insights into more general ACs.

A more effective procedure to address these limitations is to reformulate the expression of the general AC, from $\alpha(\varphi)$ to $\alpha(\varphi, \psi)$. This alteration highlights the additional dependence on the function ψ, which describes the deviation of $f(\boldsymbol{\xi})$ and $f(\boldsymbol{\xi}')$ from equilibrium with the surface, hence characterises the incident distribution function. Following this approach, Cercignani (1988) proved that the dependency on ψ can be completely circumvented, and the general AC is re-constructed as:

$$\alpha_j \equiv \alpha(\varphi_j, \psi) = 1 - \frac{(\hat{A}\varphi_j, \psi)}{(\hat{P}_t \varphi_j, \psi)} = 1 - \lambda_j, \tag{2.23}$$

where φ is replaced by a solution φ_j of the equation $\hat{A}\varphi = \lambda \hat{P}_t \varphi$, corresponding to the eigenvalue $\lambda = \lambda_j (j = 0, 1, 2, ...)$. Here in Eq. (2.23), $\hat{P}_t$ is a tangential parity operator in velocity space, $\hat{A}$ is a *linear* gas-scattering operator that is self-adjoint in the appropriate L_2 space, and the parentheses denote a scalar product in the Hilbert space for the pair functions. Collectively, they are defined as (Cercignani, 1988; Dadzie & Méolans, 2004; Kuščer, 1978; Kuščer & Vidav, 1975; Kuščer, 1974; Méolans & Dadzie, 2005):

$$\hat{P}_t \varphi = \varphi(-\boldsymbol{\xi} + 2\boldsymbol{n}[\boldsymbol{n} \cdot \boldsymbol{\xi}]), \tag{2.24}$$

$$\hat{A}\psi(\boldsymbol{\xi}) = [|\xi_n| f_w(\boldsymbol{\xi})]^{-1} \int_{\xi_n > 0} |\xi_n'| f_w(\boldsymbol{\xi}') \mathscr{R}(-\boldsymbol{\xi}' \to \boldsymbol{\xi}) \psi(\boldsymbol{\xi}') \mathrm{d}\boldsymbol{\xi}', \tag{2.25}$$

$$(\varphi, \psi) = (\psi, \varphi) = \int_{\xi_n > 0} \varphi(\boldsymbol{\xi}) \psi(\boldsymbol{\xi}) f_w(\boldsymbol{\xi}) |\xi_n| \mathrm{d}\boldsymbol{\xi}. \tag{2.26}$$

A disadvantage of Eq. (2.23) is that the ACs correspond to the eigenfunctions φ_j, which typically lack a straightforward physical interpretation. Alternatively, a more physically meaningful reconstruction has been explored by Kuščer (1974); S. Shen and Kuščer (1971); Waldmann (1977), but only for the distribution function $f = f_w[1 + \varphi_j(-\boldsymbol{\xi})]$, wherein $\varphi_j = \psi$, assuming the source of perturbation is consistent with the quantity under consideration. Consequently, a

matrix of ACs is obtained, with symmetric elements defined as:

$$\alpha_{ij} = 1 - \frac{(\varphi_i, \hat{A}\varphi_j)}{(\varphi_i, \hat{P}_t\varphi_j)} = 1 - \frac{(\varphi_j, \hat{A}\varphi_i)}{(\varphi_j, \hat{P}_t\varphi_i)} = \alpha_{ji}, \tag{2.27}$$

where the first subscript refers to the quantity i being transported to and from the surface, while the second j indicates the type of perturbation. As accommodation of momentum and energy are of interest and the perturbation is typically caused by a slow flow in the directions t_1, t_2, n, or by a small temperature difference, Kuščer (1974) proposed to further restrict $\varphi_i \in \{\xi_{t_1}, \xi_{t_2}, \xi_n, \xi^2\}$. This restriction thereby naturally aligns with the idea of Knudsen (1911, 1934) that ACs should exclusively depend on the properties of the gas molecules and the surface, and leads to the so-called Knudsen ACs. Notably, Eq. (2.27), perceivable as a linear least-squares fitting of the scattering quantities, is of practical importance in the numerical computation of ACs, which is further detailed in Section 3.3.

2.2.3 The General Form of Scattering Kernels (SKs)

The General Form Proposed by Cercignani

The complexity of GSIs can be substantially mitigated by stating the values of ACs. Nevertheless, the utilisation of ACs should be, in principle, firmly related to SKs. A tangible relation between ACs and SKs is apparent, fundamentally dependent on the choice of functions for φ and ψ. Cercignani (1988) therefore advocates developing more general SKs via the eigenvalue equation of ACs given by Eq. (2.27), during which the construction satisfies basic properties Eqs. (2.17a)-(2.17c) while without being bound by other constraints.

By taking a series expansion of the kernel under appropriate assumptions on its eigenfunctions and eigenvalues, Cercignani (1988) proved that the simplest mathematical expression satisfying basic properties takes the general form:

$$\mathscr{R}_{\mathrm{G}}(\boldsymbol{\xi}' \to \boldsymbol{\xi}) = \mathscr{R}_{\mathrm{G},t}(\boldsymbol{\xi}_t' \to \boldsymbol{\xi}_t)\,\mathscr{R}_{\mathrm{G},n}(\xi_n' \to \xi_n), \tag{2.28a}$$

where

$$\mathscr{R}_{\mathrm{G},t}(\boldsymbol{\xi}_t' \to \boldsymbol{\xi}_t) = \frac{\left(1-q^2\right)^{-1}}{2\pi RT_w} \exp\left\{-\frac{1}{1-q^2}\frac{(\boldsymbol{\xi}_t - q\boldsymbol{\xi}_t')^2}{2RT_w}\right\}, \tag{2.28b}$$

$$\mathscr{R}_{\mathrm{G},n}(\xi_n' \to \xi_n) = \frac{(1-p)^{-1}\,\xi_n}{RT_w} \exp\left\{-\frac{\xi_n^2 + p\xi_n'^2}{2RT_w(1-p)}\right\} I_0\left(\frac{\sqrt{p}}{1-p}\frac{\xi_n\xi_n'}{RT_w}\right). \tag{2.28c}$$

$\boldsymbol{\xi}_t$ is the two-dimensional vector residing on the tangential plane with velocity components ξ_{t_1} and ξ_{t_2}, which possess equivalent scattering dynamics on an isotropic surface, the bounded parameters $q \in [-1, 1]$ and $p \in [0, 1]$ stems from the kernel expansion and can be related to the aforementioned ACs that possess a more transparent physical interpretation. I_0 is the modified

Bessel function of the first kind and zeroth order, defined as:

$$I_0(y) = \frac{1}{2\pi}\int_0^{2\pi} \exp(y\cos\phi)\mathrm{d}\phi. \tag{2.28d}$$

The General Form Proposed by Kuščer et al.

It is worth stressing that a simplified version of the general form has also been independently proposed by Kuščer (1978); Kuščer et al. (1971), who implicitly follow the assumption by Knudsen (1911); that is, if the incident distribution is a Maxwellian of arbitrary temperature $T' \neq T_w$, then the reflected distribution should again be Maxwellian with an intermediate temperature T. The ratio of the temperature difference is related to the accommodation of energy, and expressed via the parameter μ:

$$\frac{T - T_w}{T' - T_w} = \mu^2. \tag{2.29}$$

The additional assumption can be made that if the incident distribution is a Maxwellian of temperature T_w, and drifting parallel to the surface with a small speed u_t, then the reflected distribution should be of the same kind, slowed down by a factor μ, i.e., $u_t/u_t' = \mu$. Knudsen's assumption and this supplement, as well as normalisation and reciprocity, are satisfied by a one-parameter family of SKs (of adjustable parameter being μ). This can be shown by considering the three factors of each Maxwellian flux as generating functions of Laguerre and Hermite polynomials. Orthogonality of the polynomials then helps to establish $\mathscr{R}(\boldsymbol{\xi}' \to \boldsymbol{\xi})$ as a bilinear series following the form:

$$\begin{aligned}\mathscr{R}(\boldsymbol{\xi}' \to \boldsymbol{\xi}) = {} & \frac{\xi_n}{2\pi(RT_w)^2(1-\mu^2)^2} I_0\left(\frac{\mu}{1-\mu^2}\frac{\xi_n\xi_n'}{RT_w}\right) \\ & \times \exp\left\{-\frac{1}{1-\mu^2}\frac{\xi_n^2 + \mu^2\xi_n'^2}{2RT_w} - \frac{1}{1-\mu^2}\frac{|\boldsymbol{\xi}_t - \mu\boldsymbol{\xi}_t'|^2}{2RT_w}\right\}.\end{aligned} \tag{2.30}$$

Here, Knudsen's assumption can be generalised by allowing a distorted reflected Maxwellian with different temperatures for motion parallel to the surface and normal to it. Eq. (2.30) can therefore readily be extended to Cercignani's general form Eq. (2.28), with $\mu = q$ for the tangential components and $\mu = \sqrt{p}$ for the normal component.

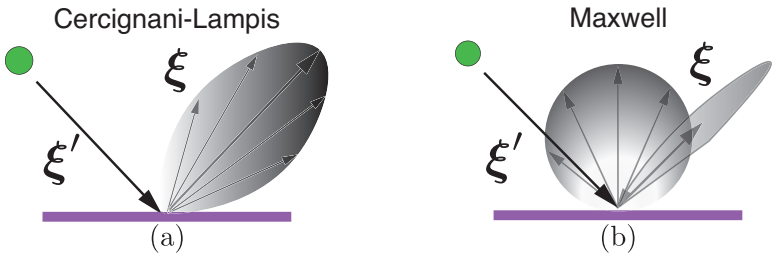

Figure 2.3: Schematics illustrating two classical gas molecule scattering patterns: (a) Maxwell model; (b) Cercignani–Lampis (CL) model.

All existing SKs can be readily derived from the general form of Eq. (2.28), or equivalently, by Eq. (2.30). Furthermore, any linear combination of this form, with weighting coefficients summing to unity, still constitutes a kernel that satisfies all the basic properties. For elementary diffuse and specular reflections, as well as the prevalent Cercignani–Lampis (CL) model, the substitution of ACs into the general form, Eq. (2.28), is as follows:

$$\text{Diffuse:} \quad q = p = 0; \tag{2.31a}$$

$$\text{Specular:} \quad q = p = 1; \tag{2.31b}$$

$$\text{CL:} \quad q = 1 - \alpha_t, \quad p = 1 - \alpha_{E_n}. \tag{2.31c}$$

Cercignani–Lampis (CL) Model

The CL model stands as a comprehensive SK and incorporates two ACs, α_t and α_{E_n}. It was originally obtained by a series expansion of the kernel under suitable assumptions on its eigenfunctions and eigenvalues (Cercignani & Lampis, 1971). Another derivation by Cercignani (1972) involves solving the half-space transport equation that details the gas dynamics within the wall modelled as a homogeneous and non-polar medium. Notably, the CL model has also been revisited using diverse approaches, each grounded in distinct physical meanings. These include drawing analogies with Brownian motion (Kuščer et al., 1971) and with the scattering of electromagnetic waves by random rough surfaces (Williams, 1971), assuming separability condition and special symmetric function (Cowling, 1974), and adopting a stochastic Langevin dynamical framework (Takata, Akasobe & Hattori, 2021). The resulting CL model is able to reproduce the lobular pattern observed by molecular beam experiments, depicted in Fig. 2.3(a). Furthermore, the CL model simplifies to diffuse scattering when $\alpha_t = 1$ and $\alpha_{E_n} = 1$. In the case of $\alpha_t = 0$ and $\alpha_{E_n} = 0$, it corresponds to specular reflection. The condition $\alpha_t = 2$ and $\alpha_{E_n} = 0$ results in perfect backscattering.

Maxwell Model and Other Linear Combinations

Among all existing SKs represented as linear combinations of the general form, the most notable was proposed by Maxwell (1879). The Maxwell model, as shown in schematic Fig. 2.3(b), assumes that a fraction α, often represented by TMAC or EAC, of the incident gas molecules undergo diffuse reflection, while the remainder $(1-\alpha)$ are re-emitted specularly. Consequently, the diffuse-specular Maxwell SK reads:

$$\mathscr{R}_{\mathrm{M}}(\boldsymbol{\xi}' \to \boldsymbol{\xi}) = \alpha \mathscr{R}_{\mathrm{d}}(\boldsymbol{\xi}' \to \boldsymbol{\xi}) + (1-\alpha)\mathscr{R}_{\mathrm{s}}(\boldsymbol{\xi}' \to \boldsymbol{\xi}). \tag{2.32}$$

Though extensively employed to describe incomplete accommodation, the Maxwell model fails to reproduce the lobular scattering pattern observed in molecular beam experiments (Cercignani & Lampis, 1971). Furthermore, there are cases where theoretical predictions based on such a kernel contradict experimental results (Sharipov, 2015). This contradiction arises largely because the Maxwell model incorporates only a single free parameter, α, thereby oversimplifying the underlying scattering mechanisms. For instance, momentum and energy are known to accommodate at different rates in physical interactions, with momentum changing more rapidly than energy (Cercignani, 1988). This highlights a fundamental limitation of the Maxwell model.

Epstein (1967) extended the Maxwell model by substituting the constant coefficient α with a function of the molecular velocity, highlighting the dependency of the scattering dynamics on the incident velocity of the particle. Struchtrup (2013) combined the Epstein model with the diffuse-elastic kernel. The resulting model provides results similar to the CL model but possesses a more straightforward mathematical expression facilitating the derivation of boundary conditions for extended moment equations. Yamamoto, Takeuchi and Hyakutake (2007) suggested that a fraction of scattered molecules follow a CL-like model, while the remaining molecules undergo diffuse reflection. The proposed model aligns closely with numerical simulations when the surface encounters contamination with a set volume of heavy molecules and is under bombardment from lighter gases. However, it does not contain links with the contaminant information nor the adsorption physics, acting more as a phenomenological model with coefficients fitted from specific simulations conditions and is thus not general. An adsorption model was introduced by Brancher, Stefanov, Graur and Frezzotti (2020), which linearly combines the fully diffuse and CL (or Maxwell with incomplete accommodation) models. This model captures the temporal variation of the adsorbed surface coverage, which simplifies to the Langmuir isotherm (Butt, Graf & Kappl, 2003; Langmuir, 1916) when adsorption and desorption rates balance. The combination of Epstein and CL models has also been proposed, which not only is evidenced to more accurately capture the molecular trajectory during the scattering process (Yakunchikov, Kovalev & Utyuzhnikov, 2012), but also provides an accurate description of both the Poiseuille and thermal transpiration flows (Wu & Struchtrup, 2017).

2.2.4 Transport Equations Within the Surface Layer

Under the Constraint of Reciprocity

The mathematical approach, specifically the expansion series of the kernel based on its eigenfunctions and eigenvalues, can be useful for obtaining relatively simple expressions for a range of SKs involving adjustable parameters. However, these kernels and their associated parameters lack a direct correlation with the fundamental physical properties of GSIs. This includes aspects such as atom and crystal characteristics, wall atom temperatures, and the intricacies of the interaction potential (Cercignani, 1972, 1988). Additionally, the physical origins of the bounded parameters in Eq. (2.28) remain largely unspecified.

Building on this, Cercignani (1972, 1988) pointed out a possible way of finding kernels from physically more meaningful models. He began with the Liouville equation, which describes a gas molecule captured by a wall in thermal equilibrium; notably, the state of the wall is presumed unaffected by this gas molecule in order to satisfy reciprocity (see Section 2.2.1). Following this path, the solid atoms are treated as part of a mechanical system, with a well-defined geometrical boundary occupying the half-space. The surface of this boundary is flat, and the solid atoms within the wall are modelled as a homogeneous, non-polar medium illustrated in schematic Fig. 2.4(a). Physically, this implies that the microscopic properties of the system will not depend on the tangential directions. Given the complexity of the Liouville equation—primarily due to the large number of variables involved—it is reduced from describing a multi-particle system to a transport equation that only involves the one-particle distribution function. This simplification is especially relevant in scenarios with harmonic forces among wall atoms, which may be less chaotic or more predictable, corresponding to multi-phonon excitation cases (Kuščer, 1978; Manson & Miret-Artés, 2022) (see also in Section 2.3.1).

Regarding the intermolecular potential in GSIs, Cercignani (1972, 1988) advocated for the separate consideration of long-range, intermediate-range, and short-range interactions. These interactions, as illustrated in Fig. 2.4(b), can be readily related to the Vlasov term, the FP collision term and the Boltzmann collision term (as reviewed in Section 2.1.2), respectively. The half-space transport equation for the probability density $P(r_n, \boldsymbol{\xi})$ of a molecule at position r_n with velocity $\boldsymbol{\xi}$ is therefore presented as follows:

$$\frac{\partial P}{\partial t} + \boldsymbol{\xi} \cdot \frac{\partial P}{\partial r_n} + \underbrace{\frac{\partial P}{\partial \boldsymbol{\xi}} \cdot X(r_n)}_{\text{Long-range interactions, e.g. Vlasov}} = LP, \tag{2.33a}$$

where

$$LP = \underbrace{\int (P_{w*}\, P - P'_{w*}\, P')\mathscr{W}\, \mathrm{d}\boldsymbol{\xi}'_* \mathrm{d}\boldsymbol{\xi} \mathrm{d}\boldsymbol{\xi}_*}_{\text{Short-range interactions, e.g. Boltzmann}} + \underbrace{\sum_{i,j=1}^{3} \left[\frac{\partial}{\partial \xi_i} \left(D_{ij} \frac{\partial P}{\partial \xi_j} \right) + \frac{\partial}{\partial \xi_i} \left(F_{ij} \xi_j P \right) \right]}_{\text{Intermediate-range interactions, e.g. Fokker-Planck}}, \tag{2.33b}$$

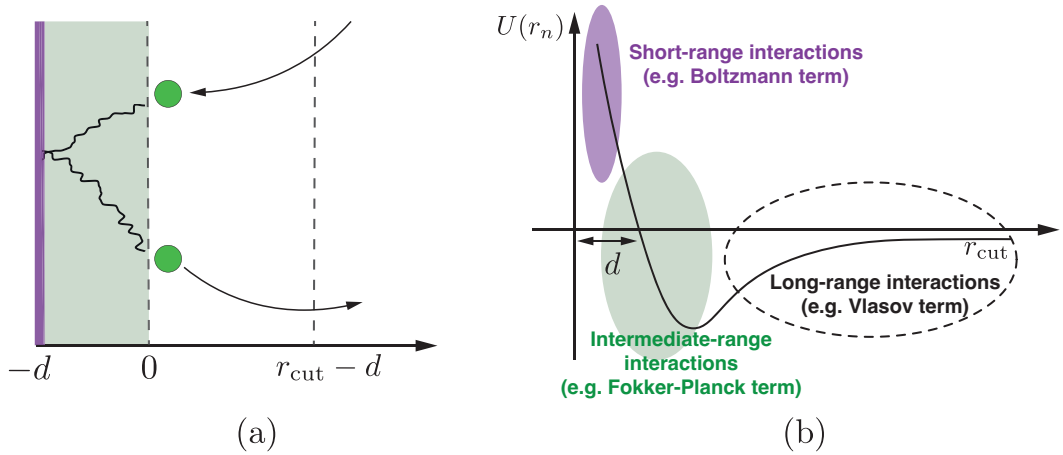

Figure 2.4: (a) A schematic illustrating the motion of a gas molecule within the near-surface layer, which is governed by the range of surface forces and noted by the cut-off distance of intermolecular potentials r_{cut}. (b) A typical surface interaction potential, U, plotted against r_n, can be divided into long-range, intermediate-range, and short-range interactions.

in which

- $X(r_n)$ denotes the average of long-range forces exerted by solid atoms upon a gas molecule (see Section 2.1.2). It depends simply on r_n due to the symmetry of the wall.
- $P_{w*} = P_w(\boldsymbol{\xi}_*), P'_{w*} = P_w(\boldsymbol{\xi}'_*)$, where P_w denotes the equilibrium Maxwellian of the solid atoms; $\mathscr{W}$ holds the same interpretation as in Eq. (2.5), the Boltzmann hard collision term, except for the fact that it is based on the details of a collision between a gas molecule and a solid wall atom. Notably, the collision terms in Eq. (2.33) pertain solely to gas–solid collisions, with gas–gas collisions being disregarded.

Given the complexity of addressing all interactions, it is understandably challenging to find a simple solution of Eq. (2.33). Cercignani (1972, 1988) opted for a path that is very promising, but is less fundamental. Specifically, Cercignani targeted analytically computable kernels. This class of more tractable models can be obtained by considering the steady state of the transport equation, suppressing the long-range force fields that are represented by a specularly reflecting barrier at $r_n = -d$ shown in schematic Fig. 2.4(a), and keeping either the short or the intermediate-range interactions.

Considering the intermediate-range interactions as an example, upon solving the aforementioned time-independent FP system, one obtains the probability density $P(r_n = 0, \boldsymbol{\xi})$ of reflected molecules against incident molecular beam $\delta(\boldsymbol{\xi} - \boldsymbol{\xi}')$. This distribution is then incorporated into the expression:

$$\mathscr{R}(\boldsymbol{\xi} \to \boldsymbol{\xi}') = \frac{|\boldsymbol{\xi} \cdot \boldsymbol{n}|}{|\boldsymbol{\xi}' \cdot \boldsymbol{n}|} P(r_n = 0, \boldsymbol{\xi} \cdot \boldsymbol{n} > 0), \tag{2.34}$$

which is obtained by substituting $f = \delta(\boldsymbol{\xi} - \boldsymbol{\xi}')$ into Eq. (2.11). Accordingly, finding the form of SK is identical to finding P at $r_n = 0$, when $\xi_n > 0$. Finally, the CL model is elegantly retrieved by establishing a correlation between the ACs (α_t, α_{E_n}) and physical parameters that are related to the diffusion D_{ij} and friction F_{ij} tensors in velocity space (Cercignani, 1972, 1988).

It is worth stressing that Kuščer et al. (1971) independently proposed a similar concept of utilising a modified FP term for GSIs (Cercignani, 2003), inspired by the diffusion of a Brownian particle in velocity space. Solutions to the modified FP system yield a one-parameter family of SKs that meet all basic constraint properties. Again, a natural generalisation of this SK aligns exactly with the CL model (as reviewed in Section 2.2.3). Cercignani's approach has also been revisited by Takata et al. (2021), leading to the retrieval of the CL model via the Langevin system. This facilitates the inclusion of time-delay effects in the scattering model. Moreover, this Langevin system provides a clearer physical interpretation of the CL model, distinguishing it into two components: diffusion and drift. These two components exhibit competitive effects during GSIs, shaping the ultimate scattering patterns.

Cercignani (1972) also addressed short-range interactions by simplifying the Boltzmann collision term in Eq. (2.33b) to its linear form. The resulting linear Boltzmann equation, Eq. (2.9), thus describes the behaviour of gas molecules trapped in solid atoms, considered as a background medium. Depending on the position of the reflecting barrier, either at $r_n = -d$ or $r_n = 0$, it leads to the choice of either the Maxwell or the fully diffuse scattering model.

Without the Constraint of Reciprocity

Before delving into more detailed transport equations for kinetic boundary conditions, let us briefly revisit the physical implications of reciprocity: microscopic scattering dynamics is time-reversible, and the surface is assumed to be in a state of local equilibrium, undisturbed by impinging gas molecules (Cercignani, 1988; Kuščer, 1971). These assumptions, which appear to have general validity, underpin the derivation of the general form of SKs (Cercignani, 1988; Kuščer et al., 1971) and aforementioned transport equations for physical models (Cercignani, 1972, 1988; Kuščer et al., 1971; Takata et al., 2021). Notably, this led Kuščer (1971) to assert that all gas–surface kernels obey the reciprocity relation (Bärwinkel & Schippers, 1989).

While reciprocity seemingly holds in many typical experimental situations (Bärwinkel & Schippers, 1989), the proof of $\mathscr{H}$-theorem for GSIs (Cercignani, 1972; Darrozes & Guiraud, 1966; J. L. Lebowitz & Frisch, 1957) explicitly demonstrates the local nature of irreversibility in GSIs and its general applicability to any point on the wall. This apparent disagreement between reciprocity (time-reversibility) and $\mathscr{H}$-theorem (irreversibility) is trivial when considering deviations from local equilibrium due to slight perturbations, such as slow drifts or small temperature differences, c.f. linear transport theory (Cercignani, 1988; Sharipov, 2015). Under such conditions, as also will be constructed in the MD systems shown in Section 3.2, it

is sufficient to consider the bulk of the solid as a thermal reservoir, while allowing for a thin near-surface layer for non-equilibrium dynamics. Conventional SKs thus remain appropriate for these scenarios, preserving the quasi-Maxwellian nature for both incident and reflected fluxes, even if strict reciprocity becomes invalid.

Given the fundamental importance of $\mathscr{H}$-theorem in GSIs, the constraints of reciprocity can be relaxed, especially when considering non-isolated systems (Bärwinkel & Schippers, 1989; Goldberger & Watson, 2004). A prime example of nonreciprocity is observed in flows characterised by orbital high speeds, wherein gas molecules impinging on shuttle surfaces significantly disturb solid wall atoms, inducing pronounced heating (Hurlbut & Sherman, 1968). Moreover, the examination of lift-to-drag ratio measurements for the Shuttle Orbiter in the free-molecular regime suggests a significant deviation from diffuse, fully equilibrated re-emission of molecules from the surface (R. C. Blanchard, 1986; Cercignani, 2000), thus contradicting the use of conventional SKs in accordance with a non-drifting Maxwellian as a limiting case. Instead, the model proposed by Nocilla (1961, 1963) and subsequently examined by Hurlbut and Sherman (1968), assumes that molecules are reflected according to a drifting Maxwellian with a temperature that is, in general, different from the temperature of the wall. Although this model does not align with reciprocity (Kuščer et al., 1971), it has proven valuable for representing experimental data and has been utilised in actual computational works (Cercignani, 2000).

We shall now shift our focus back to transport equations that describe a wall system interacting with its surroundings (Bergmann & Lebowitz, 1955; J. L. Lebowitz & Bergmann, 1957). We start from a model based on the simultaneous solution of the Boltzmann equation for the gas and the kinetic equation for all particles within the range of surface forces, as posited by Borman, Krylov and Prosyanov (1988). This model bears similarities to the clues presented by Cercignani (1972, 1988), transitioning from the Liouville equation to the equation for the one-particle distribution function of molecules in the quasi-classical limit. Furthermore, this model considers not only the interactions with a solid occupying the half-space but also the ensemble of molecules constituting the adjacent gas phase. The governing kinetic equation (for monatomic gas) thus follows:

$$\frac{\partial f}{\partial t} + \boldsymbol{\xi} \cdot \frac{\partial f}{\partial \boldsymbol{r}} - \frac{1}{m}\frac{\partial U}{\partial \boldsymbol{r}} \cdot \frac{\partial f}{\partial \boldsymbol{\xi}} = Q_{\text{gas-gas}}(f,f) + Q_{\text{gas-ph}}(f), \tag{2.35}$$

where $f(\boldsymbol{\xi}, \boldsymbol{r}, t)$ represents the distribution function for physisorbed or gas molecules, and U is the intermolecular potential between fixed wall atoms and gas molecules. $Q_{\text{gas-gas}}$ is the gas–gas collision operator, which accounts for the effects of interparticle interactions, while $Q_{\text{gas-ph}}$ represents the gas–phonon collision operator, serving as a dissipative term to account for interactions with the heat bath.

Although considering solid walls as 'distributed collisions' — by incorporating appropriate functions or collision terms into Eq. (2.35) — is more complex than simply adopting an analytical SK, this approach offers significant advantages. In particular, it provides a flexible and comprehensive description of non-equilibrium systems undergoing irreversible processes, constrained only by $\mathscr{H}$-theorem. A series of studies (Aoki, Charrier & Degond, 2011; Aoki & Giovangigli, 2019, 2021; Aoki et al., 2024, 2022; Beenakker, Borman & Krylov, 1994, 1995; Beenakker & Krylov, 1997; Borman et al., 1988; Borman, Krylov & Prosyanov, 1990; Brull, Charrier & Mieussens, 2013, 2014, 2016; Frezzotti & Gibelli, 2008; Krylov, 2003; Krylov, Prosyanov & Beenakker, 1997) have employed this approach to explore GSIs, nanoflows, and surface diffusion. Despite its somewhat crude approximation of the complex GSIs, it has proved to be remarkably useful by offering fresh perspectives on these issues. More specifically, this approach is capable of explaining the density dependence of the diffusion coefficient (Beenakker & Krylov, 1997; Krylov et al., 1997), and can be easily modified or expanded to encompass GSIs in dense fluid flows (Frezzotti & Gibelli, 2008), nanoscale surface roughness (Brull et al., 2016), as well as adsorption and chemical reactions on crystal surfaces (Aoki & Giovangigli, 2019, 2021).

By employing standard tools in kinetic theory, such as scaling and systematic asymptotic analysis, one can derive solutions for transport equations. Nevertheless, formulating a precise transport equation itself, as in Eq. (2.35), presents two main challenges. The first challenge lies in the selection and accuracy of the intermolecular potential U (Aoki et al., 2022; Cercignani, 1988). Determining this potential proves difficult as it varies markedly depending on the unique characteristics of each gas–surface combination. Furthermore, unlike the intuitive categorisation of potentials into long, intermediate, and short interactions by Cercignani (1972, 1988), where each type is addressed separately, the continuous potentials in Eq. (2.35) appear difficult to resolve in a unified manner. The second challenge involves the intricate nature of the gas–phonon collision operator $Q_{\text{gas-ph}}$. This necessitates a thorough understanding of solid-state physics (Kuščer, 1978; Manson & Miret-Artés, 2022), which is an expansive subject in its own right. A prevalent strategy to navigate this complexity is to assume that phonons maintain equilibrium, following the Bose–Einstein distribution (Aoki et al., 2022; Brull et al., 2013; Péraud & Hadjiconstantinou, 2011). Such an assumption paves the way for an effective BGK-like term to represent $Q_{\text{gas-ph}}$. Another straightforward strategy, as already posited by Kuščer (1971) and Cercignani (1972), is to employ a diffusive FP term for $Q_{\text{gas-ph}}$, applicable mainly at standard wall temperature or higher. This is grounded in the fact that, at these temperatures, quantum effects are negligible due to the minor energy level differences involved in phonon creation or annihilation (Bird, 1994; Manson & Miret-Artés, 2022). Consequently, a classical description of scattering is applicable, and $Q_{\text{gas-ph}}$ can be modelled as continuous small perturbations to the system, represented by the diffusive FP form (Borman et al., 1988; Krylov,

2003), as also adopted by numerous researchers (Barth, 2000). Finally, it is worth stressing that from the FP equation, the relaxation time used in the BGK-like approach may be derived, underscoring the complementary nature of these strategies in understanding and modelling $Q_{\text{gas-ph}}$ and the relaxation process towards wall equilibrium.

2.3 GSIs — Phenomenological Aspects Grounded in Solid-State Physics

In this section, GSIs are introduced from the perspective of solid-state physics, emphasising the physical attributes of the wall. Considering the broad nature of the subject, readers are directed to key textbooks (Billing, 2000; Goodman & Wachman, 1976; Muiño & Busnengo, 2013) and review papers (Barker & Auerbach, 1984; Cardillo, 1981; Kuščer, 1978; Manson & Miret-Artés, 2022; C. Rettner, Auerbach, Tully & Kleyn, 1996; Tully, 1980). Several key concepts are briefly described, including (a) the transition from quantum mechanical scattering to classical scattering, (b) the role and impact of the Debye–Waller factor (DWF) in GSIs, and (c) classical rainbow scattering and its implications.

2.3.1 Phonon Excitation — From Quantum Mechanical to Classical

The greatest detail of GSIs emerges from experiments in the quantum mechanical regime, characterised by low projectile energies, low surface temperatures, and small projectile masses (Manson & Miret-Artés, 2022). These studies yield insights into the GSI potential, as well as surface order and structure, by analysing diffraction patterns. For instance, when the system reaches a threshold at which individual quantum excitations become noticeable, it becomes possible to study surface phonons. At this point, any imperfections on the surface will also become evident and can be revealed through the patterns that emerge between the diffraction peaks observed in experiments. Conversely, in engineering practices, GSIs are generally analysed within the classical or multiphonon regime, characterised by higher incident energies, elevated surface temperatures, and the use of heavier incident gases (Billing, 2000; Goodman & Wachman, 1976). This classical regime suppresses quantum features like diffraction and single phonon events, typically yielding broader single or sometimes multiple peaks that indicate classical behaviour.

Understanding the transition to classical scattering as incident energy increases necessitates a quantum viewpoint, anchored by Fermi's Golden Rule. This principle defines the transition rate, $\Gamma(\boldsymbol{k}, \boldsymbol{k}')$, for a particle's scattering vector to change from $\boldsymbol{k}'$ to $\boldsymbol{k}$ per unit time. For elastic scattering — those not involving energy transfer with the wall atoms — the transition rate can be evaluated exactly by considering the interaction potential as a pairwise sum over all unit cells of the surface. The expression for purely elastic diffraction on a defect-free surface is (Manson

& Miret-Artés, 2022):

$$\Gamma^{(0)}(\boldsymbol{k},\boldsymbol{k}') = \frac{2\pi}{\hbar}\sum_{\mathbf{G}}\exp\{-\langle(\boldsymbol{u}_\ell\cdot\Delta\boldsymbol{k})^2\rangle\}|T^{(0)}_{\boldsymbol{k},\boldsymbol{k}'}|^2\delta_{\Delta\boldsymbol{k}_t,\mathbf{G}}\delta(E_{\boldsymbol{k}}-E_{\boldsymbol{k}'}), \tag{2.36}$$

where $\hbar$ is the reduced Planck constant. $E'_{\boldsymbol{k}}$ and $E_{\boldsymbol{k}}$ represent the total energy of the system before and after the scattering, respectively. $\Delta\boldsymbol{k}_t = \boldsymbol{k}_t - \boldsymbol{k}'_t$ indicates the change between the parallel components of the reflected and incident particle wavevectors on the surface, with $\mathbf{G}$ being the reciprocal lattice vector, representing the periodicity and symmetry of a crystal lattice in reciprocal space (Billing, 2000; Kittel, 2005; Simon, 2013). The only observable scattering intensities appear as diffraction peaks when $\boldsymbol{k}_t = \boldsymbol{k}'_t \pm \mathbf{G}$, with intensities proportional to the squared magnitude of the transition matrix $|T^{(0)}_{\boldsymbol{k},\boldsymbol{k}'}|^2$. Additionally, each peak is multiplied by a DWF, accounting for the attenuation of diffraction arising from the thermal motion of solid atoms:

$$\text{DWF} = \exp\{-\langle(\boldsymbol{u}_\ell\cdot\Delta\boldsymbol{k})^2\rangle\}, \tag{2.37}$$

where $\boldsymbol{u}_\ell$ represents the displacement of the wall atom from its equilibrium position due to its thermal vibration, $\Delta\boldsymbol{k}$ is the change in wavevector after scattering. Angle brackets denote the thermal average at a given temperature (Barker & Auerbach, 1984; Goodman & Wachman, 1976). The presence of the DWF in elastic diffraction intensities highlights the intersection of quantum mechanical and classical multiphonon scattering. It is evident that the total phonon excitation in a collision correlates with the exponent $\langle(\boldsymbol{u}_\ell\cdot\Delta\boldsymbol{k})^2\rangle$. When this value is around or below one, scattering predominantly manifests as elastic diffraction or inelastic phenomena governed by single phonon events, thereby necessitating a quantum mechanical treatment. A more detailed perspective of the DWF is obtained through its explicit expression for the specular diffraction beam (Manson & Miret-Artés, 2022):

$$\langle(\boldsymbol{u}_\ell\cdot\Delta\boldsymbol{k})^2\rangle = \frac{24m}{m_w}\frac{E'\cos^2(\theta_i)\,T_w}{k_B\Theta_D^2}, \tag{2.38}$$

where m_w represents the effective mass of the surface, E' the incident energy and θ_i the angle of incidence, and Θ_D the Debye temperature. Eq. (2.38) implies a suppression of quantum features when there is an increase in mass ratio between gas molecules and wall atoms, the incident energy and the wall temperature. Single phonon excitations, which rely on their creation or annihilation at specific frequencies, are also governed by a DWF, while the detailed expression is omitted here for brevity. Finally, in the limit of multiphonon excitations, the reflection pattern essentially becomes the envelope of all the quantum peaks. It is within this domain that classical theories aptly describe the scattering processes, as depicted in Fig. 2.5(a).

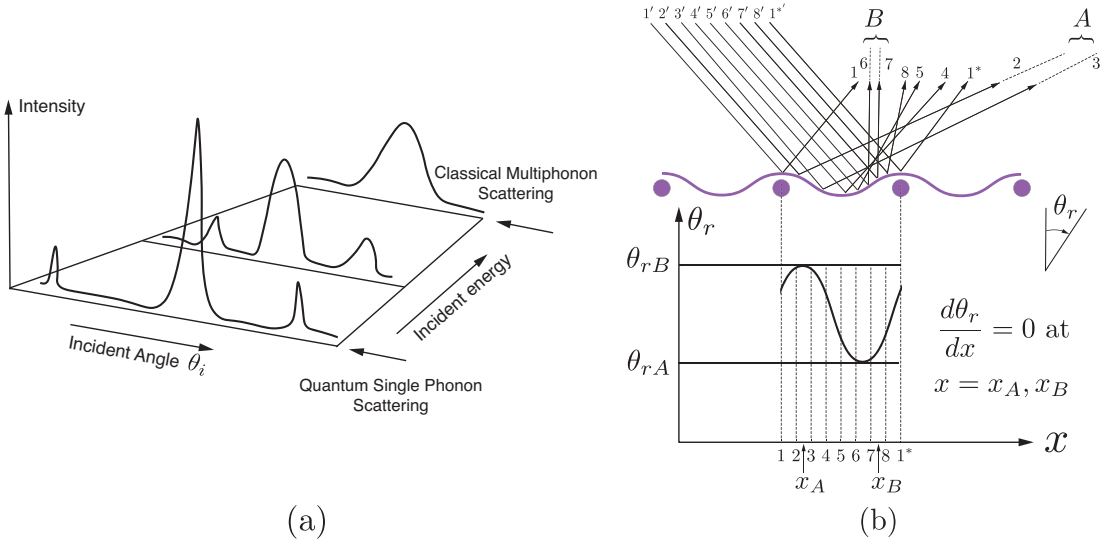

Figure 2.5: (a) Schematic depicting the transition from quantum mechanical scattering to classical scattering (Manson & Miret-Artés, 2022). At low incident energies, sharp quantum features are observed in the angular distributions (at specific frequencies), while at higher energies, quantum peaks become indistinguishable, and only broad classical features appear. (b) Schematic illustrating the formation of classical surface rainbows from a two-dimensional scattering model with one-dimensional periodicity (Goodman, 1971). Two pronounced scattering lobes can be observed at location x_A and x_B.

The phenomenon of classical rainbow scattering merits particular emphasis due to its significant physical implications (Goodman & Wachman, 1976; Miret-Artés & Pollak, 2012). In the quantum regime, gas particle beams scattered from a surface appear as sharply defined peaks, corresponding to diffracted beams influenced by the surface lattice structure and phonon excitation. Transitioning to the classical regime, a distinct change is observed: the emergence of two pronounced lobes at opposite sides of the specular scattering angle, marking the classical rainbow effect. These lobes, which encompass a range of quantum mechanical diffraction peaks, signify surface corrugations, particularly on well-ordered/periodic surfaces, as shown in the schematic Fig. 2.5(b). The intricate relationship between classical rainbow scattering and quantum mechanical diffraction can be revealed through scattering experiments, often highlighted by the occurrence of multiple maxima (Goodman & Wachman, 1976).

2.3.2 Cube Models — Attempts to Circumvent Quantum Mechanics

There have been endeavours to seek physically-grounded representations of GSIs, which, meanwhile, circumvent detailed quantum-mechanical considerations. Such approaches often distil complex interactions into binary collisions, exemplified by cube models that treat the surface as an array of effective cubes. These cube models, reviewed in detail by Goodman and Wachman (1976) and Livadiotti et al. (2020), rely on experimental data and are particularly useful for elucidating the influence of surface thermal motion on gas scattering.

Among these, three quasi-one-dimensional models are noteworthy: the hard-cubes, soft-cubes, and washboard models. The hard-cubes model (Logan & Stickney, 1966) utilises a simple impulsive-repulsive potential, neglecting any attractive forces, and assumes that momentum exchange is solely due to the normal component of the gas particle velocity. While sacrificing some accuracy, this model provides a qualitative match to the lobular scattering patterns observed in experiments. Logan and Keck (1968) later refined this model by incorporating a 'soft' potential well (the soft-cubes model), better representing energy-specific scattering events and adsorption processes, though it still failed to adequately account for tangential momentum transfer. The Washboard model by Tully (1990) introduced a sinusoidal surface and a corrugation parameter to address surface irregularities for cube models. While it offers a closed-form solution for scattering patterns, the model holds improper local collision assumptions and fails to capture the reversibility of gas molecular trajectories, hence violating the reciprocity relation (Liang, Li & Ye, 2018).

Although cube models are computationally convenient compared to solving transport equations, their fidelity to physical reality is generally constrained. The hard-cubes model is valuable mostly for qualitative understanding, while the soft-cubes and washboard models rely on additional premises, such as a Maxwellian energy distribution of the wall atoms or sinusoidal surface corrugation, which may not be universally valid. Furthermore, cube models typically stem from the detailed characterisation of single scattering events, thus requiring excluding molecules continuing inward post-interaction or adopting a simplified approach to handle multiple scattering events. Because of these arbitrariness, cube models often lead to non-normalised results and violate the reciprocity (Cercignani, 2003; Kuščer, 1978), limiting their broader applications, especially in precision-critical scenarios.

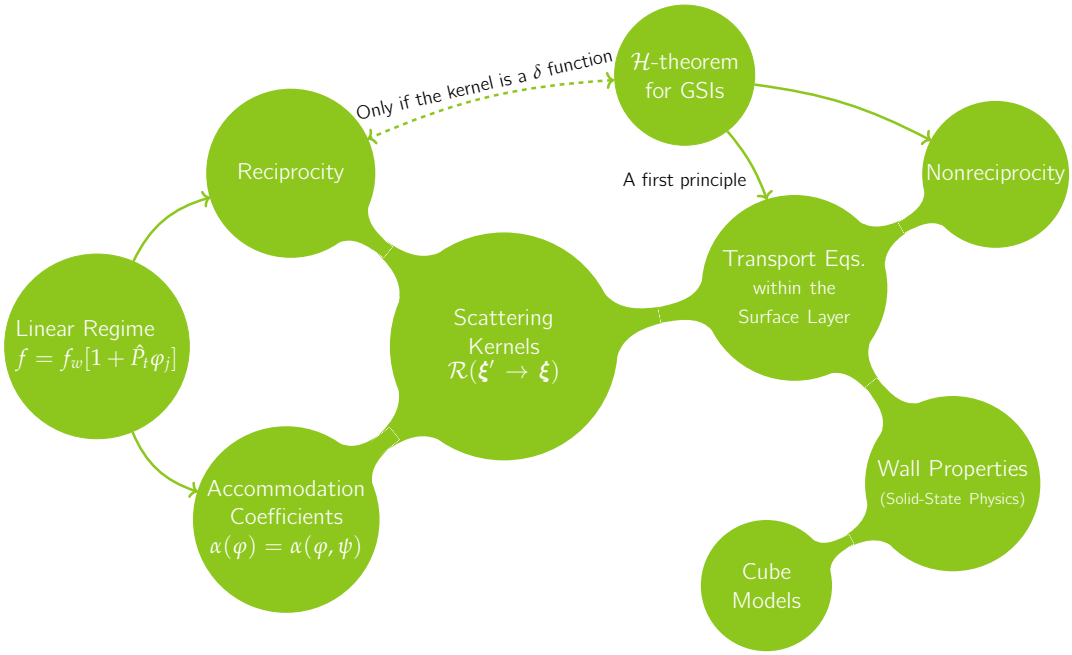

Figure 2.6: Summary of the theoretical background for GSIs.

2.4 Concluding Remarks

This chapter has systematically reviewed the essential theoretical underpinnings of GSIs, which are visually summarised in Fig. 2.6. Within the kinetic theory framework, GSIs are conventionally formulated through SKs. This formulation establishes a probabilistic connection between the incident and reflected molecular flux at the surface, incorporating adjustable ACs and adhering to reciprocity constraints. It is worth stressing, however, that the SK approach is primarily developed in scenarios with small deviations from equilibrium, specifically for linear flow regimes. Moreover, the general lack of a direct correlation between mathematical SKs and the fundamental physical properties of GSIs highlights the need for further research. This chapter has also reviewed physically-grounded representations of GSIs, ranging from simplified models considering binary collisions between gas molecules and effective surface cubes, to more comprehensive approaches involving solving kinetic equations in a thin surface layer based on first principles. Thus, this chapter paves the way for subsequent investigations to be discussed in this thesis, providing a solid foundation for interpreting the forthcoming simulation results.

Chapter 3

Molecular Dynamics for Modelling GSIs

Taking into account the complex physical properties and the many-body nature of GSIs, theoretical attempts for addressing GSIs are inherently challenging and demand a comprehensive understanding of the solid wall and detailed particle interactions. Yet, MD simulations, which reconstruct gas–surface scattering experiments within a computational environment, intrinsically embody the essential physics of GSIs, and offer additional insights into the development of kinetic boundary conditions through the analysis of deterministic trajectories.

This chapter commences with a brief overview of the MD simulation methodology (Section 3.1), crucial for understanding gas flow physics at the nanoscale. It describes the MD simulation setup for numerical scattering experiments of GSIs (Section 3.2), which enable the recording of comprehensive Lagrangian scattering data and capturing solid-state physics phenomena often overlooked in theoretical studies. Furthermore, this chapter discusses how Lagrangian data from the MD simulations were analysed (Section 3.3), providing not only macroscopic quantities such as velocity and temperature profiles of common interest but also the elusive scattering dynamics, specifically for the ACs and gas reflection patterns.

3.1 Molecular Dynamics Background

MD is a deterministic simulation method that integrates Newton's equations of motion for individual molecules in a system (Allen & Tildesley, 2017). This high-fidelity technique, capable of capturing complex phenomena like surface diffusion and rarefied effects, becomes essential for nanoflows where classical fluid dynamics assumptions break down. In this thesis, the open-source LAMMPS software package (Plimpton, 1995) is utilised for all MD simulations.

The fundamental principles of MD hinge on the calculation of forces and subsequent particle motion. The force acting on a particle is derived from the gradient of the potential energy ($\boldsymbol{F} = -\boldsymbol{\nabla} U$), and its motion is governed by Newton's second law ($\boldsymbol{F} = m\mathrm{d}\boldsymbol{\xi}/\mathrm{d}t$), where $\boldsymbol{\xi} = \mathrm{d}\boldsymbol{r}/\mathrm{d}t$. The velocity-Verlet algorithm (Swope, Andersen, Berens & Wilson, 1982), known for

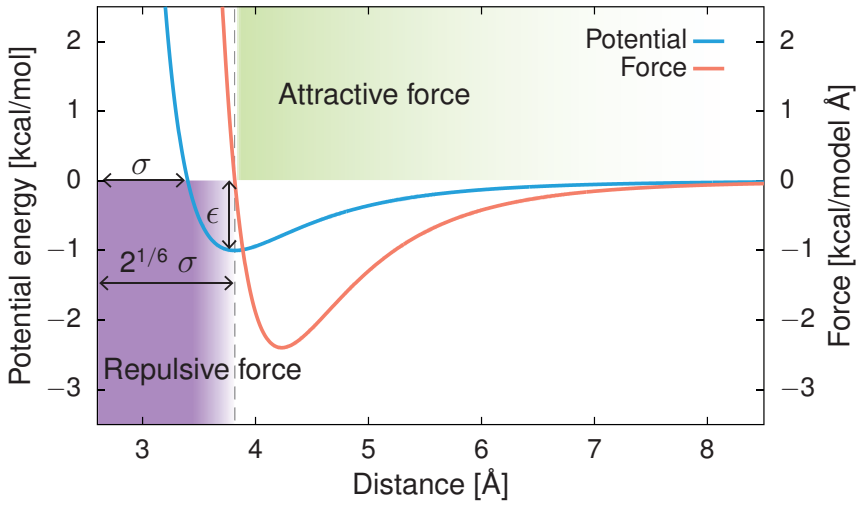

Figure 3.1: Lennard-Jones potential ($\sigma = 3.4$ Å, $\varepsilon = 1.0$ kcal/mol) and forces plotted as a function of interatomic distance.

its numerical stability and simplicity, is commonly employed for updating particle positions $\boldsymbol{r}$ and velocities $\boldsymbol{\xi}$. Moreover, this algorithm is precisely reversible in time (c.f. reciprocity for deriving SKs) and, under conservative forces, conserves linear momentum (Allen & Tildesley, 2017), which made it the preferred choice for GSI investigations in this thesis.

3.1.1 Intermolecular Potential

A key component in MD simulations is the intermolecular potential $U(r)$, defined as the potential energy between two particles separated by a distance r. In all studies presented in this thesis, all particles interact using a standard 12-6 Lennard–Jones (LJ) potential:

$$U_{\mathrm{LJ}}(r) = 4\varepsilon \left[\left(\frac{\sigma}{r}\right)^{12} - \left(\frac{\sigma}{r}\right)^{6} \right], \tag{3.1}$$

where σ is the distance at which the intermolecular potential is zero — approximately equal to the diameter of an atom d seen in Fig. 2.4(b), and ε is the depth of the potential well. As shown in Fig. 3.1, particles experience attractive forces at separations greater than $r > 2^{1/6}\sigma$, while at shorter distances ($r < 2^{1/6}\sigma$), the repulsive force predominates and is significantly stronger than the long-range attractive interactions. To balance accuracy with computational efficiency, the long-range interaction of the LJ potentials has been cut off at a distance $r_{\mathrm{cut}} = 3 \sim 4\sigma$, using the neighbour list algorithm, as is common in most MD studies.

The intermolecular potential, while not altering the state and energy equations in rarefied gases, plays a crucial role in characterising transport phenomena such as mass, momentum, and heat transfer. For instance, a hard sphere potential, which is usually the preferred choice in non-MD studies of rarefied gases, constrains molecules from approaching closer than their

diameter and dismisses any forces beyond a certain separation distance ($r > \sigma$). This leads to a different temperature dependence of viscosity compared to potentials with long-range interactions (Sharipov & Seleznev, 1998). Empirical comparisons, however, show that values derived from the LJ potential, parameterised from experimental viscosity data, closely align with those from *ab initio* potentials, which are calculated from first principles without empirical parameters (Sharipov, 2015). Such qualitative parallels suggest that adopting LJ potentials provides a highly reliable depiction of GSIs in the following scattering studies.

3.1.2 Boundary Conditions in MD

Appropriate boundary conditions are essential to approximate the behaviour of infinite or semi-infinite fluids within a finite MD simulation domain, effectively mirroring the characteristics of a more extensive system. Unlike computational fluid dynamics (CFD) simulations, where pressure and velocity are the typical boundary conditions facilitating continuous fluid flow, MD simulations often necessitate the careful addition and removal of atoms to maintain system stability (Borg, Lockerby & Reese, 2014; Borg, Macpherson & Reese, 2010). Here, three types of boundary conditions employed in this thesis study of GSIs are briefly introduced.

Periodic boundary conditions (PBCs) are used in MD simulations in the non-confined dimensions to emulate the properties of an extensive system within a finite domain. They operate under the premise that the domain is surrounded by identical replicas, allowing particles that exit one boundary to re-enter from the opposite with unchanged velocities. This approach conserves mass, energy, and momentum and facilitates the modelling of bulk properties in smaller systems. It is crucial, however, to ensure the domain dimensions exceed twice the cut-off distance r_{cut} to avoid finite-size effects and preserve the integrity of interatomic interactions.

Explicit walls, constructed from solid atoms, provide a tangible and realistic representation of solid boundaries in MD. These walls can reflect and adsorb gas molecules and be configured into various crystalline structures, such as face-centred cubic (FCC) and body-centred cubic (BCC), or represent porous media like organic kerogen surfaces. This modelling allows precise control over thermodynamic ensembles and surface roughness via wall atoms, offering insights into the dynamics of GSIs with a level of detail and realism.

Stochastic walls in MD, governed by SKs, present a computationally efficient alternative to explicitly modelled solid walls. These boundaries reflect gas particles based on predefined scattering laws, unlike PBCs that cyclically reintroduce particles into the domain. Essential for validating scattering dynamics, stochastic walls can be applied using the Box–Muller algorithm (Box & Muller, 1958), with methodologies exemplified by Lord (1991) for the CL model. Open-source particle simulation platforms like LAMMPS, with its EXTRA-FIX module, and SPARTA, designed for low-density gas simulations (Gallis, Torczynski, Plimpton, Rader & Koehler, 2014), also support these stochastic walls. This research enhances

LAMMPS's capabilities by integrating a custom implementation of the general form of SKs, as expressed by Eq. (2.28), using the Box–Muller algorithm. This customisation allows refined control of various scattering models to be implemented, which is crucial for in-depth GSI studies. See Appendix A for implementation details.

3.1.3 Ensembles and Thermostats

In MD simulations, thermodynamic ensembles serve as fundamental constructs that define the macroscopic constraints under which a particle system operates. An ensemble represents a group of possible microscopic states, such as the phase space of individual particles, that collectively exhibit consistent macroscopic properties like temperature, pressure, and volume. Ensembles enable us to model the behaviour of wall atoms and gas flows under various thermodynamic conditions, facilitating accurate predictions of scattering dynamics.

The *microcanonical* or NVE ensemble is one such example, representing an isolated system with a fixed number of particles (N), volume (V), and total energy (E). It can be applied to govern the evolution of gas phase space across a surface under thermal equilibrium, a scenario essential for ensuring reciprocity and thus crucial for the investigation of SKs.

The *canonical* or NVT ensemble maintains a constant number of particles (N), volume (V), and temperature (T), effectively mimicking a system in thermal equilibrium with a larger heat reservoir. Energy levels in this ensemble may fluctuate, but the overall temperature remains constant, providing a statistical framework for isothermal states. This ensemble is particularly useful for equilibrating systems at specific temperatures, such as wall atoms in GSIs, and is commonly used during the preparatory stages of MD simulations (refer to Section 3.2).

Temperature control within the NVT ensemble in MD is achieved through thermostats — algorithms designed to emulate heat exchange with an external reservoir by adjusting particle velocities. While uniform velocity modifications can provide basic temperature control, more sophisticated approaches, such as the Nosé–Hoover and Langevin thermostats, offer distinct adjustments to replicate the fluctuating energy exchanges seen in realistic thermodynamic systems. The Nosé–Hoover thermostat introduces an additional damping degree of freedom, altering the kinetic energy of the system to sustain a specific temperature. In contrast, the Langevin thermostat accounts for the interaction of the particles with a background medium and employs stochastic forces to mimic random thermal motion. This research employed both thermostats for their effectiveness in replicating the NVT ensemble. This is facilitated through the integration of the 'fix nvt' and 'fix langevin' commands in LAMMPS, respectively, enabling isothermal simulation runs and precise system equilibrations.

3.2 Basic Machinery — Scattering Experiments in MD

Having established the foundation for MD, this section now focuses on simulation setups relevant to GSIs. Specifically, it outlines the basic machinery for simulating gas flow systems confined between parallel walls. This setup is easily extensible to various scattering experiments, depending on the initialisation of gas particles and the chosen boundary conditions, while adhering to the standard MD workflow as illustrated in Fig. 3.2.

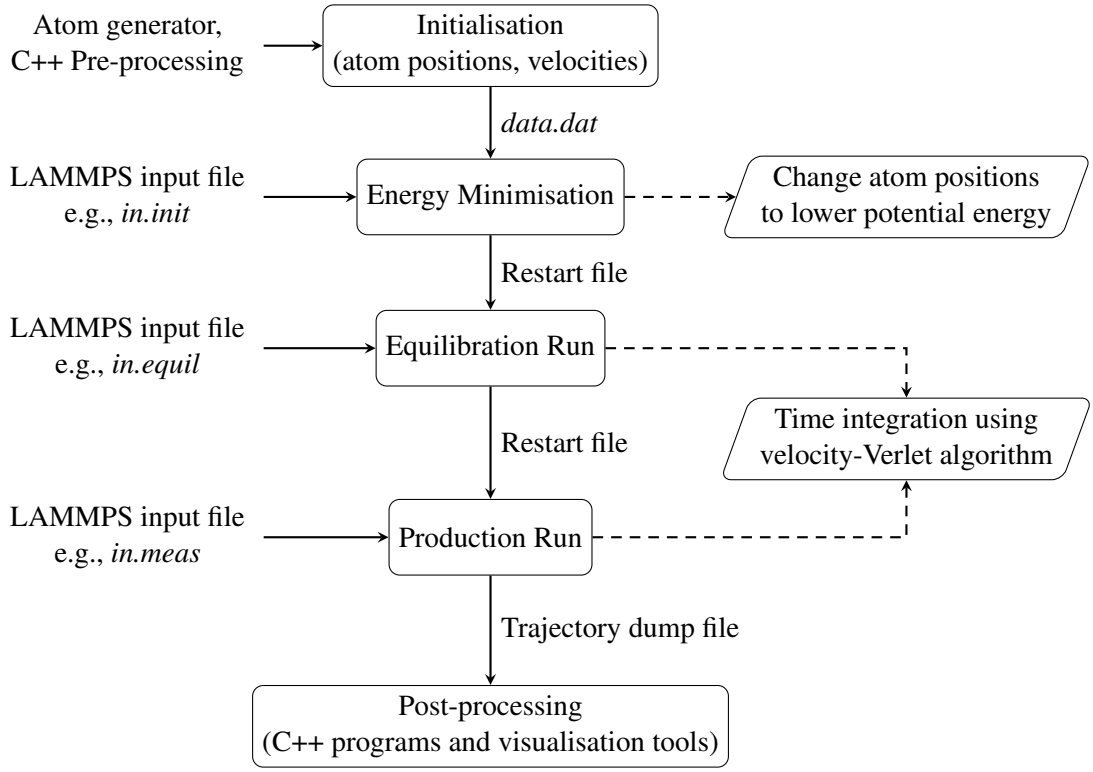

Figure 3.2: Flowchart showing the steps involved in an MD simulation using LAMMPS.

3.2.1 Initialisation

During the *initialisation* phase of the MD system, gas particles are uniformly distributed across the computational domain, ensuring their centres maintain a separation exceeding σ to prevent overlap. Overlapping particles can induce high repulsive forces, potentially leading to numerical instabilities, a phenomenon often referred to as 'simulation blow up'. This issue can be mitigated by reducing the simulation timestep, albeit at the cost of increased computational time. Furthermore, when focusing solely on GSIs, it is possible to switch off gas–gas interactions by significantly reducing the cut-off distance r_{cut} and energy scale ε. This allows for a more arbitrary, rather than uniform, particle distribution within the MD domain without risking simulation blow-up. Gas velocities are sampled using the Maxwellian distribution, employing the Box-Muller transform for realistic thermal beam simulations or

by specifying the same velocity for all gas particles for monoenergetic beam simulations, thus enhancing experimental versatility. In the non-confined dimensions, PBCs are used to effectively emulate a large system. In the direction of confinement, either explicit walls with solid atoms are set, whose initial velocities follow a Gaussian distribution, or stochastic walls are maintained at specified temperatures, aiding in the investigation and validation of scattering models. An in-house C++ code was developed to generate the initial configuration of atoms in a system, that produces a 'data.dat' file, which can be read in by LAMMPS for the first *energy minimisation* step.

3.2.2 Equilibration and Production Run

In the MD setup described in this thesis, gas particles are uniformly distributed, and wall atoms are arranged in their crystal structures across periodic boundaries, effectively preventing unphysical states like particle overlap. Consequently, the energy minimisation step shown in Fig. 3.2, which typically aims for a stable or low-energy configuration, is essentially pre-achieved during the initialisation; the constructed MD system inherently attains such a state.

Following energy minimisation, the system undergoes two critical dynamic phases: *equilibration* and *production*. Time integration during these phases updates particle velocities and positions. The gas and wall atoms are kept at a constant temperature during equilibration using thermostats, and explicit walls feature a rigid outer boundary to prevent self-movement.

Two types of MD simulations are carried out: equilibrium molecular dynamics (EMD) and non-equilibrium molecular dynamics (NEMD). In EMD, no external forces are applied to the gas molecules, with the primary focus on measuring gas–surface scattering dynamics. During the equilibration stage, EMD allows the gas properties to converge towards the required thermodynamic state through natural fluctuations. Conversely, NEMD simulates gas flows by applying external forces to the gas or creating temperature differences on the wall atoms, such as to mimic pressure or temperature gradients, respectively. In the equilibration of NEMD simulations, the gas properties for heat and flow are allowed to reach a steady state, thus examining the response of the system to external perturbations.

After equilibration and upon achieving steady-state conditions, the thermostat on the gas molecules is deactivated to prevent bias in their subsequent scattering dynamics. The production run then generates high-resolution Lagrangian data, including position ($\boldsymbol{r}$), velocity ($\boldsymbol{\xi}$), forces ($\boldsymbol{F}$), stress tensor (σ_{ij}), and energy (E), among others. This dataset provides detailed insights into the motion and properties of individual particles over time following post-processing, as discussed in the subsequent sections.

3.2.3 Post-Processing — Microscopic to Macroscopic

In this thesis, the post-processing of MD simulation data, specifically output from LAMMPS, is conducted using custom in-house C++ programs. These programs are tailored to extract molecular details and evaluate additional quantities not immediately measured during the equilibration and production phases.

Macroscopic properties such as density, pressure, temperature, and fluid velocity are calculated as weighted averages of microscopic molecular data. The simulation domain is partitioned into K rectangular cells of equal size, each serving as a volumetric sampling unit and aligned with the characteristic direction of the flow. For a given cell k with volume V_k, the number density is determined by the ratio of the number of particles it contains to its volume, as expressed by:

$$\langle n_k \rangle = \frac{\langle N_k \rangle}{V_k} = \frac{1}{SV_k} \sum_{j=1}^{S} N_k(t_j), \tag{3.2}$$

where S represents the total number of time samples, $N_k(t_j)$ the number of particles within the cell at sampling time j, and $\langle \cdot \rangle$ the time averaging operator.

Fluid velocity in particle-based simulations may be computed using various methods, as outlined by Tysanner and Garcia (2004). In this thesis, the cumulative average method is employed, providing an unbiased mean fluid velocity applicable to both EMD and NEMD, defined as:

$$\langle \boldsymbol{u}_k \rangle = \frac{\sum_{j=1}^{S} \sum_{i \in k}^{N_k(t_j)} \boldsymbol{\xi}_i(t_j)}{\sum_{j=1}^{S} N_k(t_j)}, \tag{3.3}$$

where the notation $i \in k$ indicates the index i ranging over the particles within cell k. Using the obtained velocities ($\boldsymbol{\xi}_i$, $\boldsymbol{u}_k$ and the peculiar velocity $\boldsymbol{c}_i = \boldsymbol{\xi}_i - \boldsymbol{u}_k$ within cell k), the translational temperature based on the equipartition theorem can be derived and measured (Allen & Tildesley, 2017; Landau & Lifshitz, 2013):

$$\langle T_k \rangle = \frac{m}{3k_B} \frac{\sum_{j=1}^{S} \sum_{i \in k}^{N_k(t_j)} |\boldsymbol{c}_i(t_j)|^2}{\sum_{j=1}^{S} N_k(t_j)}. \tag{3.4}$$

Pressure calculation follows a similar expression, involving the summation of the principal components of the per-atom stress tensor and averaging across all particles within the cell:

$$\langle p_k \rangle = -\frac{1}{3} \frac{\sum_{j=1}^{S} \sum_{i \in k}^{N_k(t_j)} \sigma_{11,i}(t_j) + \sigma_{22,i}(t_j) + \sigma_{33,i}(t_j)}{\sum_{j=1}^{S} N_k(t_j)}. \tag{3.5}$$

These evaluated macroscopic quantities, in turn, facilitate the understanding of the state and energy equations in rarefied gases and provide benchmark results for upscale kinetic solvers.

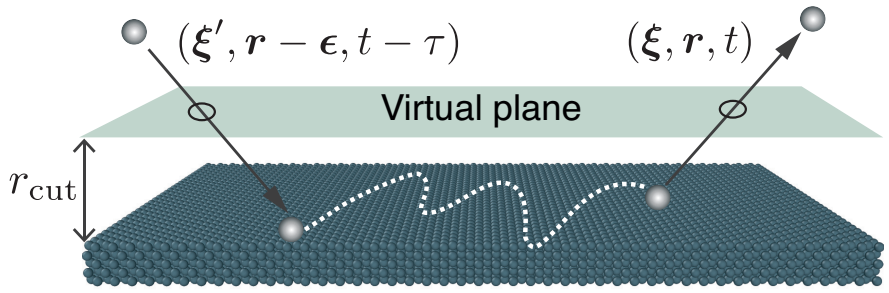

Figure 3.3: Schematic of the scattering dynamics of gas molecules near a smooth FCC surface. Scattering information for incident (e.g., $\boldsymbol{\xi}', \boldsymbol{r} - \boldsymbol{\epsilon}, t - \tau$) and reflected (e.g., $\boldsymbol{\xi}, \boldsymbol{r}, t$) molecules is recorded at the virtual plane.

3.3 Tracking GSIs

A key aspect of the post-processing involves defining and tracking GSIs. For flow systems modelled with hard-sphere potentials, such interactions are instantaneous and local, enabling the straightforward recording of pre- and post-collision states. However, for the continuous LJ potential employed in this study, which accurately models repulsive and attractive forces at wall interfaces, the definition of GSIs becomes less clear. To address this, a virtual plane parallel to the wall is introduced, located at a cutoff distance r_{cut} from the surface. Beyond this distance, the long-range attractive forces on gas molecules that stem from wall atoms are neglected. As illustrated in Fig. 3.3, when a gas molecule from the bulk crosses this virtual plane into the surface layer, its incident information (e.g., $\boldsymbol{\xi}', \boldsymbol{r} - \boldsymbol{\epsilon}, t - \tau$) is recorded. The same molecule is logged again when it re-crosses the plane back into the bulk, capturing the reflected information (e.g., $\boldsymbol{\xi}, \boldsymbol{r}, t$) and indicating the completion of a scattering event. The gathered scattering data from each molecule can thus be utilised to provide further physical insights, such as ACs related to momentum and energy exchange, and SKs constructed from velocity distribution functions. Furthermore, the surface layer encompasses all the fluid dynamics pertinent to GSIs, aligning precisely with the scenarios in the kinetic modelling of GSIs (refer to Section 2.2.4). By tracking the trajectories of molecules within the surface layer at every time step, the phenomena and properties of GSIs can be thoroughly investigated. This includes observing multiple collisions between gas molecules and wall atoms, resulting physisorption and surface diffusion phenomena, as well as the impact of surface temperatures and incident velocity distributions on scattering dynamics.

3.3.1 Velocity Correlations and Evaluation of ACs

After tracking GSIs, attention is shifted towards measuring the velocity correlations between incident and reflected molecular flux. This correlation is critical, as it can be depicted as a two-dimensional probability distribution profile for analysing scattering events, and subsequently assessing ACs and constructing SKs. Specularly reflective walls, for instance, manifest a pronounced correlation where incident velocities mirror their post-collision counterparts in magnitude, resulting in a distinctive diagonal trend in the correlation profile. Conversely, fully diffuse walls lose any incident velocity information, yielding a two-dimensional Gaussian profile indicative of randomised reflection. Observations from other wall models, including those explicitly modelled, typically fall between these two extremes, presenting a range of reflection characteristics.

Fig. 3.4 presents the velocity correlation and distribution profiles for the Ar-Pt system at 300 K, contrasting EMD against NEMD under varying external forces. In EMD depicted in Figs. 3.4(a-c), a notable correlation is observed between the incident and reflected velocities, as indicated by the linear least-squares fit (red solid line). This fit diverges from both the purely specular (dashed diagonal line) and fully diffuse (dashed horizontal line) scattering models. The slope of this fit, which quantifies the ACs, equals $1-\alpha$. Moreover, the velocity distributions for both incident and reflected molecules, shown in Fig. 3.4(d), maintain Maxwellian characteristics, reaffirming the equilibrium state of the system.

On the other hand, NEMD simulation of Poiseuille flow, characterised by small external forces, is depicted in Figs. 3.4(e-g). Notably, this setup aligns with scenarios noted by Kuščer (1971) and Bärwinkel and Schippers (1989), where non-equilibrium phenomena occur near the surface with the bulk solid acting as a heat bath. Strictly speaking, this scenario indicates a failure of reciprocity while still preserving a quasi-Maxwellian distribution. Scattering models remain applicable in such cases, and the MD setup becomes instrumental in investigating transport phenomena. Here, correlation profiles are shown to be similar to those in EMD, despite having a drift so subtle that it is visually almost imperceptible. Yet, this drift can be observed in the tangential velocity distributions in Fig. 3.4(h), evidenced by slight deviations in $f(\xi_{t_1}')$ and $f(\xi_{t_1})$ from the equilibrium state of the wall, i.e. $\mathscr{R}_{\mathrm{d}}(\xi_{t_1})$. Both distributions, nevertheless, align with the wall temperature.

In stark contrast, NEMD simulation with a large external force, as shown in Figs. 3.4(i-l), reveals a pronounced shift in scatter points toward higher velocities. This implies that the increase of surface temperature, indicated by Fig. 3.4(l), is due to energy transfer from the gas molecules. Such conditions are indicative of nonlinear flow regimes and nonreciprocity, surpassing the predictive capability of conventional SKs.

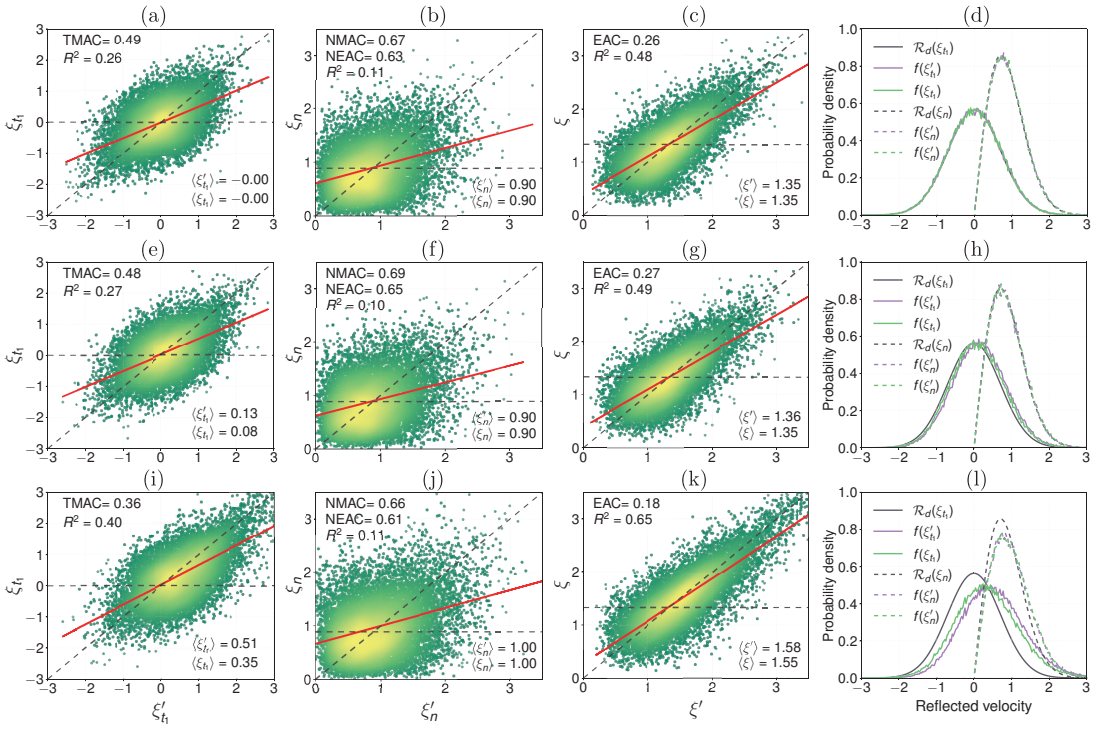

Figure 3.4: Velocity correlations between incident (x-axis) and reflected (y-axis) velocity components (ξ_{t_1}, ξ_n, ξ), along with their corresponding probability distribution profiles for the Ar-Pt system at a specified temperature of 300 K. Panels (a-d) illustrate EMD, while (e-h) depict NEMD under a force-driven Poiseuille flow in the low-speed case with a small velocity drift, and (i-l) present NEMD in the high-speed case with a large velocity drift. The dashed horizontal and diagonal lines represent the fully diffuse and specular cases, respectively. Red solid lines indicate the linear least-squares fitting through all scattering data.

Here, the post-processing procedure applied to scattering data for evaluating ACs can be clarified. The general form of ACs, as presented in Eq. (2.22), is as follows:

$$\alpha(\varphi) = \frac{\langle\varphi'\rangle - \langle\varphi\rangle}{\langle\varphi'\rangle - \langle\varphi_w\rangle}, \tag{3.6}$$

where $\langle\cdot\rangle$ denotes the mean value, and the subscript w implies that molecules are fully accommodated to the wall. This expression, still, is not exempt from intrinsic limitations, notably its dependence on incident velocity distributions in scenarios characterised by fluid drift or temperature gradients. Furthermore, it can lead to numerical inaccuracies, as observed in EMD when both incident and reflected velocity distributions are Maxwellian. Nonetheless, it is worth stressing that the latter limitation does not constrain the assessment of the TMAC; the condition $\langle\varphi_w\rangle = 0$ is maintained when $\varphi(\boldsymbol{\xi}) = \xi_{t_1}$ (or ξ_{t_2}), thereby ensuring computational precision in the evaluation.

As reviewed in Section 2.2.2, the inherent limitations of ACs can be effectively addressed post-reconstruction, provided the source of perturbation in the fluid flow aligns with the observed quantity. This situation leads to the reconstructed form of ACs, as presented in Eq. (2.27). Notably, this thesis confirms for the first time that the reconstructed form aligns precisely with scenarios where linear least-squares fitting is employed to assess ACs (Spijker, Markvoort, Nedea & Hilbers, 2010):

$$\alpha(\varphi) = 1 - \frac{\sum_i (\varphi_i' - \langle \varphi' \rangle)(\varphi_i - \langle \varphi \rangle)}{\sum_i (\varphi_i' - \langle \varphi' \rangle)^2}, \tag{3.7}$$

where the index i ranges over the scattering data. In the linear flow regime, where the averaged reflected quantity $\langle \varphi \rangle$ has a linear relationship with the corresponding averaged incident quantity $\langle \varphi' \rangle$, Eq. (3.7) provides ACs that do not depend on the incident distribution function, thus having a more objective physical meaning.

Three remarks are worth making in the analysis of velocity correlations and the evaluation of ACs. Firstly, within the linear flow regime, the overall velocity distributions, as shown in Figs. 3.4(d) and (h), may not serve as reliable indicators for GSIs. This is because the source of perturbation is generally weak in such scenarios, and the resulting non-equilibrium effects are not always readily discernible in distribution profiles. Instead, focusing on the velocity correlation profile and validating SKs from this data seems more effective. For enhanced clarity, selecting molecules whose tangential (or normal) velocity components are within the range of $[\xi', \xi' + \Delta\xi']$ — as if using a sliced dataset along the x-axis in velocity correlation profiles — allows a refined examination of scattering patterns through partial velocity distributions, which yield more discernible characteristics. Secondly, while the linear least-squares approach bypasses the intrinsic limitations of ACs, it fails to capture the velocity dependence of ACs essential for some SKs implementation, such as in the Epstein model. The expression from the general definition, Eq. (3.6), facilitates the evaluation of beam ACs and unveils this critical velocity dependence, akin to analysing partial velocity datasets in velocity correlation profiles. Lastly, it is noteworthy that linear least-squares fitting remains applicable beyond the linear flow regime, as illustrated in Fig. 3.4(i); however, the interpretation of ACs in this context must be approached cautiously. The transition of ACs (or correlation coefficient R^2) to differing values, as presented in Figs. 3.4(a), (e) to (i), signals a departure from conventional SKs suitability, necessitating more sophisticated methods, such as the kinetic approach within the surface layer, to accurately resolve the fluid dynamics at play.

3.4 Summary

This chapter presented the application of MD simulations and the setups used in this thesis for studying GSIs, effectively integrating both practical scattering experiments and theoretical concepts of kinetic boundary conditions into MD systems. It detailed the measurement processes that capture both macroscopic properties and crucial microscopic Lagrangian scattering data, thereby enriching our understanding of molecular interactions within nanoflow systems. Specific attention was given to velocity correlations, overall distributions, and ACs, as demonstrated through a case study highlighting the complex behaviours observed in response to various perturbations. It is worth stressing that the MD setups explored in this thesis focus on studying SKs under the linear flow regime, while they could serve as useful baselines for further investigations into the nonlinear flow regime. Integrating these setups with real-world experiments and kinetic solvers could establish MD as a crucial tool for advancing GSI research, solidifying its role as a benchmark within this field.

Finally, it should also acknowledge the computational expense involved in running these simulations, which were conducted on the ARCHER2 super-computing facility. For those interested in replicating or extending this research, example LAMMPS scripts and post-processing codes are provided in each subsequent chapter and are openly available in the GitHub repository ScatteringKernels, facilitating a deeper exploration of the methodologies employed.

Chapter 4

Methane Scattering and Mesopore Transport on Porous Kerogen Surfaces

N.B. This chapter has been published in: Chen, Y., Li, J., Datta, S., Docherty, S.Y., Gibelli, L., Borg, M.K. “Methane scattering on porous kerogen surfaces and its impact on mesopore transport in shale." *Fuel* 316, 123259 (2022)

Revealing the scattering behaviour of gas molecules on porous surfaces is essential to develop accurate boundary conditions for kinetic transport models that describe the gas dynamics in shale reservoirs. Here, high-fidelity molecular dynamics simulations are used to resolve the gas–surface interactions between methane molecules and realistic organic kerogen surfaces, and to assess the applicability of the widely used scattering kernels. These results show that the tight matrix porosities have a negligible effect on the timescale and lengthscale of the scattering process, which can be considered instantaneous in time and local in space. Although reflected velocity distributions reveal that the common Maxwell, Cercignani–Lampis and Yamamoto–Takeuchi–Hyakutake scattering models fail to fully capture the scattering details of methane near kerogen, especially when the incident molecular speeds are high, the Maxwell model predicts best the reflected angular beam pattern and the overall reflected velocity distribution for rough kerogen surfaces. However, for low-speed impingement, more characteristic of shale applications, all scattering models give similar velocity distributions, which are driven by the high degree of gas–surface accommodation observed. This research shows that a Maxwell model with a calibrated tangential momentum accommodation coefficient, which approaches unity as the surface roughness increases to ~ 2 nm, is enough to reproduce comparable velocity profiles and mass flow rates inside moderately confined kerogen mesopores. Deviations between the Maxwell model and the molecular simulations are only observed for highly rarefied transport problems, but this rarefaction lies beyond the realm of shale reservoir applications. This chapter reports the first scattering study on porous and rough kerogen surfaces, and demonstrates the applicability of the Maxwell model, which can be readily incorporated into gas kinetic solvers to predict the apparent permeability of shale with mesopore and macropore networks.

4.1 Literature Survey

The recent shale gas revolution is transforming the global energy sector. Understanding the fundamental engineering science underpinning the extraction of methane gas from shale reservoirs is, therefore, becoming increasingly important (Falk, Coasne, Pellenq, Ulm & Bocquet, 2015). Much of the unknown flow physics occurs at the micro/nano scales surrounding the organic kerogen structures (Guo, Xu, Wu, Wei & Liu, 2015; Shan, Wang, Guo & Wang, 2021; S. Wang, Javadpour & Feng, 2016a, 2016b), with micropores (< 2 nm) and mesopores (< 50 nm) being responsible for the major storage of methane in shale reservoirs. Moreover, adsorption (Huang, Gu, Li, Du & Liu, 2022; Liu, Hou & Wang, 2020) and diffusive/advective transport (Corral-Casas et al., 2021) must be accounted for within these pores, where the interplay between these processes remains unclear (Yang et al., 2019; L. Zhang, Shan, Zhao & Guo, 2019).

At a fundamental level, the physics at the micro/nano scales of shale applications is non-intuitive and depends on many physico-chemical phenomena. First, due to the large surface-area-to-volume ratio, the gas molecules interact as frequent with the pore surface as the interactions among themselves, which means effects like surface adsorption and surface diffusion can be significant. Secondly, because reservoirs operate at various pressures, from high (e.g. 50-100 MPa) all the way down to hundreds of kPa (Ziarani & Aguilera, 2012), there is a mix of dense and rarefaction effects in the different pores at different points in time of a reservoir's lifetime. The degree of rarefaction is generally described by the Knudsen number $Kn = \lambda/H$, where λ is the mean free path of the gas molecules, and H is the characteristic length of the flow system (such as the local pore width). Fluid flows in shale mesopores are in the slip $(0.001 < Kn < 0.1)$ and transition $(0.1 < Kn < 10)$ regimes (Freeman, Moridis & Blasingame, 2011), where the continuum assumption of classical flows is not valid, and transport properties can no longer be predicted accurately by the Navier-Stokes equations with no-slip boundary conditions (B. Cao, Sun, Chen & Guo, 2009; Jin & Firoozabadi, 2015). The Boltzmann equation and its model equations are applicable for mesopores, where confinement effects are negligible (e.g., $H > 7$ nm) (Sheng, Gibelli, Li, Borg & Zhang, 2020; Wu, Liu, Reese & Zhang, 2016). A number of kinetic solvers have been developed to solve the Boltzmann equation or a model of the kinetic equation, and to deal with various types of low-speed flows required in shale reservoirs, including in 3D geometries, such as the Direct Velocity Method (DVM) (Ho et al., 2019; P. Wang, Ho, Wu, Guo & Zhang, 2018), or the direct simulation BGK (DSBGK) method (Li, 2019). However, the overarching open question that has arisen in this field is whether an appropriate kinetic boundary condition exists for shale applications, which may contain molecular adsorption/desorption processes inside the tight porous surface.

These types of kinetic boundary conditions have been formulated for other engineering systems, such as for flows through micro-electro mechanical systems (MEMS) (B. Cao et al., 2009) or aerodynamics applications around very low earth orbits (Livadiotti et al., 2020). The way in which gas molecules scatter at a surface has led to several gas–surface interaction (GSI)

models, known also as scattering kernels (SKs), such as the Maxwell model (Maxwell, 1879) and the Cercignani–Lampis (CL) model (Cercignani & Lampis, 1971). Despite the recent emergence of these kinetic solvers in the field of shale gas modelling (Li et al., 2021), high fidelity scattering studies of shale rock surfaces are still missing.

The two questions tackled in this work are: (a) can existing SKs be used for shale, or new ones need to be developed? and (b) How do adsorption/desorption timescales, roughness and porosity of the organic kerogen affect the scattering dynamics of methane molecules? To answer both questions, high-fidelity molecular dynamics (MD) simulations of realistic kerogen samples are used to provide insights of the scattering physics and a baseline assessment of existing SKs. Analyses are also conducted to examine how the different SKs lead to distinct predictions of gas transport, through mesopores confined by kerogen surfaces.

The remainder of this chapter is organised as follows. The background of SKs for shale is described in Section 4.2. Section 4.3 introduces the methodology used in this work, including the MD set-up that resolves the scattering trajectories of methane gas molecules on kerogen surfaces. In Section 4.4, the MD results are used to answer the two questions above. Finally, the conclusions of this work and future outlooks are given in Section 4.5.

4.2 Scattering Models in Shale

As the scattering physics for kerogen/mineral surfaces remains poorly understood, there is a tendency to use simple SKs, such as specular-diffuse or backward-diffuse (i.e., the combination of backward and diffuse scattering) in shale applications (Ho et al., 2019; Moghaddam & Jamiolahmady, 2017; J. Wang, Chen, Kang & Rahman, 2016). However, the weighting factor of diffuse scattering in these kernels is often treated as a convenient tuneable parameter to fit the effective permeability of experiments, with used values ranging from 0.01 to 1.0 (Darabi, Ettehad, Javadpour & Sepehrnoori, 2012; Ma, Sanchez, Wu, Couples & Jiang, 2014; Moghaddam & Jamiolahmady, 2017; Wu et al., 2017) (i.e., ranging from purely frictionless surfaces to complete diffuse), which raises confusion in the implementation of SKs. For instance, Wu et al. (2017) claim TMAC should be as low as 0.5 and 0.1 to explain the experimental observation in the permeability-pressure curve. Beside the dispute about what TMAC value to choose, scattering on realistic shale surfaces should include the effects of porosity, roughness, adsorption, low-speeds flows and elevated pressures/temperatures, making it much different from the scattering on the controllable metal surfaces, on which most of SKs are developed (Liang et al., 2018; Wu & Struchtrup, 2017; Yakunchikov et al., 2012; Yamamoto, Takeuchi & Hyakutake, 2006; Yamamoto et al., 2007).

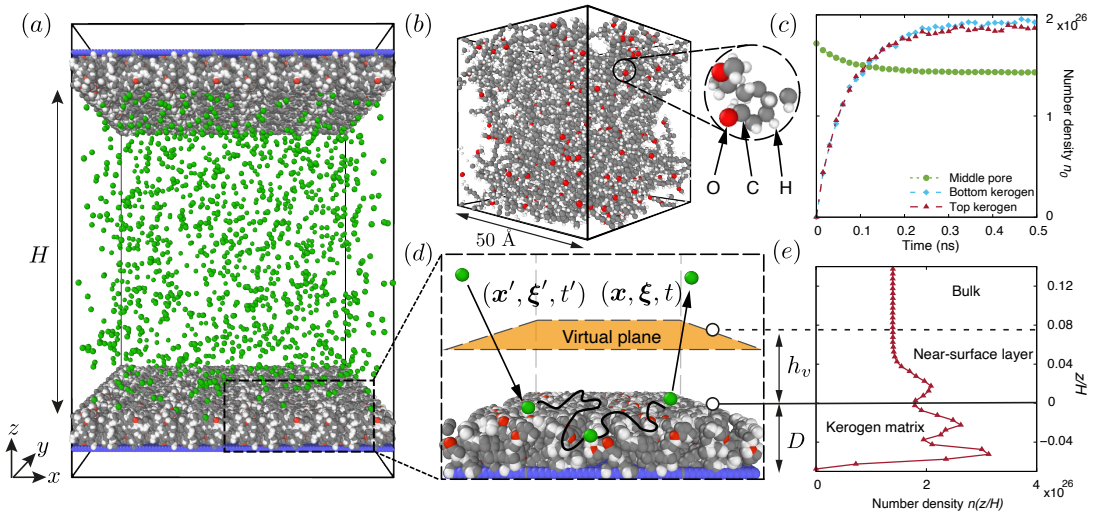

Figure 4.1: (a) Schematic of the MD domain, comprising methane flow through a quasi-2D pore slit constructed from two parallel kerogen walls with a width H = 20 nm; Colour legend: grey = carbon (C); white = hydrogen (H); red = oxygen (O); blue = outer-edge barrier (B); green = single-site methane (CH_4). (b) Kerogen structure EFK 0.8 g/cm^3 obtained from Bousige et al. (2016); (c) Number density of methane molecules in the bulk of the pore slit and inside the two kerogen walls during the equilibration run. (d) Schematic of the scattering process. Scattering information for incoming $(\boldsymbol{x}', \boldsymbol{\xi}', t')$ and outgoing $(\boldsymbol{x}, \boldsymbol{\xi}, t)$ molecules are recorded at the virtual plane (orange). (e) Number density profile of methane molecules across the pore slit after equilibration, corresponding to a bulk pore pressure $P_0 = 0.81$ MPa. Apart from the adsorption inside the kerogen matrix, monolayer adsorption is observed within the near-surface layer, which is defined by the distance h_v between the virtual plane (dashed line) and the kerogen surface (solid line).

In this work, the Maxwell and CL models are assessed, as they are both classical models capable of representing a broad class of SKs. Additionally, the Yamamoto–Takeuchi–Hyakutake (YTH) model (Yamamoto et al., 2007) is also examined, given that it integrates elements of these classical models.

4.3 Modelling and Methodology

4.3.1 MD Simulations

Fig. 4.1(a) shows the 3D MD set-up used in this work, which consists of methane stored inside a pore slit confined between two parallel kerogen walls. The distance between walls in the $z-$direction is taken to be the pore width H, while periodic boundary conditions are applied in the x, y directions. The kerogen samples used in this work are obtained from Bousige et al. (2016), which were constructed using hybrid reverse Monte Carlo and MD simulations to match experimental properties, such as the pore size distribution, C-C pair distribution function and elastic properties. In this work, results are presented for the Eagle Ford field kerogen

Table 4.1: Interatomic Lennard Jones potential parameters (σ, ε) used in our MD simulations. Potential parameters for pairs of species not shown in the table are taken to be zero.

Atom pairs	σ [Å]	ε [kcal/mol]
CH_4 - CH_4	3.730	0.2941
CH_4-B	3.545	0.0050
CH_4-C	3.545	0.1279
CH_4-H	3.075	0.0936
CH_4-O	3.450	0.2135

(EFK), which is a low-maturity organic sample taken from a carbonate-rich shale reservoir. However, as discussed in Section 4.4, no significant differences in the scattering results are expected when considering other kerogen samples. The molecular structure for EFK has been calibrated for four different densities (i.e., porosities ϕ): 0.8 g/cm^3 (45%), 1.0 g/cm^3 (35%), 1.2 g/cm^3 (24%) and 1.4 g/cm^3 (14%) (Bousige et al., 2016). Each kerogen sample has a unit box size of 50 Å, as shown in Fig. 4.1(b). To achieve more statistics in our measurements, and apply more controlled edits to the surface roughness (see Section 4.4.2), the EFK sample was replicated in the x, y directions using multiples of its length, 50 Å. However, the thickness of the kerogen slab D, is taken to be smaller than 50 Å to save on computational cost, since the scattering pattern is found to be independent of D when it is set larger than the interaction cut-off distance between gas molecules and surface atoms. To set the temperature of the kerogen samples, while keeping their structure similar to their equilibrium calibrated condition, a spring force is applied independently to each kerogen atom. The spring force tethers each atom to its initial position, at which the motion of each atom is solved using Langevin dynamics, with a damping parameter of 50 fs. Besides the kerogen structure, each parallel wall has a rigid single-layer barrier (B), which prevents any loss of methane molecules from the computational domain. Methane (CH_4) molecules are modelled using a monatomic model (Bousige et al., 2016), which has been calibrated in previous work to describe the properties of methane as well as its adsorption in kerogen, as shown by experiments (Bousige et al., 2016).

In these MD simulations, the velocity-Verlet algorithm with a time step of 0.5 fs was used to integrate the molecular trajectories, and all atoms (except the atoms in the kerogen matrix) interact using a standard 12-6 Lennard-Jones (LJ) potential. The interaction parameters for all species considered in our MD simulations, which again are obtained from Bousige et al. (2016) and Obliger, Ulm and Pellenq (2018), are listed in Table 4.1. The interactions between the kerogen atoms (i.e., C-C, H-H and O-O) are substituted by a tethered harmonic spring force with a fixed spring constant 100 kcal/(mol Å^2) and a Langevin dynamics model. The value for ε_{CH_4-B} is taken to be very small ~ 0.005 kcal/mol, which is an order of magnitude smaller than the kerogen-methane interactions. The small value of B-CH_4 interaction is necessary to avoid molecules from leaving the computational domain, and acts like a specular wall. To balance

accuracy with computational efficiency, the long range interaction of the LJ potentials are cut-off at a distance $r = r_c$ = 15 Å, using the neighbour list algorithm. This is within standard cut-off lengths of $r_c = 3 \sim 4\sigma$, around which the degree of accommodation for the GSI was shown to be invariant (J. Sun & Li, 2008).

Each MD simulation run consists of two steps, namely an equilibration run and a production run. Initially, methane is placed only in the kerogen slit, and then the system is equilibrated for 0.5 ns at a constant temperature of 423 K, which is a value that can be reached in shale reservoirs (Falk et al., 2015; Obliger et al., 2018). As shown in Fig. 4.1(c), this is enough time to allow methane molecules to adsorb inside the kerogen sample and reach a steady state in the considered cases, although the time for methane to adsorb is also proportional to the kerogen thickness and pressure within the slit pore (R. Wang et al., 2023; R. Wang, Li, Gibelli, Guo & Borg, 2021). During equilibration, the temperature of methane is kept constant using a Nosé-Hoover thermostat with a time constant of 100 fs in the NVT ensemble. Following equilibration, the MD simulation is run for a further 2-4 ns to produce the scattering data (see Section 4.3.2). During the production run, temperature control on the methane molecules is switched off, so not to bias their scattering dynamics.

4.3.2 Tracking Gas–Wall Collisions

The definition of GSI from these deterministic simulations relies on tracking the gas molecules' positions and velocities at every time step, and selecting molecules that undergo a collision with the wall. For a hard-sphere fluid this is straightforward, since a collision with the wall happens instantaneously, thereby making it easy to obtain $\boldsymbol{\xi}'$ and $\boldsymbol{\xi}$, while $\boldsymbol{x}' \approx \boldsymbol{x}$ and $\tau \approx 0$. However, for the continuous LJ potential considered in this work, which is required to accurately model the adsorption force field of the organic matrix, the definition of a wall collision is ambiguous. Here, as shown in Fig. 4.1(d), a *virtual plane* is placed parallel to the surface of the wall at a distance h_v, beyond which the long-range attractive force of the kerogen's atoms are no longer felt by methane molecules, i.e., $h_v = r_c$. The *near-surface layer* within h_v will also contain adsorption and molecule ordering, as indicated in Fig. 4.1(e). When a gas molecule crosses the virtual plane from bulk and into the near-surface layer, the molecule's position, velocity and time are recorded $(\boldsymbol{x}', \boldsymbol{\xi}', t')$, which is the incident particle information. The molecule will also be recorded again when it crosses the virtual plane back into the bulk $(\boldsymbol{x}, \boldsymbol{\xi}, t)$, which represents the reflected particle information. As illustrated in Fig. 4.1(d), the crossings of molecules across the virtual plane will contain modelling details about the GSI, and consequently, the incident and reflected information for every molecule colliding with the wall can be readily used to provide further physical insights, such as in the residence time and velocity distribution functions.

4.4 Results and Discussions

4.4.1 Effect of Porous Surfaces on Gas Scattering Theory

As discussed in Section 2.2.1, the most widely used SKs rely on the assumption that molecules striking the surface are instantaneously re-emitted from the impact position; i.e., $\boldsymbol{x}' = \boldsymbol{x}$ and $\tau = 0$. These assumptions, however, are questionable when considering porous surfaces, such as in organic matter considered here, in which a larger number of gas molecules can adsorb and desorb in the interstices of the microscale-thick matrix (Shan et al., 2021), and diffusion playing a dominant role in the sorption processes. To assess the influence of a porous surface, especially on whether the assumption of negligible residence time and position locality of the GSI breaks down, a series of validation tests are conducted on these organic kerogen surfaces.

First, kerogen surfaces with various densities (or porosities) are investigated. The residence time τ of gas molecules within the near-surface layer (and the porous kerogen matrix) is measured, which is given as the time interval $\tau = t - t'$. Fig. 4.2(a) shows the results as a time distribution normalised by the characteristic time, i.e., the inverse of the gas–gas collision frequency $\tau_c = \sqrt{m/(\pi k_B T_0)}/4n_0\sigma_0^2$, where k_B is the Boltzmann constant, and T_0, σ_0 are the temperature and diameter of the methane molecules, respectively. Although the peaks of the normalised residence time distributions are not strictly close to zero, most of the gas molecules are re-emitted from the kerogen surface in a timescale $t^* = \tau/\tau_c$ smaller than unity, indicating the assumption of instantaneous scattering turns out to be reasonable. Note that this conclusion also depends on how the characteristic time τ_c has been defined, which is relative to the value of the gas number density n_0. It is seen that the time distribution curves almost coincide with each other, which indicates that the kerogen's matrix porosity has a negligible influence on the timescale of the re-emitted gas molecules. In this respect, one can further envision that any desorbed molecules, which were adsorbed inside the kerogen for a long time, only contribute to a very small percentage of wall scattering events.

Next, systems with different bulk pore pressures P_0 are considered, which are obtained by varying the number of methane molecules in the system. Note that in the considered range of pressure [0.37 – 3.92] MPa, the fluid is only slightly non-ideal, as the reduced number density is much smaller than unity. This remark can also be supported by evaluating the value of the compressibility factor (Shan et al., 2021) that turns out to be about 0.9882. This clearly proves that one can safely apply the ideal equation of state and, therefore, the Knudsen number of the molecular system can be evaluated as $Kn = \sqrt{2}/(2\pi H n_0 \sigma_0^2)$ for simplicity. Here, the corresponding Knudsen numbers considered lie in the transition regime. As the characteristic time τ_c used for the normalisation decreases with increasing P_0, a peak with $t^* > 1$ will be observed for high pressures (e.g., $P_0 = 3.92$ MPa in Fig. 4.2(b)), which means the timescale of

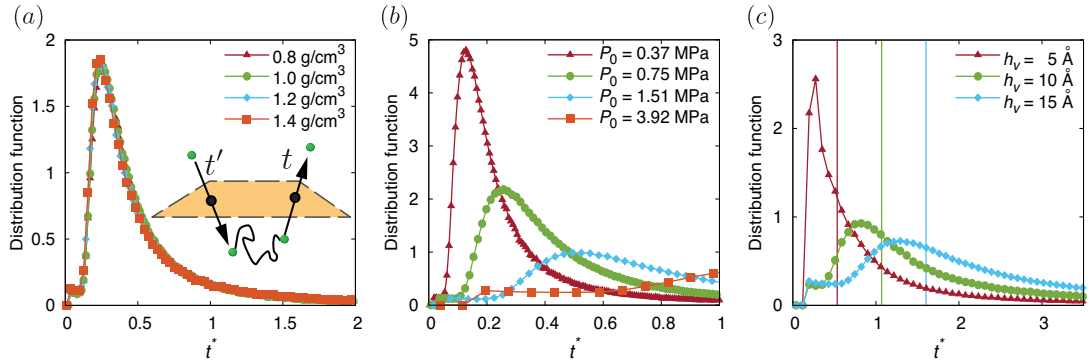

Figure 4.2: Distribution function of the nondimensional residence time ($t^* = \tau/\tau_c$) during the scattering of methane molecules inside the near-surface layer. The comparisons are performed for (a) various EFK kerogen porosities at a fixed bulk gas pressure ($P_0 = 0.95$ MPa) within the pore slit, (b) molecular systems of various pressures on kerogen structure EFK 0.8 g/cm^3, corresponding to $Kn = 1.28, 0.64, 0.31, 0.12$, respectively, and (c) various near-surface layer thicknesses at P_0 = 3.92 MPa on EFK 0.8 g/cm^3. Vertical lines represent the estimated time for molecules to cross the near-surface layer twice ($2h_v$) without considering adsorption, at a velocity $\sqrt{2\pi k_B T_0/m}/2$.

most molecules resident within the near-surface layer is larger than the timescale of gas–gas interactions. In Section 4.4.4, the impact of $t^*_{\text{peak}} > 1$ for these high pressure cases was found to be negligible on the gas transport in a moderately confined pore slit with a size of 20 nm, and this impact is expected to be even smaller for larger pore sizes.

To explore further the contributing factors of t^*, the focus is on the high pressure gas case, and the virtual plane is placed at 5 Å, 10 Å and 15 Å away from the surface, respectively. This is purely a theoretical exercise, to demonstrate the sensitivity of the virtual plane location on t^*, and mechanisms leading to larger t^*. Fig. 4.2(c) shows that the residence time for the highest probability of scattering t^*_{peak} is lowered when the thickness of the near-surface layer h_v is reduced, which indicates that molecules spend less time travelling to the wall and back. Additionally, the average travelling time of molecules from the virtual plane to the wall and back is estimated using the normal component of the average velocity of diffusely reflected molecules $\sqrt{2\pi k_B T_0/m}/2$, with results shown as vertical lines in Fig. 4.2(c). Although porosities and attractive forces between gas molecules and surface increase the average residence time of molecules (Butt et al., 2003), the vertical lines closely match the t^*_{peak} of the respective curves, which indicates that most molecules are spending their time travelling in the near-surface layer in a quasi-collisionless state. The long tail of t^* highlights the few molecules that remain in an adsorbed state (or where gas–gas molecular interactions exist) with increased residence time. These tests prove that molecular adsorption has a small influence on the peak timescale of scattering t^*_{peak}. As shown in Figs. 4.3(a-c), a similar test has been performed in terms of the transverse scattering lengthscale. The displacement $L = \|\boldsymbol{x} - \boldsymbol{x}'\|$ of one molecule undergoing a scatter event has been evaluated and normalised by the mean free path λ of the

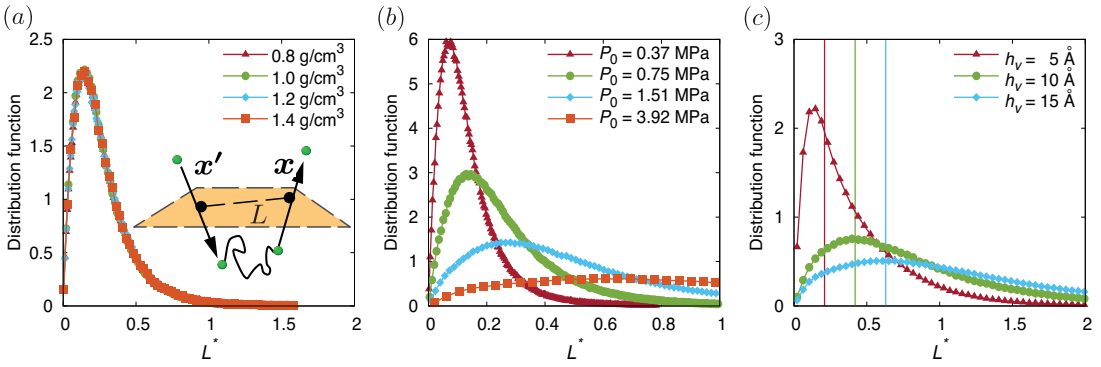

Figure 4.3: Distribution function of the nondimensional displacement ($L^* = L/\lambda$) during the scattering of methane molecules inside the near-surface layer. The comparisons are performed for (a) various EFK kerogen porosities at a fixed bulk gas pressure ($P_0 = 0.95$ MPa) within the pore slit, (b) molecular systems of various pressures on kerogen structure EFK 0.8 g/cm^3, corresponding to $Kn = 1.28, 0.64, 0.31, 0.12$, respectively, and (c) various near-surface layer thicknesses at P_0 = 3.92 MPa on EFK 0.8 g/cm^3. Vertical lines represent the thickness of the near-surface layer h_v.

gas molecules, i.e., $L^* = L/\lambda$. The magnitude of the displacement still largely depends on the thickness of the near-surface layer h_v, as indicated in Fig. 4.3(c), and similar arguments can be made about L^*_{peak}. Since both L^* and t^* are sensitive to the choice of h_v, this dependence raises the question about the appropriate location of the boundary in transport simulations using a scattering model, i.e., whether it should be defined at $z_0 = 0$ (as is more practical and also reduces t^*, L^* values below 1) or $z_0 = h_v$ (as is theoretically more accurate), which is discussed later on.

4.4.2 Origins in the Gas–Surface Accommodation

Although conventional SKs can still be used for shale applications, the degree of accommodation for momentum and energy of gas molecules with the surface needs to be investigated in the form of accommodation coefficients (ACs), to understand the scattering dynamics and suggest a suitable model. In this study, general ACs are calculated using all the incident molecules irrespective of their velocity magnitude, while beam ACs are evaluated by taking molecules with their component of incident velocity in the range $[\xi', \xi' + \Delta\xi']$, where the small increment $\Delta\xi' = 0.1$. Since the scattering dynamics is assumed to be decoupled in the tangential and normal directions, ξ' can be referred as the tangential velocity component ξ'_{t_1} or the normal velocity component ξ'_n depending on the coefficient to be evaluated. Note that the velocities are normalised by the most probable speed $\xi_m = \sqrt{2k_B T_w/m}$.

Extensive experimental (Agrawal & Prabhu, 2008; Thomas & Lord, 1974) and simulation work (Spijker et al., 2010; J. Sun & Li, 2011; Yamamoto et al., 2006) have been conducted to find the relation between the ACs and their influencing factors, such as gas temperature, gas molecular mass, surface topography, as well as the strength of the gas-surface intermolecular

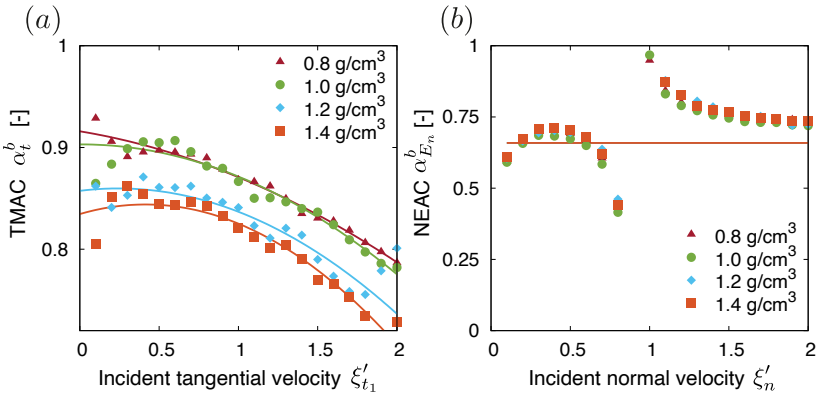

Figure 4.4: Beam ACs calculated by MD simulations on kerogen structure EFK with different densities/porosities. Variation of (a) beam TMACs α_t^b, and (b) beam NEAC α_{En}^b due to different incident velocities on the clean cut kerogen surfaces.

force field. To investigate the role of roughness on these porous surfaces, a distinction is made between (a) *microscopic roughness*, which is inherent due to the micro porous nature of the kerogen, and (b) *mesoscopic roughness*, which stems from the mesoscopic topography of the surface. Realistic kerogen surfaces have both microscopic roughness (which is mostly dictated by local porosity) and mesoscopic roughness at the interface between the kerogen matrix and the larger mesopore matrix. The influence of the microscopic roughness is shown in Fig. 4.4(a) for clean-cut kerogen samples. The results show that scattering on a higher density kerogen, results in a lower degree of tangential momentum accommodation, due to the lower porosity (i.e., microscopic roughness). In Fig. 4.4(a), a lower TMAC is also observed for molecules with higher incident velocities, which is consistent with the literature (B. Cao et al., 2009; Yamamoto et al., 2007). However, as seen in Fig. 4.4(b), there is a negligible effect of a kerogen's microscopic roughness on the degree of accommodation for the kinetic energy normal to the surface. This may occur because the exchange of energy between methane molecules and kerogen atoms represented by $\alpha_{E_n}^b$ mostly depends on the intermolecular force field and the fluid-wall mass ratio, which remain relatively constant across kerogen samples. A singular-like behaviour can be observed when the impinging velocity is close to the most probably speed. However, this behaviour is a numerical artefact that is likely due to the numerical inaccuracies arising in this condition as both numerator and denominator in Eq. (2.22) approach to zero (Cercignani, 1988; Spijker et al., 2010; Yamamoto et al., 2007).

In this work, the mesoscopic roughness is controlled in a simple, albeit unphysical way, by carving the kerogen sample using a two-dimensional corrugated surface:

$$\Delta z = \frac{A}{2}\left[\sin\left(\frac{2\pi x}{p}\right) + \sin\left(\frac{2\pi y}{p}\right)\right]. \tag{4.1}$$

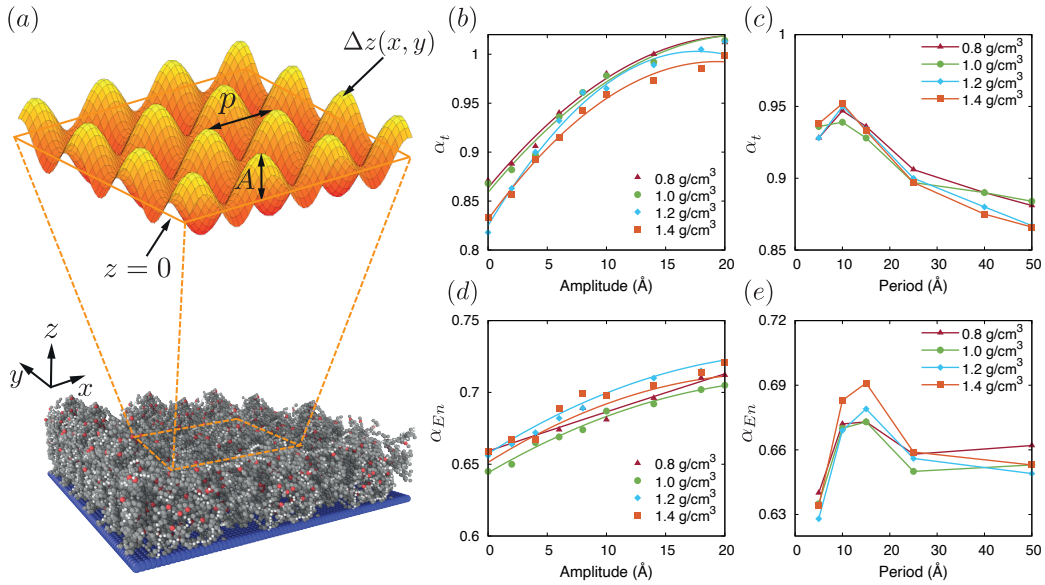

Figure 4.5: The effects of mesoscopic roughness on the degree of accommodation. (a) Schematic of the mesoscopic roughness on EFK kerogen structure, achieved by a 2D corrugated surface (orange). Variation of general TMACs due to different (b) roughness amplitudes A with period p = 25 Å, and (c) roughness periods p with A = 4 Å. Variation of general α_{E_n} due to different (d) roughness amplitudes A with p = 25 Å, and (e) roughness periods p with A = 4 Å.

This simplified approach provides insights into the sensitivity of roughness on the ACs, and the expected transition from a partial to a fully-accommodating wall. According to Eq. (4.1), and shown also in Fig. 4.5(a), the topographic roughness is determined by two parameters, i.e., the amplitude A and the period p of the corrugated surface. The pore width, H thus is defined as the distance between the centrelines (i.e., $z = 0$ on bottom and $z = H$ on top) of the sinusoidal curves, or between the centre of the outermost atoms for limiting cases with no mesoscopic roughness (i.e. when the amplitude A = 0). Figs. 4.5(b,c) show that with increasing amplitude and smaller period of mesoscopic roughness, the TMAC rapidly increases and approaches unity. More importantly, since the porosity of the considered samples (ϕ = 14% - 45%) has a small effect on TMAC, then the limiting cases with no mesocopic roughness, which have a TMAC > 0.8, lead to the conclusion that a high degree of accommodation for tangential momentum will be a common feature for any type of kerogen surface. Note that this conclusion becomes even more accurate for lower reservoir temperatures (i.e., $T_w < 423$ K), which also can be found in shale applications, as the ACs (e.g., TMACs) generally become larger at lower T_w (B. Cao et al., 2009). Compared to the tangential momentum, the amplitude and period of the mesoscopic roughness have less influence on the accommodation of normal kinetic energy, as shown in Figs. 4.5(d,e).

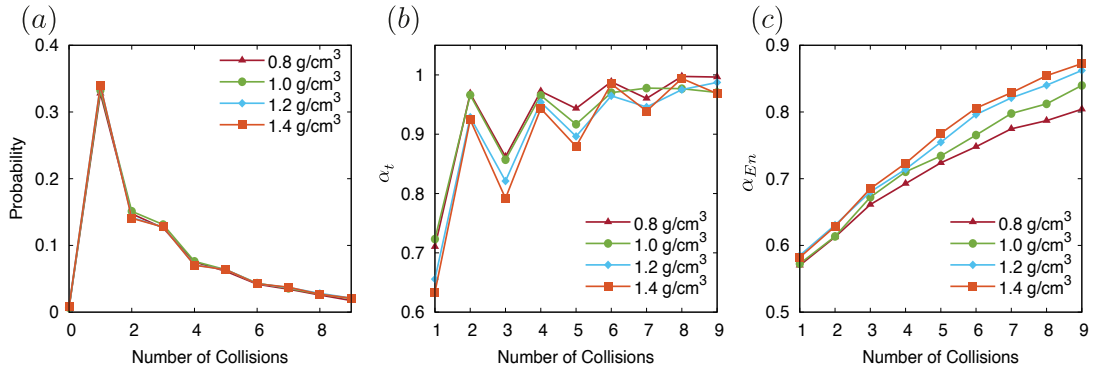

Figure 4.6: Distribution of the number of collisions during the scattering of methane molecules inside the near-surface layer on EFK kerogen samples, without considering the mesoscopic roughness for pressure P_0 = 0.75 MPa (a) Probability density distribution of number of collisions. (b) The TMAC versus number of collisions. (c) The accommodation of the normal kinetic energy versus number of collisions.

Generally, momentum and energy is exchanged between gas molecules and the surface during collisions. Therefore, the number of collisions suffered by gas molecules with the surface during their residence time offers further insights on the dependence of ACs on the molecules' impinging patterns (i.e., single or multiple collisions). Fig. 4.6(a) shows that a methane molecule may collide with the surface atoms more than once. Moreover, for the scattering process, about a third of methane molecules undergo a single collision, whereas most of them collide with the surface multiple times, thus losing memory of their incoming velocity. This high probability of multiple collisions is also found to be mostly independent on the porosity of the kerogen surface. Figs. 4.6(b,c) show that, under a fixed number of collisions, a higher TMAC was obtained for the kerogen surface with a higher porosity (microscopic roughness), while α_{E_n} decreases with porosity. Moreover, the TMACs approach unity rapidly with an increasing number of collisions, whereas the increase of accommodation of normal kinetic energy α_{E_n} is much slower. This difference in accommodation verifies the idea that momentum is being lost or gained much faster than energy in physical interactions (Cercignani, 1988). Finally, Fig. 4.6(c) shows that, in the first few collisions that cover most cases of scattering situations, α_{E_n} on kerogen surfaces with various microscopic roughness are close to each other, which explains why the beam $\alpha^b_{E_n}$ (Fig. 4.4(b)) and general α_{E_n} (Figs. 4.5(d,e)) are relatively constant across kerogen samples.

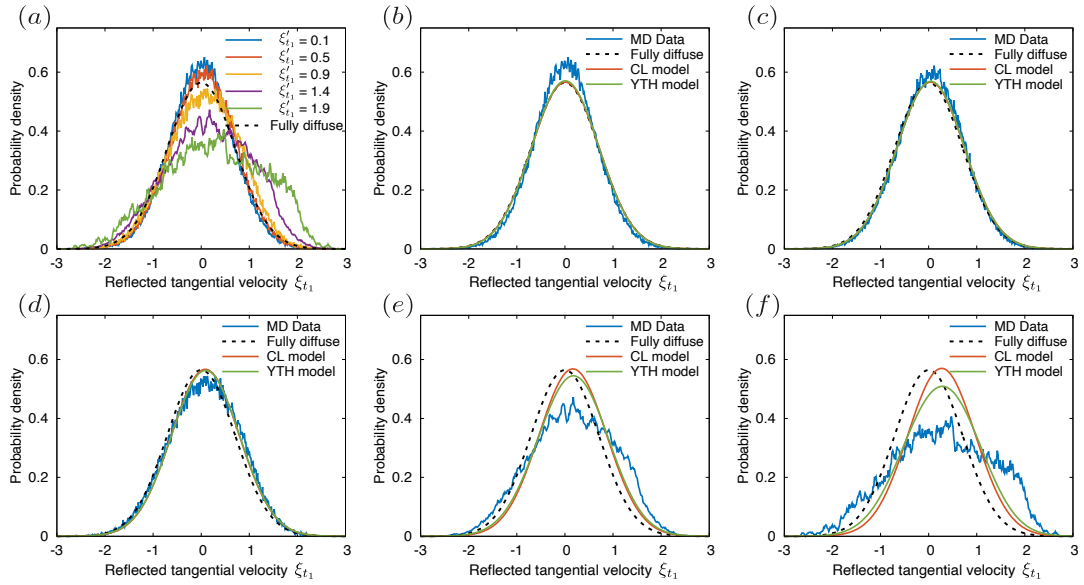

Figure 4.7: Comparison of reflected tangential velocity distributions predicted by MD and existing SKs with ACs obtained by MD. (a) MD results due to various incident velocity magnitudes; (b) $\xi'_{t_1} = 0.1, \alpha_t^b = 0.9230$; (c) $\xi'_{t_1} = 0.5, \alpha_t^b = 0.9194$; (d) $\xi'_{t_1} = 0.9, \alpha_t^b = 0.9024$; (e) $\xi'_{t_1} = 1.4, \alpha_t^b = 0.882$; and (f) $\xi'_{t_1} = 1.9, \alpha_t^b = 0.8581$. Note that the Maxwell model with a calibrated TMAC is not presented, as the spike-like pattern of specular reflection is clearly not observed in our MD results. All the MD results are obtained from the scattering on kerogen structure EFK 0.8 g/cm^3 with roughness amplitude A = 4 Å, period p = 25 Å.

4.4.3 Deviations of Velocity Distributions from Conventional Kernels

SKs can be assessed by comparing the predicted scattering pattern of a molecular beam against MD simulation results. Here, the ACs that enter in the SKs (i.e., the Maxwell, CL and YTH models) are given the values obtained by the MD results (Fig. 4.4). Similar to the evaluation of beam ACs, a sample is taken of incident molecules with a velocity between $[\xi', \xi' + \Delta\xi']$, where the small increment $\Delta\xi' = 0.1$, to investigate the velocity distribution after reflection for these molecules only. Here, normalised velocities 0.1, 0.5, 0.9, 1.4 and 1.9 are chosen. Fig. 4.7(a) shows the reflected velocity distributions for all the incident velocities considered. The results show that the tangential velocity distributions at small incident velocities are nearly symmetric and their centrelines are close to $\xi_{t_1} = 0$. Figs. 4.7(b-d) show that all the SKs provide relatively good fits to those distributions resulting from small incident velocities, which are expected due to the high TMACs. Small discrepancies are only observed for the small ξ_{t_1}, indicating that the magnitude of the tangential velocity is partially retained during the scattering process. By contrast, Figs. 4.7(e,f) show that no existing SK could reproduce a distribution for molecules with high incident velocity. These disagreements at high incident speeds were also found for scattering of Xe atoms on GaSe (Bruno, Cacciatore, Longo & Rutigliano, 2000), and N_2 on Pt surface (Yamamoto et al., 2007). In addition, a Maxwell or Epstein model contains a component

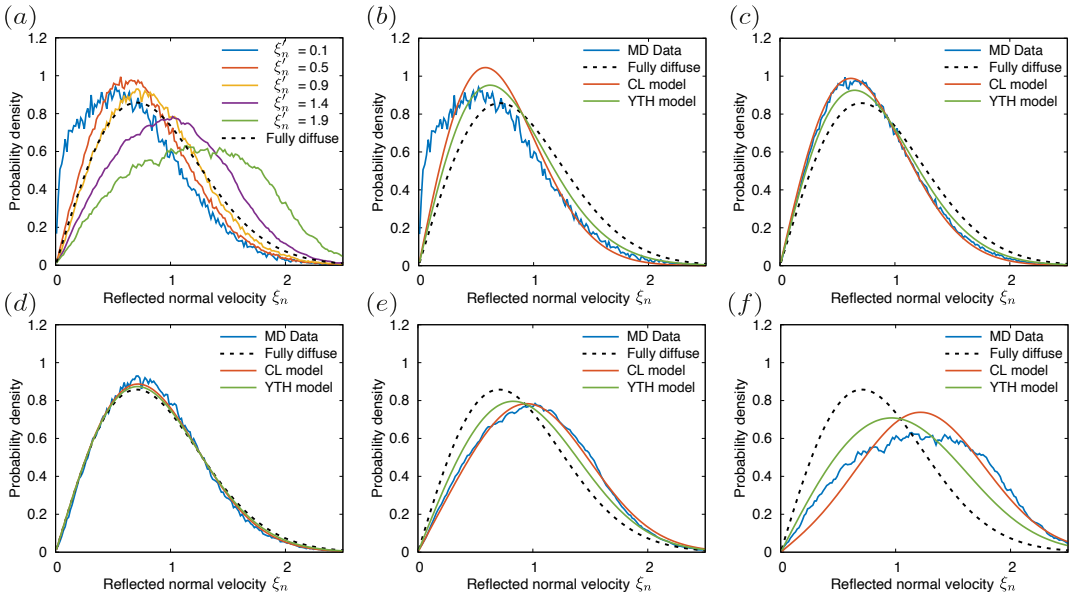

Figure 4.8: Comparison of reflected normal velocity fluxes predicted by MD and existing SKs with ACs obtained by MD. (a) MD data due to various incident velocity magnitudes; (b) $\xi_n' = 0.1, \alpha_{E_n} = 0.68$; (c) $\xi_n' = 0.5, \alpha_{E_n} = 0.68$; (d) $\xi_n' = 0.9, \alpha_{E_n} = 0.68$; (e) $\xi_n' = 1.4, \alpha_{E_n} = 0.68$; and (f) $\xi_n' = 1.9, \alpha_{E_n} = 0.68$. MD results are obtained on kerogen structure EFK 0.8 g/cm^3 (A = 4 Å, p = 25 Å).

of specular reflection, which would appear as a spike-like pattern in the velocity distributions of Fig. 4.7. This pattern is not discernible in these MD results, which indicates that any SK that in an ad hoc manner, proposes to incorporate a component of specular reflection will not be an exact predictor of the scattering behaviour on kerogen surfaces.

Fig. 4.8 shows the normal velocity distributions of reflected molecules. The incident velocity magnitudes of the normal component $|\xi_n'|$ are kept the same as the tangential velocity values. Fig. 4.8(a) shows the distributions for all the selected incident velocities. As ξ_n' increases, the peak of the distribution shifts to higher reflected velocities ξ_n and the curve flattens. As shown in Fig. 4.8(b), no SK is able to capture the reflection pattern of molecules with low incident velocity. This may be because the existence of the attractive force field, which decelerates the molecules in the direction normal to the surface and partially suppresses the reflection of molecules at small ξ_n. While the effects of this strong interaction cannot be fully predicted by a SK in the limit of small impinging velocities, the CL model seems to provide satisfactory comparisons from moderate to high incident velocities, as shown in Figs. 4.8(c-f).

To understand the interplay between normal and tangential velocity components that significantly influences the gas transport in porous media (Arya, Chang & Maginn, 2003a; Celestini & Mortessagne, 2008; Liang & Li, 2019), the scattering angular distributions of the reflected molecules are investigated next, as shown in Fig. 4.9. The representative incident angle θ_i are taken to be $15°, 30°, 45°, 60°$ and $75°$ with respect to the surface normal. The scattering angle

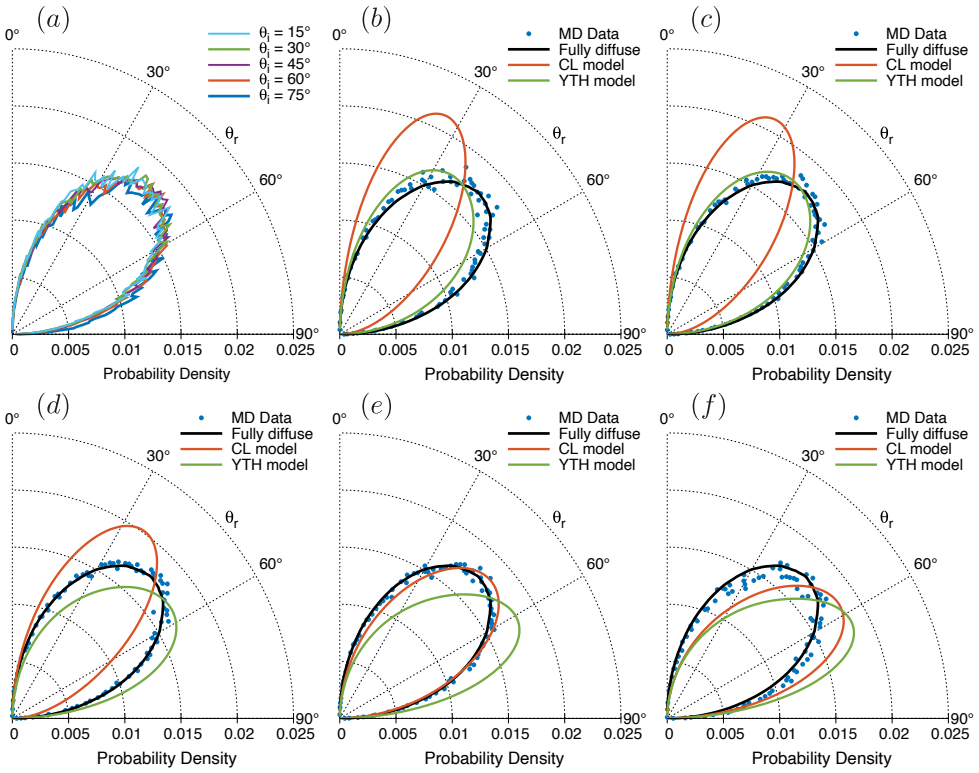

Figure 4.9: Comparison of reflected angular distributions predicted by (a) MD and (b-f) existing SKs $\theta_i = 15°, 30°, 45°, 60°, 75°$. MD results are obtained on kerogen structure EFK 0.8 g/cm^3 (A = 4 Å, p = 25 Å).

distributions can be calculated by the following equation:

$$\theta_r = \arctan\left(\frac{|\xi_n|}{|\xi_t|}\right). \tag{4.2}$$

The range of the scattering angle thus becomes $[0°, 90°]$. Unlike most beam experiments (Bruno et al., 2000; Saltsburg & Smith Jr, 1966; Yu, Zhang, Yang & Li, 2020), at which the scattering angle strongly depends on the incident angle of the gas molecule, Fig. 4.9(a) shows that distribution patterns due to different incident angles coincide with each other. The reason for this may be twofold: (a) the incident velocity in the presented simulations is relatively low, in contrast with beam experiments, where the impinging speed is normally high and leads to an increase in lobe peak height, and (b) the reflection pattern is considerably affected by the adsorption, micro- and mesoscopic roughness of the porous kerogen matrix, whereas most beam experiments consider a clean, smooth non-porous surface. Moreover, these angular scattering distributions based on the presented MD results are found to be very close to the fully diffuse SK, even though the ACs (i.e., α_t, α_{E_n}) are smaller than unity. Nevertheless, these

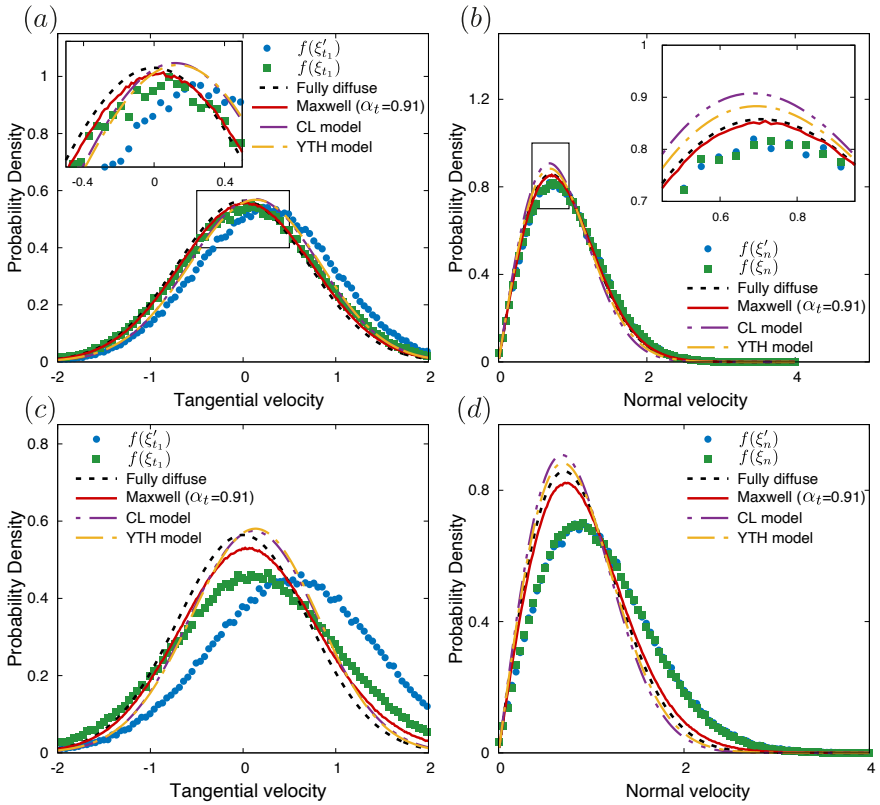

Figure 4.10: Overall velocity distributions from MD in Poiseuille flow, with bulk velocity and ACs for (a-b) the low speed case ($u_x^* = 0.25, \alpha_t = 0.91, \alpha_{E_n} = 0.68$), and (c-d) the high speed case ($u_x^* = 0.6, \alpha_t = 0.91, \alpha_{E_n} = 0.68$). MD results are obtained on kerogen structure EFK 0.8 g/cm^3 (A = 4 Å, p = 25 Å). Note that the general ACs (α_t, α_{E_n}) in this transport study are also interpreted as the equilibrium ones based on the kerogen structure, for which the corresponding values are shown in Fig. 4.5.

angular distribution measurements again confirm that the high degree of accommodation is one of the main characteristics during the scattering process of methane with kerogen. Under such a high degree of accommodation, all SKs that satisfy the basic relations (i.e., positiveness, normalisation and reciprocity) should get similar results and approach the fully diffuse SK.

4.4.4 Impact of Maxwell Model on Flow Transport

Although the presented results indicate that no single classical SK could capture the detailed scattering of methane with kerogen, a high degree of accommodation was observed during the GSIs in all the simulations. Additionally, it is more important to capture the reflected angular distribution, which reflects the interplay between different velocity components and can be modelled by the quasi-fully diffuse SK for rough surfaces, than independently capturing the distribution for each velocity component (Arya et al., 2003a; Celestini & Mortessagne, 2008; Liang & Li, 2019). It may also be more appropriate to adopt a fully diffuse model, which is simpler to implement for gas transport models. Here, the effect of the scattering physics

on gas transport is investigated, when there is a force-driven Poiseuille flow inside the set-up of Fig. 4.1(a). Two cases are initially considered with an external force $F_0 = 2.0 \times 10^{-14}$ N, 8.0×10^{-14} N applied on each fluid atom in the x-direction, leading to an average bulk velocity $u_x = 0.25, 0.60$, respectively. In Fig. 4.10(a), it is seen that the overall incident tangential velocity distribution follows a shifted diffuse scattering profile accommodated to a temperature higher than the kerogen surface, as a result of the external force. The overall reflected velocity distribution, however, lies in between the incident velocity distribution and the prediction from the fully diffuse SK (i.e., Maxwell model with TMAC = 1). To find the best fit of the reflected velocity distribution, the profiles predicted by the Maxwell, CL and YTH models are also drawn. It is observed that the simplest Maxwell model, with TMAC calibrated from the MD, turns out to reproduce a better overall fit than the other two kernels. This observation indicates that the Maxwell model may be sufficient in practical applications for gas transport near a kerogen surface, even though, as discussed, its detailed scattering pattern is not realistic due to the incorporation of a small specular reflection component. For the direction normal to the surface, Fig. 4.10(b) shows that incident and reflected velocity distributions are very close to each other. This overlap may be because the gas molecules are difficult to accommodate their normal kinetic energy with the surface in the first few collisions (see Section 4.4.2), especially under a bulk velocity. Moreover, although the CL model could provide satisfactory predictions for selected incident normal velocities without considering the gas transport (Fig. 4.8), the Maxwell model seems to give the closest agreement of the overall reflected velocity distribution for transport cases. It is noteworthy that the Maxwell model also gives good agreements for both tangential and normal components of the overall velocity distributions for nitrogen gas scattering on platinum walls (Yamamoto et al., 2006). As a comparison to the distributions of low-speed flows, Figs. 4.10(c,d) show large disagreements between the reflected velocity distributions and profiles of existing SKs for a high speed flow. This disagreement is expected from previous selected velocity distribution measurements. However, these high speed flows are rarely encountered in shale gas extraction and can safely be ignored, which is verified in the next part of this section.

Another perspective for investigating the effects of scattering physics on transport properties is by analysing velocity profiles across the pore, which are shown in Fig. 4.11 for a representative set of Knudsen numbers, i.e., $Kn = [0.12, 0.63, 6.25]$. These cases are selected to cover a significant range of gas rarefaction and specifically highlight the comparison between the MD flow transport simulations of methane through kerogen mesopores (as in Fig. 4.1(a)), and the equivalent MD simulations where the porous kerogen surfaces are now replaced by a scattering model instead. For these benchmark cases, the boundary condition is defined as a non-porous mathematical planar wall, and the Maxwell scattering model with TMAC calibrated from the presented scattering analysis. MD is chosen to compare both types of simulations, as it uses the same LJ potential for the gas–gas interactions. Furthermore, other distributions (CL, YTH) are not chosen because the previous analysis indicates that the simplest Maxwell model provides

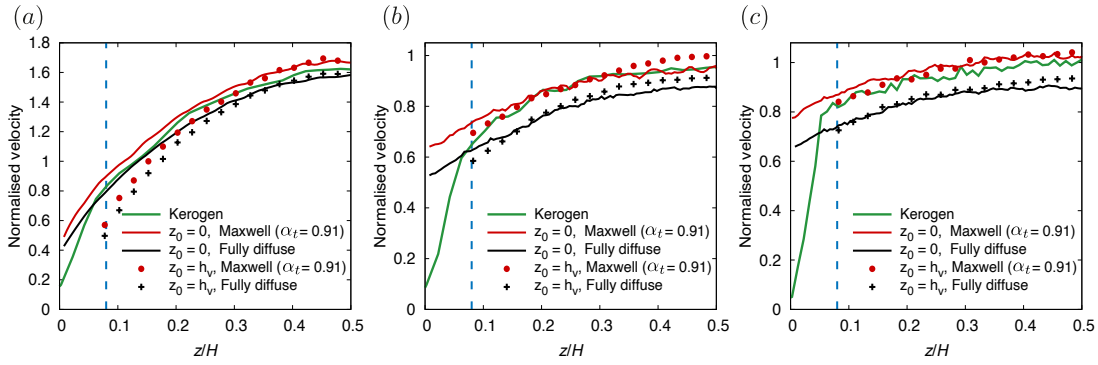

Figure 4.11: Profiles of normalised velocity for gas flow with Kn = (a) 0.12, (b) 0.63, and (c) 6.25. The vertical dashed line within each plot represents the virtual plane ($z_0 = h_v$). The solid lines represents the velocity profiles for a pore height of $H = 20$ nm (i.e., boundary located at $z_0 = 0$), while the scatter points represent the velocity profiles for a pore height of $H - 2h_v = 17$ nm (where the boundary is located at $z_0 = h_v$). To include the effect of pore size, a reference velocity V_0 is applied, which is assumed to be proportional to the normalised pressure gradient $\zeta = F_0 H/(k_B T_0)$ and the most probable speed ξ_m, i.e., $V_0 = \zeta \xi_m$. All the profiles are obtained from the flow on the kerogen structure EFK 0.8 g/cm^3 (A = 4 Å, p = 25 Å).

the best prediction of the overall reflected velocity distribution, which is sufficient for the transport study. An important remark needs to be made here. Mathematical boundaries that are used to model the gas-surface interaction should, in principle, be placed at the virtual plane, i.e., the location at which the scattering information was measured. However, this choice is not ideal, because shale rock surfaces (measured from experiments) will need to be translated by a distance h_v, which — depending on the pore size — may influence the permeability apart from making it complex to implement numerically. Having different pore heights also makes the comparison of transport in this study more challenging. Here, the velocity profile results are presented for both pore heights (H and $H - 2h_v$, which correspond to the location of the boundary at $z_0 = 0$ and $z_0 = h_v$, respectively) to test the SK, and discuss the implications of this shortly.

For flows with a moderately confined pore and a relatively high gas pressure (P_0 = 3.92 MPa), which correspond to $Kn = 0.12$ (Fig. 4.11(a)), it can be observed that all three types of surfaces produce a parabolic-like profile. In the bulk, both the Maxwell (TMAC = 0.91) and fully diffuse model give good agreements with the kerogen results for z_0 = 0, while the models implemented at $z_0 = h_v$ do not agree well. When the rarefaction level increases to Kn = 0.63 and 6.25, as shown in Fig. 4.11(b) and Fig. 4.11(c) respectively, the differences between boundary implementations ($z_0 = 0, z_0 = h_v$) becomes small in the bulk region of the flow. While the agreement between the kerogen surface and Maxwell model remains good, the deviation of the fully diffuse model from the kerogen surface becomes noticeable at large Kn.

In Fig. 4.11, the velocity profiles near the kerogen surface drop very rapidly within h_v to a finite but small slip value near the wall. This may be caused by the high adsorption force field, and it is expected the slip value will approach zero when a larger surface roughness (e.g., > 2 nm) is involved (Yu, Xu, Fan, Wang & Wu, 2020). From these figures, it is clear that none of the scattering models can predict the transport in this near-surface layer, which means the location of the boundary will always be marred by modelling inaccuracies within h_v. On one hand, if the boundary is located at $z_0 = h_v$ to correctly satisfy the condition of imposing scattering where it is measured, the mass transport due to geometrical differences for these moderately confined cases will be missed; for example, for $Kn = 0.63$, there is a 5-8% drop in mass transport. On the other hand, placing the boundary at $z_0 = 0$ allows some recovery of the local mass flow rate inside the near-surface layer, but the exact rate cannot be recovered because the local velocity and density profiles obtained by the scattering boundary model do not account for adsorption effects. At larger pore sizes, the difference about whether choosing $z_0 = h_v$ or $z_0 = 0$ does not matter, as $h_v/H \approx 0$ and the adsorption effects and flow rates in the near-surface layer become negligible on the overall transport. For the remaining part of the chapter, the location of $z_0 = 0$ is chosen, as it shows better overall agreement in the velocity profiles, has less effect on the mass flow rate for moderately-sized pores and is the most practical to implement in future kinetic solvers. Furthermore, the Maxwell model with TMAC calibrated from the MD is chosen, as the TMAC for the simulated kerogen surface with very small roughness is still less than unity.

Finally, the normalised mass flow rate Q^* is presented in Fig. 4.12, as a direct indicator of the impact of the SK on flow transport, across a wide range of Knudsen numbers. Comparisons are made between the MD simulations of the kerogen sample (EFK 0.8 g/cm^3, A = 4 Å, p = 25 Å), the calibrated Maxwell model of this sample (TMAC = 0.91) and the fully diffuse model (TMAC = 1) using MD simulations with simplified boundaries and the linearised Boltzmann equations (LBE) (Ohwada, Sone & Aoki, 1989). Because TMAC is not expected to change significantly with Kn, particularly for rough surfaces, it is fixed for all Knudsen numbers. In Fig. 4.12, the predictions given by the simplified MD simulations (LJ potentials + fully diffuse) agree well with the results predicted by LBE (hard-sphere molecules + fully diffuse) before the flow is highly rarefied, indicating the Boltzmann and its model equations are indeed applicable for mesospores with negligible confinement effect (e.g., $H \sim 20$ nm). Moreover, a general trend can be found that Q^*, given by the kerogen surface, lies between the predictions given by the Maxwell and the fully diffuse models, with a minimum value observed at $Kn \approx 1$. When Kn is small (i.e., within the slip and early transition flow regimes), the mass flow rate due to different surfaces are close to each other. This phenomenon is also confirmed in the work of Wu and Struchtrup (2017), where similar results are observed for various SKs at TMAC = 0.92 based on the LBE with the LJ potential of helium. Therefore, one may deduce that when the flow system is less-rarefied, an arbitrary SK (satisfying the basic properties) will provide adequate accuracy for the prediction of mass flow rate within shale, while the Maxwell model certainly is the simplest to implement numerically. As Kn increases to the free molecular regime, it is seen

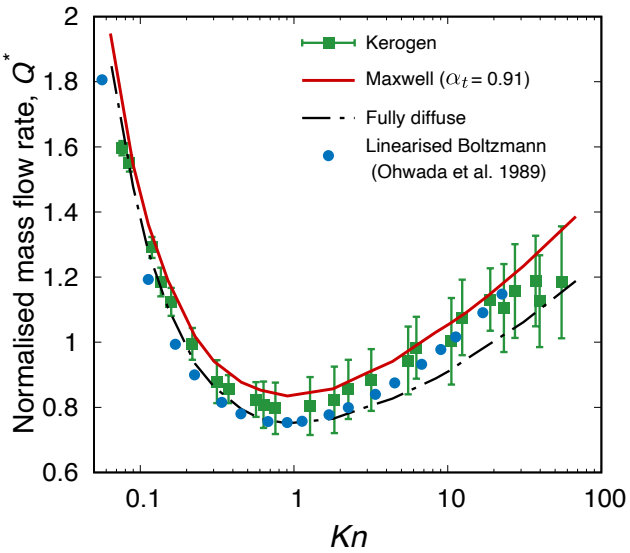

Figure 4.12: Dependence of the normalised mass flow rate on gas rarefaction Kn for kerogen structure EFK 0.8 g/cm^3 with a roughness amplitude A = 4 Å and period p = 25 Å. The mass flow rate Q was measured in the linear response regime (i.e., low-speed, isothermal flows) as the spatial integration of local density, area, and velocity, using discretised bins along the $z-$direction. The normalised mass flow rate therefore is defined as $Q^* = Q/Q_0$, where $Q_0 = mn_0V_0HL_y$ is the reference factor, and L_y is the depth of the simulation domain.

that the Maxwell model (TMAC = 0.91) agrees better with the mass flow rate from the kerogen surface, than the same model (implemented by MD and LBE) with TMAC = 1. It is worth noting that as the mesoscopic roughness increases from the assumed 0.4 nm to $\sim$ 2 nm, the TMAC will approach unity, at which the results of both kerogen surface and Maxwell model should converge to the prediction of the fully diffuse model. However, the flow rate predicted by both Maxwell and fully diffuse model have noticeable discrepancy from the kerogen surface results when the flow is highly rarefied ($Kn > 10$), which suggests that the dominant Knudsen diffusion mechanism (Arya et al., 2003a; Corral-Casas et al., 2021; Liang & Li, 2019) is now revealing the inaccuracies in the scattering dynamics of these models.

4.5 Conclusions

This chapter detailed the investigation of the scattering dynamics and accommodation of methane molecules on realistic kerogen surfaces, which contained porosities and mesoscopic roughness to enable the description of gas-surface interactions (GSIs). Existing scattering kernels (SKs) have been assessed by comparing the reflected velocity fluxes and evaluating their impact on the gas transport properties, using molecular dynamics (MD) simulations. The following key conclusions points are made:

- For re-emitted methane gas molecules, the residence time and displacement due to adsorption/desorption are on average unaffected by porosity; thus, GSIs on kerogen can be considered instantaneous in time and local in space, as assumed by conventional SKs.
- The most widely used SKs are found unable to describe the detailed scattering behaviours on kerogen surfaces, especially the reflected velocity fluxes of high-speed flows, and to a lesser extent, some of the lower speeds due to the kerogen's force field.
- The Maxwell model comes closest to the observed scattered angular beam pattern (under a TMAC = 1) and the overall reflected velocity distribution (under a TMAC calibrated by the presented MD results), which are both more important when considering the transport study, than correctly capturing the individual velocity component fluxes.
- The Maxwell model satisfactorily predicts the velocity profiles and overall mass flow rate for the transport cases confined between kerogen surfaces for a wide range of Knudsen numbers Kn, despite the observed deviation at large Kn, which, however, is a condition that is seldom met in shale reservoirs.

This chapter, therefore, confirmed the applicability of the diffuse-specular Maxwell model to deal with gas transport in organic shale media, even though the underlying scattering dynamics was found to be more sophisticated. Moreover, given the fact that the TMAC was observed to approach unity at atomic-scale roughness of $\Delta z \sim 2$ nm, as also reported on the study of other surfaces (Liang & Li, 2019; J. Sun & Li, 2011), the fully diffuse Maxwell SK may also be appropriate for modelling gas transport near kerogen or other mineral surfaces. This work also settles the question as to what value of TMAC should be used in gas transport near organic kerogen surfaces, and further investigations will be required when calibration studies with experiments reveal TMACs much lower than 1.0. For this to be true, there has to be a high concentration of very smooth non-organic surfaces, which is unlikely in shale rock.

Data availability

The data that support the findings of this study are openly available in Edinburgh DataShare repository at https://doi.org/10.7488/ds/3278.

Chapter 5

On the Impact of Surface Physisorption

N.B. This chapter has been published in: Chen, Y., Gibelli, L., Li, J., Borg, M.K. “Impact of surface physisorption on the gas scattering dynamics." *Journal of Fluid Mechanics* 968, A4 (2023)

Engineering flow systems operating under low pressures and/or at the micro/nano scale generally include a physically adsorbed gas layer next to the surface. In this chapter, a scattering kernel is developed that accounts for the effect of adsorption, arising from van der Waals interactions, on the dynamics of molecules impinging on solid smooth surfaces. In the limit of low bulk gas density, surface adsorption becomes negligible and the scattering kernel recovers consistently the Cercignani–Lampis model, which best describes molecular collisions with a clean, smooth surface. In the limit of high bulk gas density, a dense adsorbed molecular layer forms next to the surface and its presence is picked up by the Maxwell model with complete diffuse reflection, which better captures the multiple collisions of gas molecules. A weight coefficient based on the Langmuir adsorption isotherm is incorporated into the modelling to handle the transition between these two limiting conditions of low and high bulk gas densities. The proposed model is validated against high-fidelity molecular dynamics simulations that are performed for a variety of gas–surface combinations and adsorbed molecular layers with different densities. It is shown that the proposed model very well captures the scattering patterns of beams of gas molecules at different velocities impinging on surfaces, as well as momentum and energy accommodation coefficients in the entire range of explored conditions.

5.1 Literature Survey

When the condition of local quasi-thermodynamic equilibrium breaks down, dilute fluid flows are no longer governed by the Navier-Stokes equations with stick boundary conditions, and kinetic theory is required. The fluid behaviour must then be described by the Boltzmann equation, or a kinetic model equation, supplemented by boundary conditions that model the gas–surface interactions. These molecular interactions are typically formulated via the so-called scattering kernel (SK), which provides the probability density function of the molecules back-scattered into the gas after striking the surface. Typically, SKs contain a few parameters, referred to as accommodation coefficients (ACs), which describe how some physical properties of the impinging molecular flux (e.g. momentum and energy) accommodate to the state of the surface. SKs are of paramount importance in non-equilibrium gas dynamics simulations because they determine the velocity slip and temperature jump at the surface, which are the macroscopic hallmarks of the fluid non-equilibrium conditions, and, in turn, affect the overall flow field increasingly with the gas rarefaction.

The most famous and extensively used SK was proposed by Maxwell (1879). The Maxwell model assumes that a fraction of incident gas molecules are diffusely reflected, while others are re-emitted specularly. Despite being widely used, the Maxwell model is unable to reproduce the lobular re-emission patterns that are experimentally observed when a nearly monoenergetic atomic beam hits the surface (Cercignani & Lampis, 1971). Much effort has been employed over the years towards developing more accurate SKs that incorporate the gas–surface interactions.

Epstein (1967) extended the Maxwell model by replacing the constant accommodation coefficient with a function of the molecular velocity to reflect the dependency of the scattering dynamics on the velocity of the incident particle. Furthermore, Klinc and Kuščer (1972) considered the particular case of diffuse-elastic scattering, where molecules are isotropically back-scattered into the gas but conserve their impinging speed. A more general SK is the Cercignani–Lampis (CL) model (Cercignani, 1972; Cercignani & Lampis, 1971) that was derived by solving the half-space transport equation describing the dynamics of gas atoms within the wall modelled as a homogeneous and non-polar medium. It is worth stressing that the CL model was also obtained by using different approaches (Cowling, 1974; Kuščer et al., 1971; Takata et al., 2021; Williams, 1971) and was proved to be the most general mathematical expression consistent with the basic properties that all SKs are expected to fulfil (see Section 2.2.3 for more details of these basic kernel properties).

SKs have also been proposed that linearly combine the models above. Struchtrup (2013) combined the Maxwell model with the diffuse-elastic SK. The resulting model provides results similar to the CL model but has a simpler mathematical expression that makes it easier to derive boundary conditions for extended moment equations. In the Yamamoto-Takeuchi-Hyakutake (YTH) model (Yamamoto et al., 2007), it is assumed that a fraction of scattered molecules

follow a CL-like model, while the remaining molecules are diffusely reflected. This model provides scattering patterns in better agreement with molecular dynamics (MD) simulations when the surface is contaminated with a fixed amount of heavy molecules while bombarded with lighter gas. However, the YTH model does not contain links with the contaminant information nor the adsorption physics. It is a phenomenological model where the AC functions are fitted from specific simulations conditions and are thus not general. The combination of Epstein and CL models was also proposed, and it was shown that it more accurately captures the trajectory of molecules in the scattering process (Yakunchikov et al., 2012), while providing an accurate description of both the Poiseuille and thermal transpiration flows (Wu & Struchtrup, 2017).

Despite the many studies devoted to gas–surface interactions, relatively little attention has been paid to the development of SKs that incorporate adsorption (Aoki & Giovangigli, 2019, 2021; Aoki et al., 2022; Borman et al., 1988; Brancher et al., 2020; Kuščer, 1978). Yet, experimental, theoretical, and numerical evidence clearly indicates that neglecting the presence of adsorbed molecules oversimplifies the scattering dynamics and introduces inaccuracies in the resulting prediction of fluid flow. This was first highlighted in a pioneering experimental study, where it was shown that ACs of gases in contact with single-crystal silicon approach unity as pressure increases (Arkilic et al., 2001). Thereafter, this has been attributed to adsorption, as ACs have been found to significantly increase if the surface gets adsorbed with gas molecules, reaching unity when a fully adsorbed layer is formed (Chew, 2009; Finger, Kapat & Bhattacharya, 2007; Nejad, Nedea, Frijns & Smeulders, 2020; Sazhin, Borisov & Sharipov, 2001; Yamamoto et al., 2006).

A better understanding of how adsorption affects the scattering dynamics is not only of theoretical interest, but also has relevant practical implications. Examples range from a more accurate prediction of aerodynamic drag forces on satellites operating on very low Earth orbits, where these forces are strongly dependent on the variation of the atomic-oxygen adsorption with altitude (Livadiotti et al., 2020; Pilinski, Argrow, Palo & Bowman, 2013), to the enhancement of the manufacturing throughput of microprocessor chips in low vacuum photolithography machines, where adsorption of contaminants is detrimental (G. Chen, 2005). More generally, adsorption is expected to significantly affect the transport of nanoscale confined fluid flows (Shan, Wang, Wang, Zhang & Guo, 2022), such as hydrocarbons inside tight shale reservoirs (R. Wang et al., 2021), and the heat transfer efficiency in micro-electro-mechanical systems (MEMS) due to the large surface-area-to-volume ratios characterising these problems (B. Cao et al., 2009).

This chapter aims to derive a new SK that captures the effect of adsorption, arising from van der Waals interactions only (also known in the literature as physisorption) on the scattering dynamics, and unravel the resulting bulk fluid density-dependence on the ACs. The proposed kernel is the linear combination of the CL model for a clean, smooth surface and the fully

diffuse Maxwell model for a surface covered by a dense gas layer, with the weight of the combination proportional to the Langmuir adsorption isotherm (Langmuir, 1916). The proposed kernel is validated using high-fidelity MD simulations with Lennard-Jones (LJ) potentials that accurately resolve the trajectories of molecules interacting with each other in the adsorbed layer and with the surface.

It is important to emphasise that the presented study takes a different approach to model the physics of adsorption than most past research. In particular, while the proposed SK is intended to capture the overall effects of adsorption, previous studies have attempted to derive models from first principles. For example, Borman et al. (1988) proposed a kinetic equation to study the dynamics of gas molecules in a potential field generated by surface atoms, with molecule–phonon collisions accounting for fluctuations, and this approach has recently been extended to include adsorption and chemical reactions on crystal surfaces (Aoki & Giovangigli, 2019, 2021; Aoki et al., 2022). Despite its ability to precisely capture the intricate physics of adsorption, this kinetic equation-based modelling is computationally demanding and not suitable for engineering simulations. On the other hand, the proposed modelling approach has similarities with the pioneering work of Kuščer (1978) and more recently of Brancher et al. (2020). However, the focus of this work is primarily on the case of a steady adsorbed gas layer adjacent to the walls, whereas these two references mainly explore non-equilibrium adsorption-desorption phenomena. A more in-depth comparative analysis of these studies is presented in Section 5.2.

The remaining structure of this chapter is as follows. The new SK, which encompasses the effect of adsorption, is derived in Section 5.2. The set-up of high-fidelity MD simulations used in this work is presented in Section 5.3. In Section 5.4, an extensive validation study is carried out to evaluate the scattering patterns and the ACs as functions of the gas bulk density. Finally, concluding remarks are given in Section 5.5.

5.2 A New Scattering Model, Incorporating Adsorption

A new scattering model is presented that incorporates the effect of gas adsorption on smooth surfaces. Note the SK proposed here is applicable to standard temperatures or higher, so that quantum effects (Bird, 1994; Goodman & Wachman, 1976) do not play a role and the classical scattering description is applicable. For simplicity, the effect of wall roughness is omitted from this work.

Molecules impinging on smooth solid surfaces may be divided into two groups. The first group comprises adsorbed molecules, namely molecules that are momentarily trapped and go through multiple collisions with the surface and/or other fluid molecules before moving away, and as a result, are more likely to accommodate thermally with the surface (Arya, Chang & Maginn,

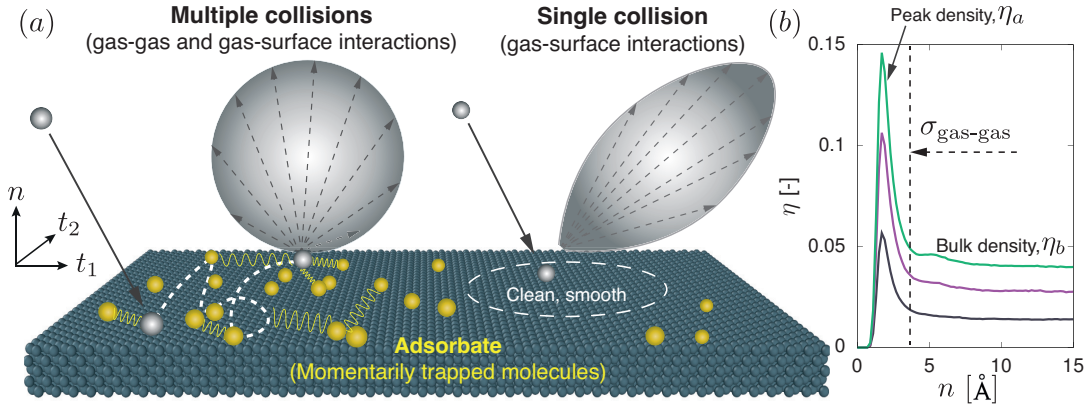

Figure 5.1: (a) Schematic of scattering dynamics of gas molecules near a smooth surface. During the scattering process, incident gas molecules (grey) could either suffer single or multiple collisions (both with the wall and other momentarily adsorbed gas molecules). (b) Example density profiles in the presence of argon (Ar) molecules near the platinum (Pt) surface at an equilibrium temperature of 300 K, with distinguishable features of bulk and elevated adsorption densities.

2003b; Bird, 1994; Butt et al., 2003; B. Cao, Chen & Guo, 2005; Kuščer, 1978; Myong, 2004; C. T. Rettner, Schweizer & Mullins, 1989). The second group is composed of molecules that, after hitting the clean part of the surface (i.e., where no adsorption occurs locally), are immediately reflected back to the bulk of the gas, and their behaviour is only expected to depend on the local microscopic features of the surface. The scattering dynamics of these two groups are very different, as depicted in the schematic of Fig. 5.1(a), and the rate of these contributions depends on the bulk density. In the limit of high gas bulk density, the first scattering group dominates, while the second scattering group is seen more in the limit of low gas bulk density.

The proposed SK is therefore a linear combination of these two limiting scattering contributions, namely the fully diffuse Maxwell model, $\mathscr{R}_{\mathrm{d}}$, which properly captures the effect of multiple collisions with adsorbed molecules (often seen in the limit of high density), and the CL model, $\mathscr{R}_{\mathrm{CL}}$, which is deemed to provide the most accurate description of the interactions of molecules with a clean, smooth surface (often seen in the limit of low density):

$$\mathscr{R}_{\mathrm{new},t} = \theta_1(\eta_b)\mathscr{R}_{\mathrm{d},t} + [1-\theta_1(\eta_b)]\mathscr{R}_{\mathrm{CL},t}(\alpha_{t,0}), \tag{5.1a}$$

$$\mathscr{R}_{\mathrm{new},n} = \theta_2(\eta_b)\mathscr{R}_{\mathrm{d},n} + [1-\theta_2(\eta_b)]\mathscr{R}_{\mathrm{CL},n}(\alpha_{E_n,0}), \tag{5.1b}$$

where $\alpha_{t,0}$ and $\alpha_{E_n,0}$ are the TMAC and NEAC of a smooth surface being free of adsorption, and are called the intrinsic coefficients. In principle, these coefficients can be obtained either from beam experiments performed in low vacuum systems (Goodman & Wachman, 1976), or using approximate theoretical models (Goodman, 1974). It is worth stressing that, from the derivation of the CL model, the details of a collision between a gas molecule and a solid atom (i.e.,

hard collisions) are assumed to be negligible, compared to the effect of simultaneously grazing collisions (Cercignani, 1988). Therefore, the accuracy of the CL model may decrease when a corrugation effect exists from the crystal structure, as would be the case in the MD simulations, which may contain a subtle corrugation in the gas–surface potential energy landscape.

In Eq. (5.1), the function θ_1 represents the probability that a molecule striking the surface behaves as an adsorbed molecule in the tangential component, and it is anticipated to be an increasing function of the reduced bulk number density $\eta_b = n_{bulk}\pi\sigma^3_{\text{gas-gas}}/6$, where n_{bulk} is the bulk number density, $\sigma_{\text{gas-gas}}$ is the diameter of a gas molecule; the function θ_2 has a similar meaning, although for the normal component, but must be treated separately because the tangential component is known to exhibit a faster accommodation rate to the state of the surface than the normal one (Cercignani, 1988; Y. Chen et al., 2022).

The function θ_1 can be naturally related to the gas/surface coverage, defined as the ratio between the occupied sites and the maximum binding sites available on the surface. Indeed, the denser is the adsorbed gas layer next to the surface (i.e., the higher the peak density η_a shown in Fig. 5.1(b)), the higher becomes the probability that the gas molecule accommodates to the state of the surface. The surface coverage can be predicted based on the classical Langmuir adsorption isotherm (Langmuir, 1916) when a monolayer adsorption forms adjacent to the surface (see sample density profiles in Fig. 5.1(b)). As for the function θ_2, the simplest direct proportionality relation is presumed also to exist with the surface coverage. Accordingly, in dimensionless units, the combination coefficients read:

$$\theta_1 = \frac{\hat{K}_L\eta_b}{1+\hat{K}_L\eta_b}, \qquad \theta_2 = C\frac{\hat{K}_L\eta_b}{1+\hat{K}_L\eta_b}, \tag{5.2}$$

where $C \in [0,1]$ is a fitting constant, and $\hat{K}_L$ is the Langmuir constant. It is worth stressing that the Langmuir adsorption isotherm has already been used by Goodman (1974) and Pilinski et al. (2013) for assessing the effect of adsorption on the energy and thermal accommodation coefficients, and it is chosen here for its simplicity. However, in principle, more sophisticated isotherm models can also be used, such as the Freundlich model (Freundlich, 1922) for heterogeneous surfaces and the Brunauer-Emmett-Teller (BET) model for multilayer adsorption (Brunauer, Emmett & Teller, 1938).

Note that, according to Eq. (5.1), the TMAC and NEAC of the new SK read:

$$\alpha_t = \theta_1 + (1-\theta_1)\,\alpha_{t,0}, \tag{5.3a}$$

$$\alpha_{E_n} = \theta_2 + (1-\theta_2)\,\alpha_{E_n,0}. \tag{5.3b}$$

As expected, the ACs recover their intrinsic values for clean, smooth surfaces, i.e., $\alpha_t \to \alpha_{t,0}$, $\alpha_{E_n} \to \alpha_{E_n,0}$ in the limit when θ_1 and θ_2 go to zero.

It is worth noting that Brancher et al. (2020) have proposed a SK with many similarities to the proposed model, namely a linear combination of Maxwell fully diffuse and CL (or Maxwell with incomplete accommodation). Unlike the proposed model, which focuses solely on the effect of an adsorbed gas layer in dynamic equilibrium, Brancher's model can explain the time variation of the adsorbed surface coverage, which simplifies to the Langmuir isotherm when the adsorption and desorption rates are in balance. However, the assumptions on the scattering dynamics underlying Brancher's model differ from the proposed model, as can be clearly seen by considering the two limiting cases of clean and fully adsorbed surfaces. In particular, in the case of clean surfaces, the proposed SK simplifies to CL, while that of Brancher et al. (2020) remains a linear combination of Maxwell fully diffuse and CL, where the coefficient of the combination is the adsorption probability. In the case of fully adsorbed surfaces, the proposed SK simplifies to Maxwell fully diffuse, while that of Brancher et al. (2020) simplifies to the CL model. As discussed in detail in the next section, the modelling choices in this study allow the obtainment of scattering patterns that are in overall good agreement with those predicted by MD.

5.3 Modelling the Scattering Using MD

In the MD simulations carried out in this work, surface atoms are constructed in a Face-Centred Cubic (FCC) arrangement with a lattice parameter 3.92 Å, as shown in Fig. 5.1(a), and gas molecules are modelled as monatomic for simplicity. It is worth stressing that very heavy gas molecules with high intermolecular attraction, such as xenon, was not considered, as they could 'permanently' stick to the surface, which violates the assumption of negligible residence time. To extend the validation of scattering models from moderately heavy to light gas molecules, and keep the gas-surface interaction unreactive, two distinct groups of gas-surface combinations have been considered: argon-platinum (Ar-Pt) and helium-gold (He-Au), respectively. Each combination has been investigated under various reduced bulk gas densities η_b, thereby permitting one to consider adsorption of different degrees. The velocity-Verlet algorithm is implemented for the trajectory integration with a time step of 1 fs, and interactions among atoms are described by the standard 12-6 Lennard-Jones (LJ) potential. The interactions parameters for Ar-Pt and He-Au, which are obtained from Spijker et al. (2010) and Liao, Grenier, To, de Lara-Castells and Leonard (2018), respectively, are listed in Table 5.1 with a LJ cut-off distance $r = r_c = 15$ Å.

Each MD simulation run is divided into two steps: equilibration and production. During equilibration, both gas molecules and wall atoms are kept at a constant temperature, using the Nosé–Hoover thermostat, with a time constant of 100 fs in the NVT ensemble. Here, two temperatures are considered: 300 K, typical for room temperature of MEMS/NEMS devices, and 423 K, which was considered in the earlier scattering study in Chapter 4, and is used here

Argon-Platinum			Helium-Gold		
Atom pairs	σ[Å]	ε/k[K]	Atom pairs	σ[Å]	ε/k[K]
Ar-Ar	3.405	119.80	He-He	2.64	10.890
Pt-Pt	2.471	8053.6	Au-Au	2.630	2662.1
Ar-Pt	2.940	79.139	He-Au	4.342	9.1355

Table 5.1: Interatomic Lennard-Jones potential parameters (σ, ε) used in the MD simulations. Molecular masses m [u]: Ar = 39.948; He = 4.0026; Pt = 195.084; Au = 196.967.

to test the proposed scattering model under elevated temperature conditions. Each parallel wall has an outer edge of rigid wall molecules, which prevents any movement of the wall. Following equilibration, the thermostat on the gas molecules is switched off such that their scattering dynamics are not biased. The production run provides access to all Lagrangian information from which the scattering data of interest can be calculated. As before, the scattering results are recorded by placing an artificial virtual plane at a distance r_c away from, and parallel to the surface, within which a gas molecule and a wall atom can still feel each other. When a molecule from the bulk crosses the virtual plane, its incident information (e.g., $\boldsymbol{\xi}', \boldsymbol{r} - \boldsymbol{\epsilon}, t - \tau$) is recorded. The reflected information of the same molecule will be recorded again (e.g., $\boldsymbol{\xi}, \boldsymbol{r}, t$) when it crosses the plane back into the bulk, as illustrated in Fig. 5.2(a) (inset). Furthermore, the collisions of gas molecules within the near wall region can be tracked. To accurately describe the scattering behaviour and construct the scattering function $\mathscr{R}(\boldsymbol{\xi}' \rightarrow \boldsymbol{\xi})$, collisions $O(10^6)$ are generally required, which leads to $O(10^{-9})$ seconds of a production run, depending on the dimension and density of the system.

5.4 Results and Validation

In this section, the accuracy of the assumptions underpinning the proposed model is assessed first (Section 5.4.1). Afterwards, the parameters of the proposed SK are calibrated to best fit the MD results for TMAC and NEAC in the range of gas bulk densities explored in this work (Section 5.4.2). Finally, the proposed SK is shown to well describe the interplay between momentum and energy accommodation coefficients (Section 5.4.3), and more accurately predicts the scattering patterns of monoenergetic beams (Section 5.4.3) provided by the MD simulations for different gas bulk densities and gas–surface systems.

5.4.1 Assessment of Model Assumptions

The proposed SK relies on three key modelling assumptions. First, a higher density of adsorbed gas layer results in a higher fraction of molecules suffering multiple collisions (assumption 1). Second, molecules that undergo multiple collisions are more likely to accommodate to the state of the surface, where the rate of accommodation of the normal component is slower than the tangential one (assumption 2). Third, the fraction of molecules that are completely accommodated to the state of the surface can be identified with the surface coverage as given by the Langmuir isotherm (assumption 3). In the following, these assumptions will be assessed for the Ar-Pt system at a temperature of 423 K. However, similar qualitative trends were found for all systems carried out in this work, which are not reported here for brevity.

Assumptions 1 and 2 are examined in Fig. 5.2(a), which shows the probability histogram of the individual gas collisions that occur between the virtual plane and the wall; a collision occurs when a molecule's velocity component changes sign, which captures both gas-gas and gas-surface collisions. It is apparent that when the surface is clean ($\eta_a = \eta_b = 0$), a gas molecule has the highest probability of colliding only once, whereas the probability of multiple collisions increases with the density of the gas layer, as indicated by the larger tail of the histogram for larger η_b. Furthermore, Figs. 5.2(b,c) support assumption 2 by showing that molecules accommodate more strongly to the state of the surface if they collide multiple times (i.e., the ACs approach unity with higher number of collisions, where here the ACs refer to beams composed of molecules grouped based on the number of collisions), and the accommodation rate is faster for TMAC than for NEAC. It is worth noticing that TMAC shows a zig-zag-like behaviour. From a qualitative standpoint, this phenomenon can be explained using the illustration in Fig. 5.2(d) of some sample collisions: the number of changes in the tangential velocity component, denoted by N_t, occur more frequently on even collisions (e.g. $N = 2, 4, ...$) and this increases the rate of accommodation, leading to the higher TMACs observed in Fig. 5.2(b). The same argument explains why the behaviour of the NEAC is instead almost monotonic.

Assumption 3 is examined in Figs. 5.2(e,f). Molecules were first grouped in two categories depending on whether they collided twice (solid green symbols) or more than twice (solid black symbols) with the surface, and the TMAC of each group is computed as a function of the reduced bulk density. As shown in Fig. 5.2(e), the TMACs of the two groups follow trends that qualitatively match those of the solid lines that represent the two contributions featuring in the proposed SK, i.e., θ_1 and $(1-\theta_1)\alpha_{t,0}$, respectively (these contributions were computed using the model calibrated as discussed in Section 5.4.2). In Fig. 5.2(f), a similar comparison is presented for NEAC. However, the criterion used here to define the two groups is slightly different; namely, a higher collision threshold was considered (four collisions instead of two) to account for the expected lower accommodation rate of the normal velocity component compared to the tangential one. A good qualitative agreement is seen in this case as well.

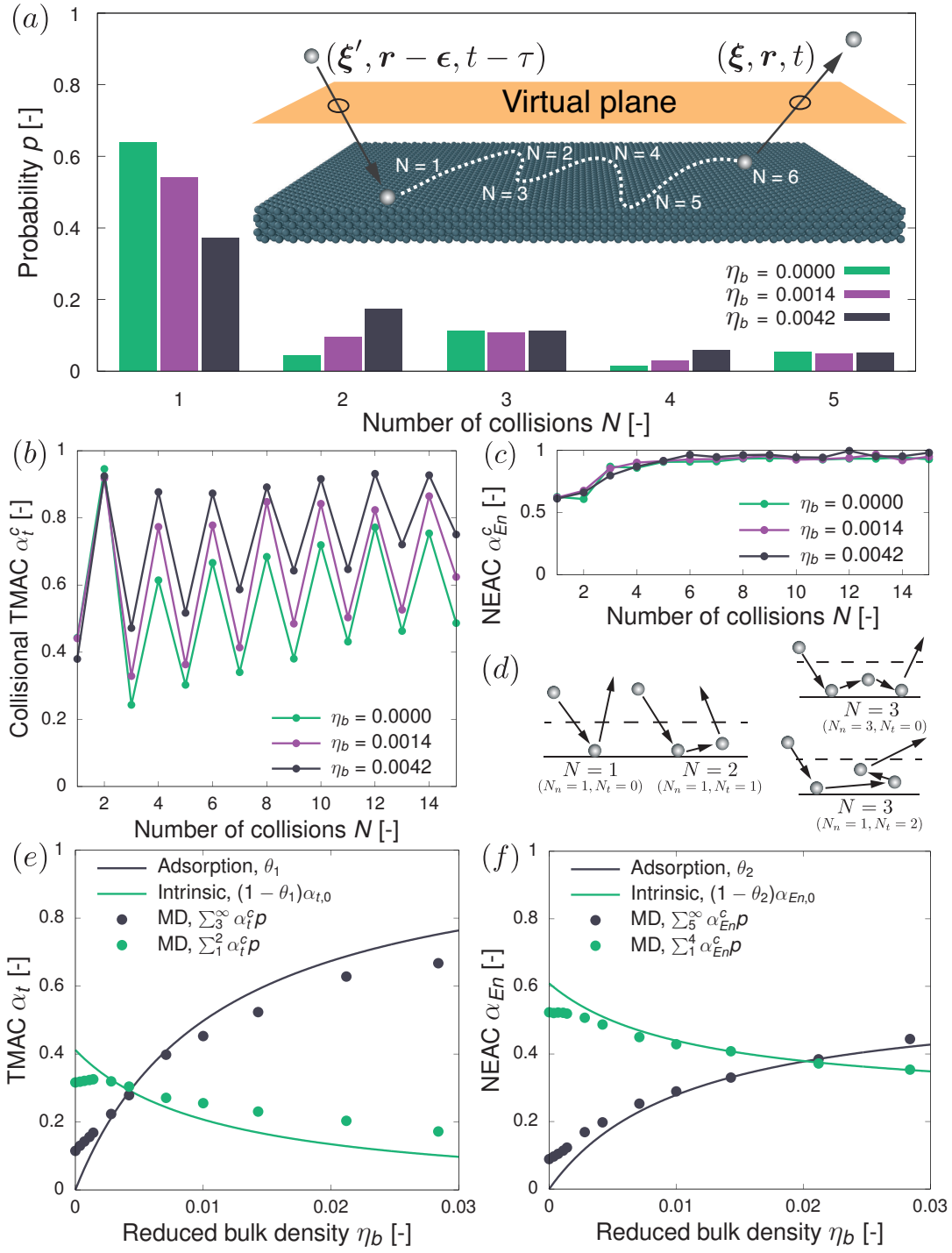

Figure 5.2: Scattering process of argon molecules on a platinum surface at 423 K. (a) Probability histogram of the number of collisions, with the inset indicating the tracking of the scattering process. (b) TMAC versus number of collisions. (c) NEAC versus number of collisions. (d) Qualitative schematics of odd versus even collisions. Contributions to (e) TMAC and (f) NEAC of molecules suffering two, for TMAC, and up to four, for NEAC, collisions (green colour) and multiple collisions (black colour) as functions of the reduced bulk density. Solid symbols are MD results and solid lines are the predictions of the proposed and calibrated SK, Eq. (5.3).

5.4.2 Model Calibration

	$\alpha_{t,0}$		$\alpha_{E_n,0}$		$\hat{K}_L$		C	
	300 K	423 K	300 K	423 K	300 K	423 K	300 K	423 K
Ar-Pt	0.49	0.41	0.64	0.61	125.15	95.34	0.58	0.57
He-Au	0.07	0.11	0.14	0.18	102.59	90.36	0.69	0.73

Table 5.2: Reference values for the intrinsic accommodation coefficients ($\alpha_{t,0}, \alpha_{E_n,0}$) and the calibrated constants ($\hat{K}_L, C$).

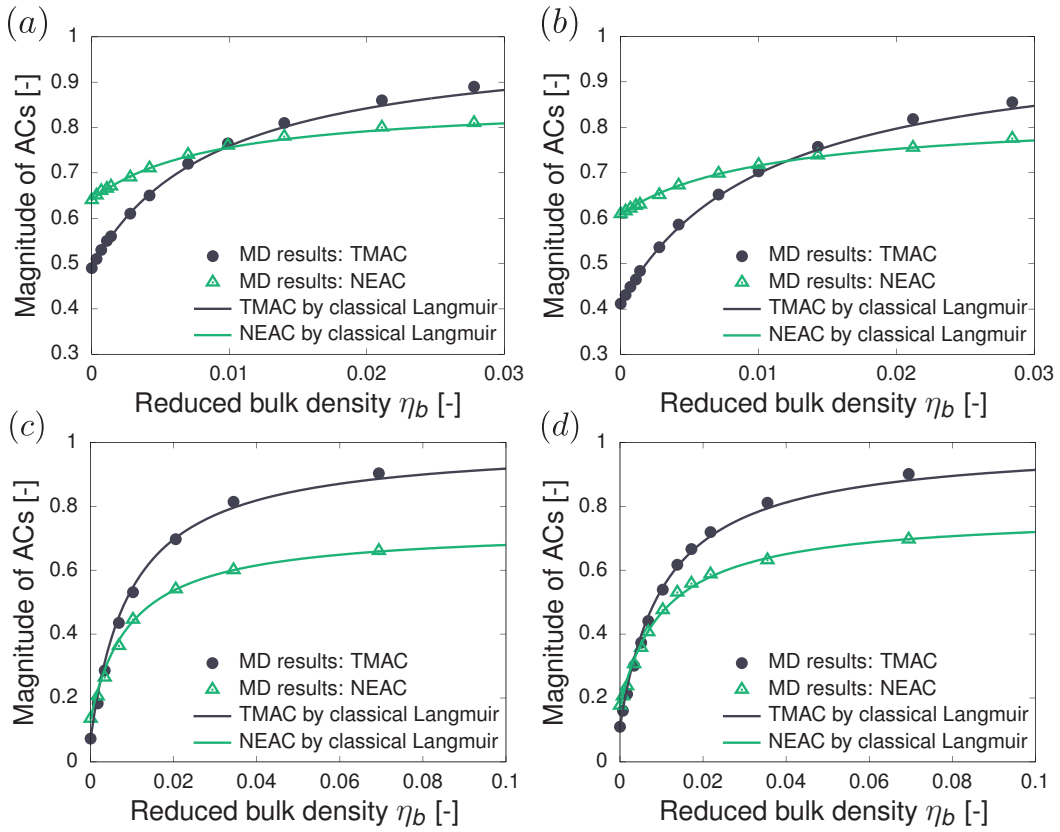

Figure 5.3: Variation of the general accommodation coefficients with bulk densities η_b given by MD results for the Ar-Pt system at (a) 300 K and (b) 423 K; the He-Au system at (c) 300 K and (d) 423 K.

The proposed SK features two groups of parameters, namely $(\alpha_{t,0}, \alpha_{E_n,0})$, which describe the re-emission dynamics from a clean, smooth surface, and $(\hat{K}_L, C)$, which account for the effects of the adsorbed gas layer. The first group of parameters was evaluated by computing TMAC and NEAC based on MD simulations in which gas-gas interactions are switched off. Afterwards, the second group of parameters were calibrated by fitting Eq. (5.3), alongside Eq. (5.2), to the values of TMAC and NEAC corresponding to different reduced bulk densities provided by MD simulations, which include gas-gas interactions. Here, the two groups of parameters, obtained from the considered systems, are listed in Table 5.2 for reference. The AC results measured

Model	Intrinsic correlations
Maxwell	$\alpha_{E_t} = \alpha_t$
Cercignani–Lampis	$\alpha_{E_t} = \alpha_t(2-\alpha_t)$
YTH	$\alpha_{E_t} = 1-(1-\alpha_t)^{3/2}$
Proposed model Eq. (5.1)	$\alpha_{E_t} = \alpha_{t,0}(1-\alpha_t)+\alpha_t$

Table 5.3: Relation between the TMAC (α_t) and the TEAC (α_{Et}) for various SKs.

from the MD are shown in Fig. 5.3 for the sample cases of Ar-Pt and He-Au systems at two different temperatures (solid symbols), along with the fitting curves (solid lines). An excellent agreement is found except for the larger values of the reduced bulk density, e.g., at $T = 300$ K, deviations are less than 4% for the Ar-Pt system, and reduce to 2% for the He-Au system. These deviations can be explained by the inability of the Langmuir isotherm to capture the interactions between adsorbed gas molecules that arise when a high-density gas layer covers the surface. However, by including the effect of repulsive lateral interactions on the adsorption and desorption rates (Butt et al., 2003), all MD data were able to be fitted with an accuracy of 3%.

Two remarks are worth making about the results reported in Eq. (5.3). First, the slope of NEAC is smaller than that of TMAC regardless of the temperature and gas-solid combination. This clearly highlights the slower accommodation of the energy to the state of the surface and, therefore, the need to introduce the constant C in Eq. (5.2). Second, the general ACs take smaller values as the temperature increases for the Ar-Pt system, while the opposite has been observed for the He-Au system.

5.4.3 Assessment of Scattering Dynamics

Correlation between accommodation coefficients

The fundamental aspects of gas-surface interactions are fully encompassed in the SK, but ACs are also useful in that they provide some coarse-grained information about the dynamics of molecules impinging on the surface. As the SKs represented by Eq. (2.28) only contain one disposable parameter in the tangential component and another one in the normal component, relations must exist between ACs of quantities defined along the same directions. The relations between TMACs and tangential kinetic energy accommodation coefficients (TEACs) of the SKs considered in this study are listed in Table 5.3, whereas those between normal momentum accommodation coefficients (NMACs) and NEACs were determined numerically because the presence of the Bessel function prevents one to easily obtain results in closed form. Note that the relations between TMACs and TEACs do not depend on the impingement distribution but this is not the case for the relations between NMACs and NEACs. The results presented in this section refer to a Maxwellian impingement that typically occurs when considering low-speed gas flows.

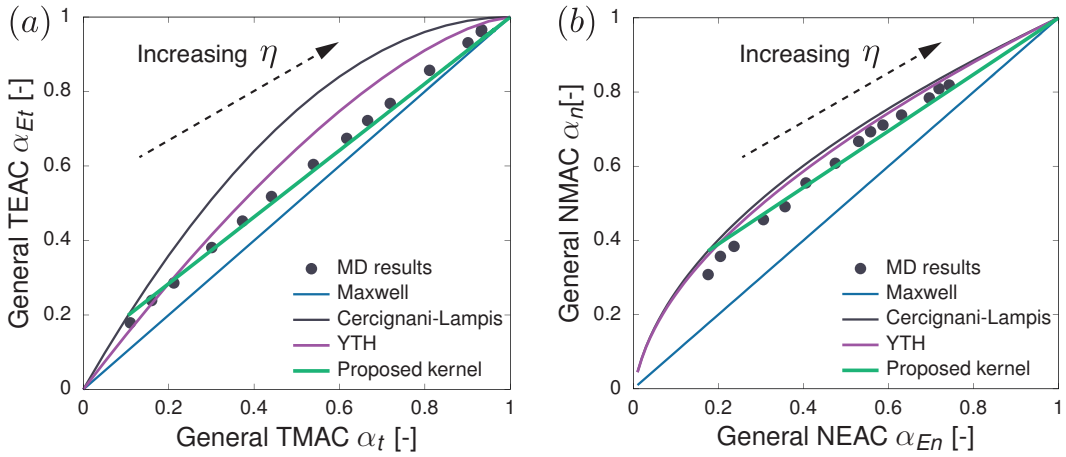

Figure 5.4: Relation between momentum and energy accommodation coefficients for the He-Au system at 423 K, given by the MD results and predicted by various SKs. (a) TEAC versus TMAC; (b) NMAC versus NEAC. Density of data points correspond to those in Fig. 5.3(d).

Fig. 5.4 shows the relations between TMAC and TEAC (panel (a)) and between NMAC and NEAC (panel (b)) provided by MD simulations for various reduced densities (solid symbols), along with the predictions of the SKs (solid lines). It is apparent that the proposed SK provides the best match with MD results in the range of explored reduced densities. The predictions of the Maxwell model are in poor agreement with MD results, especially for the smaller values of η_b.

The CL model agrees reasonably well with the MD results in this limit, whereas large discrepancies of the CL model can be clearly seen in Fig. 5.4(a) when the surface adsorption increases. The YTH model shows an agreement at intermediate densities. Note here that the same phenomenological fit is carried out for the YTH model with the MD simulations, using the general ACs.

Scattering patterns

A more accurate assessment of the SKs is here carried out by comparing the scattering patterns of monoenergetic beams provided by each model against MD simulation results. In these numerical experiments, a monoenergetic beam is obtained by selecting only those molecules bombarding the surface which have their tangential (normal) component of velocity in the range $[\xi', \xi' + \Delta\xi']$, and re-emission probabilities of the velocity components are evaluated accordingly.

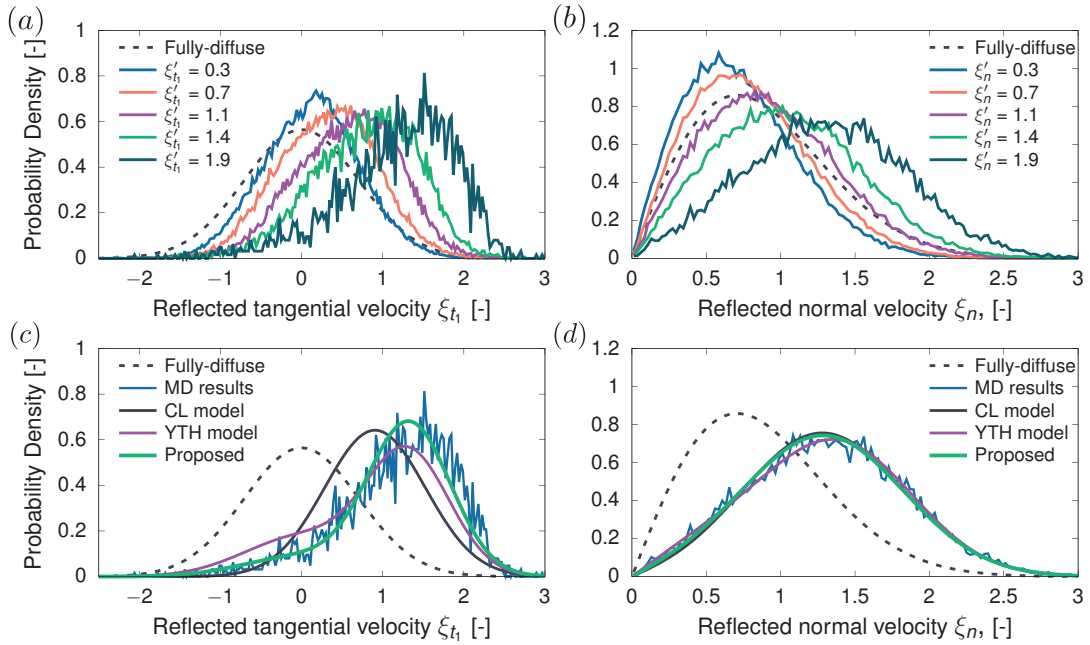

Figure 5.5: Re-emission probability distributions of the (a) tangential and (b) normal velocity for monoenergetic beams predicted by MD for Ar-Pt system with surface temperature 423 K and $\eta_b = 0.0011$. Velocities of the beams are normalised by the most probable speed $\sqrt{2RT}$. In (c)-(d) MD results are compared against predictions of the SKs for an example of high impinging velocity of $\xi'_{t_1} = 1.9$ and $\xi'_n = 1.9$.

Figs. 5.5(a-b) show the reflected velocity distributions of argon molecules scattered from a platinum surface at 423 K. An example value of the reduced bulk density is presented here, i.e., $\eta_b = 0.0011$, to highlight the different predictions of the SKs, since in the limiting cases of small and large reduced densities, similar behaviours are anticipated (e.g., in the limit when η_b goes to zero, the proposed SK simplifies to the CL model). As expected, the re-emission patterns are centred around the line of specular reflection with large tails at small velocities.

Figs. 5.5(c-d) show the comparison between the scattering patterns of a monoenergetic beam predicted by the different SKs, under a high incident velocity ($\xi'_{t_1} = 1.9, \xi'_n = 1.9$), which is chosen specifically to reveal high deviations from Maxwell's model. It is apparent that the tail of the re-emission pattern in the tangential direction is very well captured by the proposed SK, while deviations can be clearly seen from the predictions of CL and YTH models. As for the normal direction, all the SKs provide satisfactory fits to MD data showing that the adsorbate does not affect significantly the scattering dynamics in this direction.

Fig. 5.6 shows results similar as in Fig. 5.5 but for the He-Au system. Compared to the case of argon molecules scattered by a platinum surface, the smaller degree of accommodation to the state of the surface makes the tangential distributions narrower near the specular-reflected velocity and the tails of the normal distributions thinner. In Fig. 5.6(c), a small discrepancy is found between the proposed model and the MD result. This is not unexpected since the fine

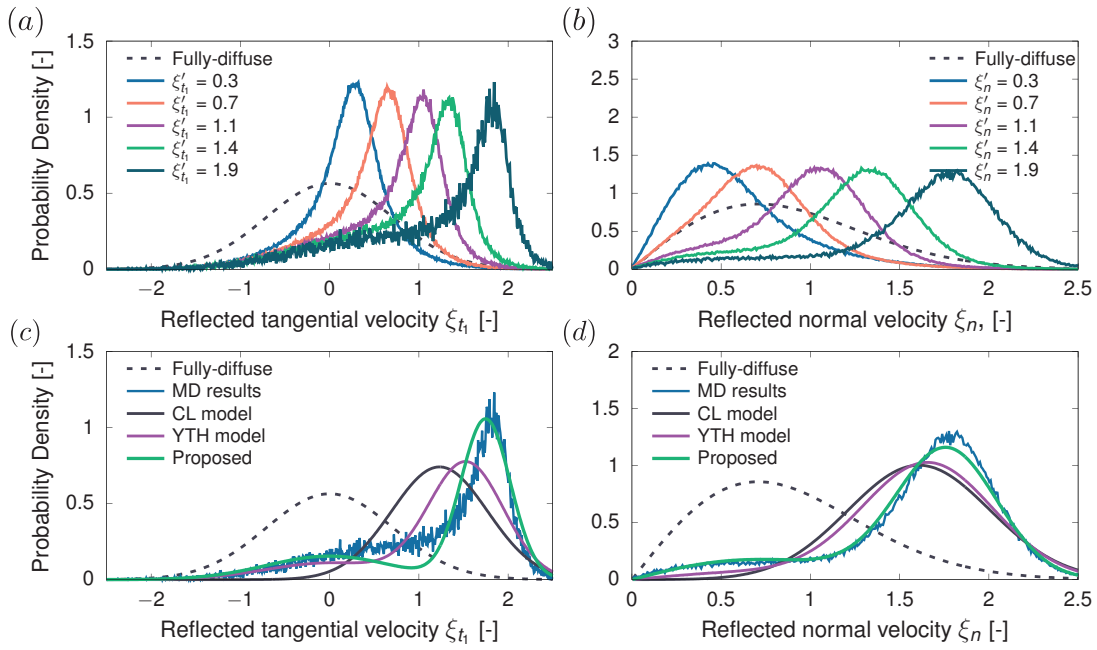

Figure 5.6: Re-emission probability distributions of the (a) tangential and (b) normal velocity for monoenergetic beams predicted by MD for He-Au system with surface temperature 423 K and $\eta_b = 0.0051$. Velocities of the beams are normalised by the most probable speed $\sqrt{2RT}$. In (c)-(d) MD results are compared against predictions of the SKs for an example case of high impinging velocity of $\xi'_{t_1} = 1.9$ and $\xi'_n = 1.9$.

details of the real scattering patterns depend on many additional features such as residence time, sticking probability and desorption rate, to name a few. Nevertheless, it should be emphasised that, despite its simplicity, the proposed model gives an overall good agreement with the scattering patterns, as shown in Figs. 5.6(c-d), confirming its applicability even for gas-surface interactions with intrinsically small momentum and energy accommodations (see Table 5.2).

A more quantitative comparison of the scattering patterns of monoenergetic beams was performed by computing the L^2-norm errors assuming the MD results as baseline for comparison:

$$\varepsilon_{t_1}(\xi'_{t_1}, \eta_b) = ||\mathscr{R}_{\mathrm{SK}}(\xi'_{t_1} \to \xi_{t_1}; \eta_b) - \mathscr{R}_{\mathrm{MD}}(\xi'_{t_1} \to \xi_{t_1}; \eta_b)||_2, \tag{5.4a}$$

$$\varepsilon_n(\xi'_n, \eta_b) = ||\mathscr{R}_{\mathrm{SK}}(\xi'_n \to \xi_n; \eta_b) - \mathscr{R}_{\mathrm{MD}}(\xi'_n \to \xi_n; \eta_b)||_2, \tag{5.4b}$$

where

$$||g||_2 = \left[\int_{-\infty}^{\infty} g^2 d\xi\right]^{1/2}. \tag{5.4c}$$

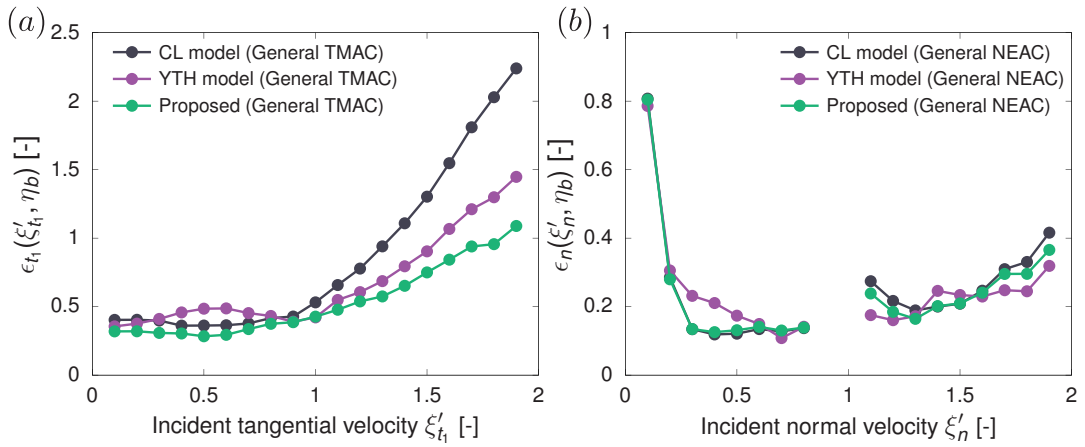

Figure 5.7: Beam L^2-norm errors between the reflected velocity distributions of monoenergetic beams predicted by existing SKs and MD results versus the impinging molecule velocity. The results refer to the Ar-Pt system at the surface temperature of 423 K and $\eta_b = 0.0011$ in the (a) tangential, and (b) normal directions.

Fig. 5.7 shows the L^2-norm of the errors of CL, YTH, and the proposed SK for the Ar-Pt system at 423 K with $\eta_b = 0.0011$, and impinging velocities in the range of $[0,2]$. Note that the results related to the normal component near the most probable speed have been removed as the mathematical definition of ACs is very sensitive to numerical errors in that region (see Section 2.2.2). Interestingly, for small velocities, the errors related to the tangential component are almost constant, whereas the ones related to the normal component are large. This is likely to be attributed to the attractive force field exerted by the surface that is accounted for by none of the SKs. Nevertheless, the proposed SK outperforms others in accuracy for both tangential and normal scattering patterns.

In order to check the accuracy of all SKs over a larger span of reduced densities, the error given by Eq. (5.4) was integrated with respect to the impinging velocity using the Maxwellian flux as a weight, and the results was normalised using the error of the Maxwell fully diffuse model:

$$\varepsilon_{t_1}(\eta_b) = \frac{\int \varepsilon_{t_1}(\xi'_{t_1}, \eta_b)\, f_w(\xi'_{t_1}) d\xi'_{t_1}}{\int ||\mathscr{R}_{\mathrm{d}}(\xi_{t_1}) - \mathscr{R}_{\mathrm{MD}}(\xi'_{t_1} \to \xi_{t_1})||_2\, f_w(\xi'_{t_1}) d\xi'_{t_1}}, \tag{5.5a}$$

$$\varepsilon_n(\eta_b) = \frac{\int_{\xi'_n<0} \varepsilon_n(\xi'_n, \eta_b)\, f_w(\xi'_n) |\xi'_n| d\xi'_n}{\int_{\xi'_n<0} ||\mathscr{R}_{\mathrm{d}}(\xi_n) - \mathscr{R}_{\mathrm{MD}}(\xi'_n \to \xi_n)||_2\, f_w(\xi'_n) |\xi'_n| d\xi'_n}. \tag{5.5b}$$

The error given by Eq. (5.5) is computed for the range of reduced densities considered in this study, and the results are reported in Figs. 5.8(a,b) for the tangential and normal directions, respectively. The proposed SK turns out to be the most accurate. In particular, it shows a similar accuracy as the CL model for clean, smooth surfaces (small η_b), whereas it is closer to the YTH model as the degree of adsorption increases (large η_b). Note that, as already pointed out, the

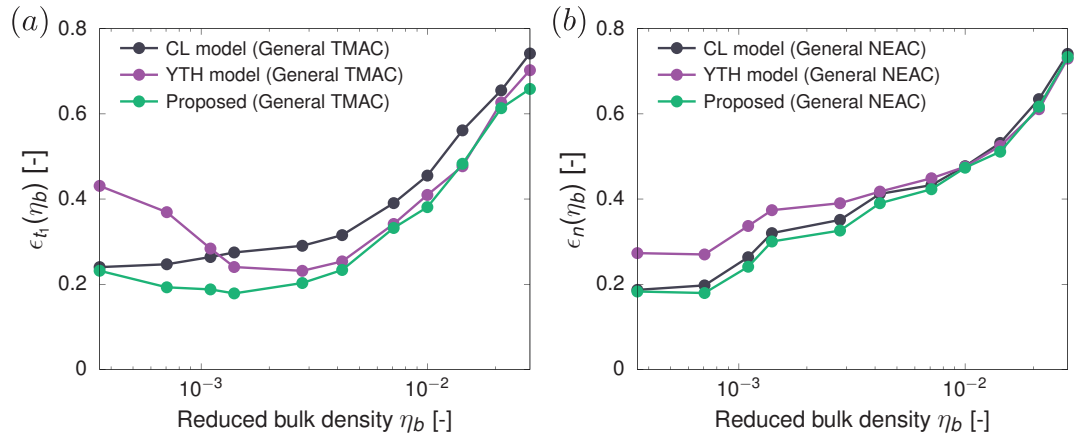

Figure 5.8: General L^2-norm errors, obtained by integrating the corresponding beam errors and using the Maxwellian flux as weighted factor, versus the reduced density. The results refer to the Ar-Pt system at the surface temperature of 423 K in the (a) tangential, and (b) normal directions.

adsorbate has a comparatively minor impact on the normal component of the scattering patterns and this is clearly reflected by the smaller discrepancies between scattering models shown in Fig. 5.8(b). Finally, the proposed model is expected to have better overall accuracy over existing SKs when considering the He-Au system, where the intrinsic ACs are smaller (and the impact of adsorption is found to be more significant) compared to the Ar-Pt system.

5.5 Conclusions

Existing scattering kernels (SKs) assume that gas molecules impinging on a surface only interact with wall atoms, whereas this assumption is inaccurate when an adsorbed layer forms next to a surface. In such a condition, gas–gas interactions affect the molecular scattering process, as clearly shown by the dependence of the accommodation coefficients (ACs) on the gas bulk density. To address this limitation, a new SK is proposed as a simple linear combination of the Cercignani–Lampis (CL) and Maxwell fully diffuse models, using the Langmuir isotherm as a weighting factor. The rationale behind this modelling approach is that the CL term accurately describes the scattering process from a clean, smooth surface, whereas the Maxwell fully diffuse term is expected to capture also the effect of multiple gas–gas interactions when an adsorbed gas layer forms next to the surface. The accuracy of various SKs were assessed using high-fidelity molecular dynamics (MD) simulations, and it was shown that the proposed SK gives the best performance across the range of explored bulk densities.

Future work will consider the implementation of the proposed scattering model in kinetic solvers and to test its performance in heat and flow simulations where adsorption is present. Notably, preliminary studies reveal that a conventional SK alone may not be sufficient to describe these heat and flow cases at the nanoscale, and this will need to be tackled in future work. The possible extension of the proposed model to polyatomic molecules is also of interest. Although there are expressions of the Maxwell fully diffuse and CL models for this case (Dadzie & Méolans, 2004; Gorji & Jenny, 2014; Lord, 1991, 1995) and encouraging results in the literature suggesting that a linear combination may work (Wu & Struchtrup, 2017; Yamamoto et al., 2007), a more detailed study using MD is needed to determine whether the coupling between internal and translational energy modes adds complexity and thereby requiring a more sophisticated modelling approach.

Data availability

The LAMMPS and post processing source codes that support the findings of this study are openly available in the Edinburgh DataShare repository at http://doi.org/10.7488/ds/7473.

Chapter 6

On the Impact of Random Nanoscale Roughness

N.B. This chapter has been published in: Chen, Y., Gibelli, L., Li, J., Borg, M.K. "Impact of random nanoscale roughness on gas-scattering dynamics" *Physical Review E*, 109(6), p.065308.

The impact of nanoscale wall roughness on rarefied gas transport is widely acknowledged, yet the associated scattering dynamics largely remain elusive. In this chapter, a scattering kernel is developed for surfaces having nanoscale roughness that distinctly characterises the two major types of interactions between gas molecules and rough surfaces. Namely, these are: (a) the weak perturbations arising from the thermal motion of wall atoms, essentially gas–phonon collisions, which are captured by the well-established Cercignani–Lampis model, and (b) the hard collisions owing to the irregularities of the rough, static potential energy surface, which are generally described by the fully diffuse model. Drawing an analogy between wave–surface and gas–surface scattering, a pseudo Debye–Waller factor is incorporated into the modelling as a weighting coefficient to allow the transition between smooth and rough surface conditions. The proposed scattering kernel is validated through high-fidelity molecular dynamics simulations that are performed for systems with varying roughness, temperature, and gas–surface combinations. The results indicate that the model well captures the scattering dynamics of gas molecular beams impinging on surfaces at different velocities, specifically for the accommodation coefficients and reflection patterns. Additionally, in flow and heat transport cases, it accurately predicts macroscopic quantities such as velocity slip and temperature jumps across the range of tested conditions.

6.1 Literature Survey

Engineering fluid systems operating at low pressures or micro/nanoscales often indicate the breakdown of local quasi-thermodynamic equilibrium, necessitating a different modelling approach that goes beyond standard continuum fluid dynamics. In these problems, the fluid behaviour must then be modelled using the Boltzmann or a kinetic model equation, supplemented by boundary conditions that model gas–surface interactions (GSIs). As gas rarefaction increases, gas molecules increasingly collide with wall atoms, making GSIs critical in simulating non-equilibrium gas dynamics. These interactions, which are molecular in nature, determine the velocity slip and temperature jump at the surface, which are macroscopic manifestations of fluid non-equilibrium conditions and significantly influence the overall flow field.

GSIs are conventionally formulated through scattering kernels (SKs) (Brancher et al., 2020; Cercignani, 1972, 1988; Cercignani & Lampis, 1971; Y. Chen, Gibelli, Li & Borg, 2023; Deng et al., 2022; Epstein, 1967; Kuščer et al., 1971; Lord, 1991; Maxwell, 1879; Struchtrup, 2013; Wu & Struchtrup, 2017; Yamamoto et al., 2007), establishing a probabilistic connection between incident and reflected molecular flux at the surface. These SKs generally include adjustable parameters known as accommodation coefficients (ACs) (Cercignani, 1988; Kuščer, 1974), which describe how physical properties of the impinging molecular flux (e.g. momentum and energy) are accommodated to the state of the surface. Physically-grounded representations of GSIs have also been considered, either by simplifying them to consider only binary collisions between gas molecules and effective surface cubes (Goodman & Wachman, 1976; Liang et al., 2018; Logan & Keck, 1968; Tully, 1990), or more comprehensively, by solving kinetic equations within a very thin layer near the surface, modelling the behaviour of gas molecules subjected to a static potential field from fixed wall atoms and colliding with phonons representing the fluctuating surface potential (Aoki et al., 2011; Aoki & Giovangigli, 2019, 2021; Aoki et al., 2022; Borman et al., 1988; Brull et al., 2014, 2016; Frezzotti & Gibelli, 2008; Krylov, 2003).

While substantial efforts have been invested in providing more accurate descriptions of GSIs, the role of nanoscale surface roughness has been notably underrepresented (Brull et al., 2016). Conventional SKs tend to model surface roughness by simply tweaking ACs, without relating them to the detailed scattering dynamics. Although pioneering experimental studies (D. Blanchard & Ligrani, 2007; Seidl & Steinheil, 1974; Stacy, 1923; Thomas & Lord, 1974; Trott, Castañeda, Torczynski, Gallis & Rader, 2011) and subsequent numerical research (Arya et al., 2003b; Y. Chen et al., 2022; Ozhgibesov, Leu, Cheng & Utkin, 2013) demonstrate variations in the ACs of gases on rough surfaces compared to their smooth (polished) counterparts, the relationship between ACs and roughness is not always fully understood, as discussed in a recent work (Perrier, Hadj-Nacer, Méolans & Graur, 2019). Furthermore, ACs alone are inadequate to capture the effects of roughness on gas scattering

dynamics. This can be seen from numerical studies using the same ACs in various SKs, but producing different macroscopic properties (Basdanis, Tatsios & Valougeorgis, 2022; Sharipov, 2002; Wu & Struchtrup, 2017), and experiments where ACs are extracted based on pre-assumed SKs (Sharipov & Moldover, 2016; Yamaguchi et al., 2011). Therefore, the relationship between ACs and surface roughness needs to be more deeply investigated, and surface roughness should be embedded in the modelling of SKs to pick up the overall reflection patterns.

There have been endeavours to understand the role of roughness on rarefied gas transport, but the emphasis has been predominantly on larger scale structures (i.e. meso or microscale) (Su, Liu, Zhang & Wu, 2017; C. Zhang, Chen, Deng & Shi, 2012). When examining gas scattering dynamics, investigations should also consider nanoscale irregularities (Brull et al., 2016), which are brought by the height variation of wall atoms on the scale of a few nanometres. Current studies at the nanoscale (Arya et al., 2003b; Brull et al., 2016; B.-Y. Cao, Chen & Guo, 2006; Y. Chen et al., 2022; Sofos, Karakasidis & Liakopoulos, 2009; H. Sun & Faghri, 2003) have favoured simple geometrical constructions, such as surfaces with sinusoidal and triangular roughness, which typically have led to qualitative rather than quantitative analyses, thus limiting their wider applicability.

In the present chapter, a SK is proposed that quantitatively characterises the influence of nanoscale roughness on the scattering dynamics. The proposed kernel is a linear combination of the Cercignani–Lampis (CL) model (Cercignani & Lampis, 1971) for a smooth, thermal wall and the fully diffuse Maxwell model (Maxwell, 1879) for a highly rough surface. The weighting coefficient of these two limiting conditions is found to be a form of the Debye–Waller factor (DWF), which can be obtained experimentally and provides additional insights into the effects of surface roughness on the ACs. To assess the proposed SK, high-fidelity molecular dynamics (MD) simulations are performed for gas molecules interacting with various rough surfaces. The scattering reflection patterns are then measured accurately based on the deterministic gas molecular trajectories.

The remaining chapter is organised as follows: Section 6.2 provides a background of the spectral characterisation of random roughness. Building on an established analogy between wave–surface scattering and GSIs, a new SK is proposed in Section 6.3. Section 6.4 details the setup of the high-fidelity MD simulations with the implementation of random roughness that are carried out for both scattering and heat/flow measurements. Section 6.5 validates the scattering dynamics predicted by the proposed SK on surfaces with different roughness characteristics, demonstrates its accuracy on Fourier and Poiseuille flow in large nanochannels and shows how it provides better agreement than current ones with the benchmark MD simulations. Finally, concluding remarks are given in Section 6.6.

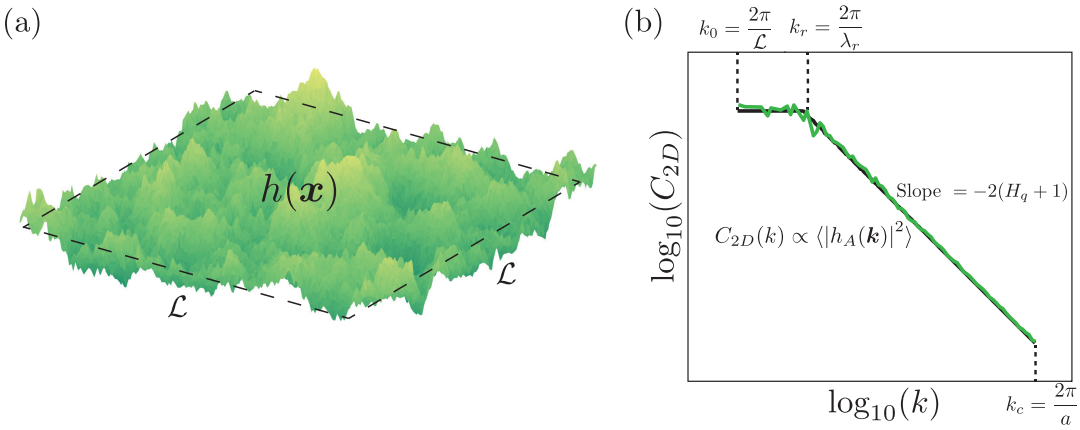

Figure 6.1: (a) An example of a surface profile $h(\boldsymbol{x})$ with random roughness on a square plane. (b) A typical surface roughness power spectrum associated with the height profile $h(\boldsymbol{x})$, possessing a mean of zero and characterised, on average, by a second moment as defined by the height spectrum. The green line indicates the exact power spectrum taken from the sample in (a). Further details regarding the notations, e.g., Hurst exponent H_q, roll-off wavelength λ_r and wavevector k_r, are common in the literature, such as in Persson et al. (2004).

6.2 Spectral Characterisation of Random Rough Surfaces

The fully diffuse and CL models cover the extremes of very rough and smooth (thermal) surfaces (Cercignani, 1988; Goodman & Wachman, 1976), respectively. However, few SKs systematically study roughness at the nanoscale, which lies between these two extremes. To develop a SK model that manages this intermediary range of roughness, the foundational methodology for characterising surface roughness is presented first in this section.

Surface roughness is quantitatively described by its height, denoted as $h(\boldsymbol{x})$, with respect to position $\boldsymbol{x}$. The variation in height is captured by the correlation function $C(\boldsymbol{x}_2 - \boldsymbol{x}_1)$ evaluated between two separated points. Employing a Fourier transform on this function and invoking the convolution theorem enables surface roughness analysis within the spatial frequency domain, characterised by wavevectors $\boldsymbol{k}$. This approach yields the surface power spectrum $C(\boldsymbol{k})$, also referred to as the power spectral density, which statistically describes the roughness by revealing the amplitude of height variations and the distribution of spatial frequencies $\boldsymbol{k}$ — the inverse of the wavelength. Surfaces exhibiting large height variations over short length scales thus will show elevated spatial frequencies in their power spectra compared to smoother surfaces, making the power spectrum a useful tool to characterise surface roughness over diverse length scales.

If the surface statistical properties are isotropic and translationally invariant, the dependency of the spectrum on the wavevector reduces to the magnitude, i.e., $C(\boldsymbol{k}) = C(k)$. For simplicity, while satisfying general validity, the consideration is restricted to a square area $A = \mathscr{L}^2$, as shown in Fig. 6.1(a). A two-dimensional spectrum $C_{2D}(k)$ thus can be expressed as (Persson et

al., 2004):

$$C_{2D}(k) = \frac{(2\pi)^2}{A}\langle|\hat{h}_A(\boldsymbol{k})|^2\rangle, \tag{6.1}$$

where the angle brackets stem from the spatial autocorrelation of height functions and stands for ensemble averaging, while

$$\hat{h}_A(\boldsymbol{k}) = \frac{1}{(2\pi)^2}\int_A \mathrm{d}^2x\, h(\boldsymbol{x})e^{-i\boldsymbol{k}\cdot\boldsymbol{x}} \tag{6.2}$$

is the Fourier transform of the zero-mean height profile $h(\boldsymbol{x})$, measured over the sample of area A. Note that, as shown in Fig. 6.1(b), there will be an upper and a lower limit to the wavevector within the spectrum. The largest feasible wavevector will be of order $2\pi/a$, where a embodies a short wavelength cut-off associated with the lattice constant. Conversely, the smallest feasible wavevector is of order $2\pi/\mathscr{L}$, with $\mathscr{L}$ being the length dimension of the surface. To generate a random rough surface, the power spectral density (PSD) is first specified, defining how each spatial frequency contributes to the overall roughness. A grid of wave vectors is then created, corresponding to discrete spatial frequencies within the spectrum limits. For each wave vector, a Fourier component is assigned by setting its amplitude according to the PSD—often using a power-law decay $C(k) \propto k^{-2(H_q+1)}$, where H_q is the Hurst exponent controlling the fractal characteristics—and assigning a random phase to ensure randomness while maintaining statistical properties. The zero frequency amplitude is set to zero, representing the average surface height. The PSD is scaled to match the specified root-mean-square (RMS) roughness, ensuring both the correct spectral distribution and amplitude of roughness. To obtain a real-valued surface profile, conjugate symmetry is applied to the Fourier components, preventing imaginary values in the spatial domain. Finally, an inverse Fourier transform is performed to combine all frequency components and generate the surface height profile as a two-dimensional array. The detailed algorithm for this process is provided in Appendix B. Finally, it is worth stressing that the typical power spectrum shown in Fig. 6.1(b) can be observed in the fluidic channel fabrication of microchips, where the roughness of silicon wafer surfaces is found to be random and multiscale (Bora et al., 2005; Gui, Elwenspoek, Tas & Gardeniers, 1999; Persson et al., 2004; Székely & Guttman, 2005).

6.3 GSIs Inspired by the Debye–Waller Factor (DWF)

The investigation of GSIs could gain profound insights from the analogy with established wave–surface scattering (Bass & Fuks, 2013), as exemplified in a study involving the scattering of electromagnetic waves by a randomly rough surface (Williams, 1971).

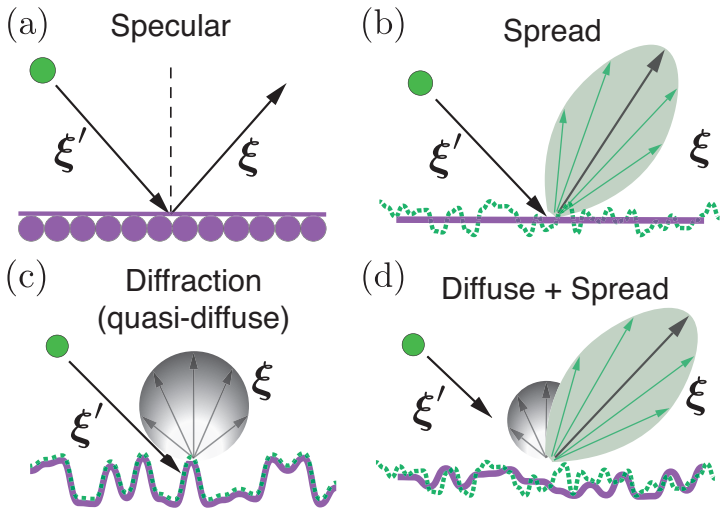

Figure 6.2: Schematic illustrating gas molecule scattering patterns: (a) elastic specular reflection on a perfectly smooth rigid/frozen surface; (b) inelastic spread reflection on a perfectly smooth surface but which contains thermal motion; (c) diffraction-induced reflection on a rough surface; (d) representative inelastic reflection factoring in both surface roughness and thermal motion on surfaces of interest in this work (i.e. containing nanoscale roughness).

In the wave–surface scattering scenario, it is known that the wavevector of an incoming wave is altered by the thermal motion of the wall atoms as well as their nanostructure morphology, e.g., surface roughness. Indeed, experimentally recording both the incoming and outgoing wavevectors of X-rays or neutrons serves as a useful method to elucidate the properties of the surface.

For the scenario of GSIs, the aforementioned analogy can be applied to a group of gas particles impinging the surface, whose incoming wavevectors get an imprint of the surface wavevectors upon their reflection (Beeby, 1971, 1972; Goodman, 1977; Manson & Miret-Artés, 2022). To be precise, a 'gas wavevector' $\boldsymbol{k}_g = 2\pi/\lambda = m\boldsymbol{\xi}/\hbar$ is defined via the de Broglie wavelength λ, and $\hbar$ is the reduced Planck constant. The term 'surface wavevectors' is used from here onward as an effective representation of wavevectors in the power spectrum $C_{2D}(k)$, stemming from the height profile after the Fourier transform (see Section 6.2).

6.3.1 DWF for Thermal Motion

When a beam of gas particles scatters from rigid surfaces comprised of frozen atoms, the scattering is purely elastic, i.e., it does not involve energy transfer with the wall atoms. All scattered particles are found in perfectly sharp (delta function) peaks (Barker & Auerbach, 1984; Billing, 2000) — either a specular reflection on the perfectly smooth surface, such as that shown schematically in Fig. 6.2(a), or diffracted beams arising from the corrugated surface. The thermal motion of solid atoms attenuates this elastic scattering by a Debye–Waller factor (DWF) (Krivoglaz, 1967), and leads to the spread of the scattered particles, as shown in

Fig. 6.2(b). The DWF is defined as (Barker & Auerbach, 1984; Billing, 2000; Goodman & Wachman, 1976; Manson & Miret-Artés, 2022):

$$\mathrm{DWF} = \exp(-\langle(\boldsymbol{u}_\ell \cdot \Delta\boldsymbol{k}_g)^2\rangle), \tag{6.3}$$

where $\boldsymbol{u}_\ell$ is the displacement of the wall atom from its equilibrium position due to its thermal motion, $\Delta\boldsymbol{k}_g$ is the change of wavevector after scattering, and angle brackets denote the thermal averaging at a given temperature (Barker & Auerbach, 1984; Goodman & Wachman, 1976).

The DWF, alongside its complement, 1−DWF, hence provides approximate fractions of elastic and inelastic scattering events, respectively. Furthermore, the DWF exhibits temperature dependence, indicated as $\ln(\mathrm{DWF}) \propto -T_w$ (Barker & Auerbach, 1984; Glauber, 1955; Manson & Miret-Artés, 2022). Consequently, it is not unexpected that in GSIs, the form of DWF noticeably coheres with the effects of wall temperature T_w on the ACs, characterised by an exponentially decaying relationship (B. Cao et al., 2005; Menzel & Kouptsidis, 1974). While the DWF has been shown to qualitatively describe the scattering physics related to thermal motion, it has not been explicitly used in the modelling of a SK.

6.3.2 Pseudo Debye–Waller Factor (PDWF) for Rough Surfaces

In this study, a DWF-inspired concept has been incorporated in the SK model to account for the influence of surface roughness on scattering events. This adaptation stems from the fact that thermal motion causes wall atoms to deviate from their equilibrium positions, akin to the generation of a rough surface arising from a perfectly smooth plane. Here, the roughness refers to a contour governed by the static potential energy surface (PES), beyond which the movement of a gas molecule is inhibited. Notably, these hard gas–surface collisions align closely with the physical model described by Cercignani (1972, 1988) (see Section 2.2.4), who, however, disregarded the roughness and presumed a perfectly flat PES, where gas molecules are specularly reflected.

A pseudo Debye–Waller factor (PDWF) is proposed as follows:

$$\mathrm{PDWF} \sim \exp(-\langle(\hat{h}_A(\boldsymbol{k}) \cdot \boldsymbol{k})^2\rangle), \tag{6.4}$$

in which the surface height $\hat{h}_A(\boldsymbol{k})$ bears an analogous relation to the thermal displacement $\boldsymbol{u}$. The change of wavevector $\Delta\boldsymbol{k}_g$ in Eq. (6.3), resulting as an imprint of the wall on the scattered gas molecules, is replaced by the PES wavevector $\boldsymbol{k}$. This substitution conceptually indicates that alterations of gas wavevectors are directly proportional to the static surface wavevectors (Bass & Fuks, 2013; Beeby, 1971, 1972; Kuščer, 1978), which provides the basis for modelling of gas scattering on a rough surface.

Inspired by the expression of the DWF for harmonic potentials among wall atoms (Goodman & Wachman, 1976; Kittel, 2005), the PDWF for roughness may be given as:

$$\mathrm{PDWF} = \exp\left[-\int_{k_{\min}}^{k_{\max}} k^2 C_{2D}(k)\mathrm{d}k/\kappa^2\right], \tag{6.5}$$

where κ is a fitting constant (see Section 6.5.2) and serves as the characteristic wavevector for quantifying roughness intensity. The wave nature of the surface spectrum, as outlined in Section 6.2, hence lends a convenient and accurate method to compute the PDWF in Eq. (6.5), which can now be incorporated into a SK that models roughness.

6.3.3 A New Scattering Model, Incorporating Surface Roughness

A new scattering model is presented that accounts for the effects of random surface roughness at standard or elevated temperatures, where quantum mechanical features are suppressed and classical scattering description applies (Billing, 2000; Bird, 1994; Goodman & Wachman, 1976; Kuščer, 1978; Manson & Miret-Artés, 2022). For simplicity, the atomic-rough corrugations of the PES that arise from the crystal lattice structure are omitted. These corrugations are often imperceptible within the range of the largest feasible wavevectors k_c, given their characteristic lengthscale can be even smaller than the cut-off wavelength a.

Classical molecular scattering may be dominated by two types of interactions or collisions. The first category stems from the thermal motion of solid atoms, perceived as weak perturbations owing to the fluctuating surface potential. These interactions are denoted as gas–phonon collisions in scattering studies (Aoki & Giovangigli, 2019, 2021; Aoki et al., 2022; Borman et al., 1988; Brull et al., 2014, 2016; Krylov, 2003), leading to a spread or lobular pattern (not necessarily surrounding the specular line of reflection) of the re-emitted particles (see Fig. 6.2(b)). The second category encompasses hard gas collisions with a static PES. Substantial specular reflection is expected if the PES perceived by incident molecules is smooth on the scale of the de Broglie wavelength (Billing, 2000; Goodman & Wachman, 1976; Kuščer, 1978). However, when considering very rough random surfaces, the re-emitted molecules are more likely to display a diffuse pattern, as shown in Fig. 6.2(c), which arises from the elastically diffracted beams occurring across the surface (at different points). These two types of scattering dynamics coexist for practical surfaces that involve nanoscale roughness, as illustrated in Fig. 6.2(d).

The proposed SK therefore accounts for a linear combination of these weak and hard collisions. Specifically, this includes the CL model, denoted as $\mathscr{R}_{\mathrm{CL}}$, considered to provide the most accurate description of molecular interactions with a smooth surface in thermal equilibrium, and the fully diffuse Maxwell model, $\mathscr{R}_{\mathrm{d}}$, which characterises hard collisions on random rough

surfaces:

$$\mathscr{R}_{\mathrm{new},t} = B_1 \mathscr{R}_{\mathrm{CL},t}\left(\alpha_{t,0}\right) + (1 - B_1)\mathscr{R}_{\mathrm{d},t}, \tag{6.6a}$$

$$\mathscr{R}_{\mathrm{new},n} = B_2 \mathscr{R}_{\mathrm{CL},n}\left(\alpha_{E_n,0}\right) + (1 - B_2)\mathscr{R}_{\mathrm{d},n}, \tag{6.6b}$$

where

$$B_1 = \mathrm{PDWF}, \qquad B_2 = C_n(\mathrm{PDWF} - 1) + 1, \tag{6.6c}$$

in which $\alpha_{t,0}$ and $\alpha_{E_n,0}$ are the intrinsic magnitude of TMAC and NEAC for gas molecules on a thermal surface excluding roughness. These coefficients can be sourced either from beam experiments (Barker & Auerbach, 1984; Goodman & Wachman, 1976) conducted in low vacuum systems, provided the surface can be manufactured perfectly smooth, or by using MD simulations as done in this work.

In Eq. (6.6), the function B_1 signifies the fraction of molecules striking the surface without considerable alteration in their tangential velocity. This can be naturally related to the PDWF introduced in Section 6.3.2. Note, $B_1 = \mathrm{PDWF} = 1$ corresponds to a very smooth surface in thermal equilibrium. Its counterpart, $1 - B_1$, represents the fraction undergoing diffuse reflection, which relates the surface roughness intensity to the changes in tangential scattering dynamics. Unlike Maxwell's conception that diffusely re-emitted gas is linked to the depth of the 'stratum' (Maxwell, 1879), here it is found that both B_1 and $1 - B_1$ are, in fact, insensitive to penetration depth within the wall (see Appendix C); gas scattering dynamics are consistent across any stratum, provided the roughness characterisation remains similar at each level.

The function B_2 bears a similar meaning to B_1, albeit for the normal velocity component. It necessitates independent treatment because, unlike momentum, the energy accommodation to the state of the surface, describing the normal scattering dynamics, is recognised to be slower (Cercignani, 1988; Y. Chen et al., 2023, 2022). Regarding the evaluation of B_2, it can be postulated that either a straightforward fitting function or the simplest direct proportionality relationship, as indicated by the fitting constant $C_n \in [0, 1]$ in Eq. (6.6c), may exist in correlation with the PDWF.

The general TMAC and NEAC of the proposed SK readily follow:

$$\alpha_t = B_1 \alpha_{t,0} + (1 - B_1), \tag{6.7a}$$

$$\alpha_{E_n} = B_2 \alpha_{E_n,0} + (1 - B_2). \tag{6.7b}$$

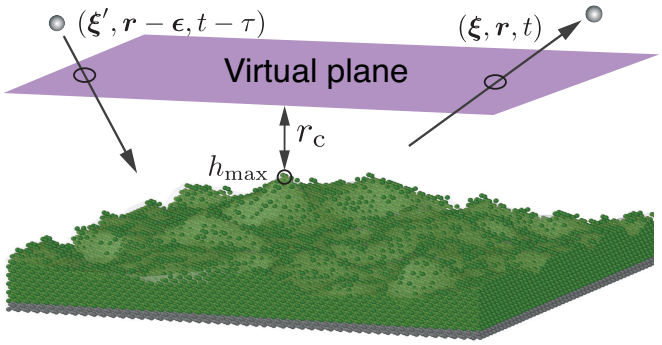

Figure 6.3: Schematic of the scattering dynamics of gas molecules near a rough FCC wall. Scattering information for incident (e.g., $\boldsymbol{\xi}', \boldsymbol{r} - \boldsymbol{\epsilon}, t - \tau$) and reflected (e.g., $\boldsymbol{\xi}, \boldsymbol{r}, t$) molecules is recorded at the virtual plane.

6.4 Modelling the Scattering Using MD

This study employs the MD method to simulate the scattering dynamics of gas molecules, using the open-source LAMMPS software (Plimpton, 1995). In the MD system, gas molecules are modelled as monatomic for simplicity. Chemically active or very heavy gas molecules, such as oxygen and xenon, are intentionally excluded from the MD setup. These molecules, due to their strong intermolecular potentials with wall atoms, may 'permanently' adsorb onto the surface, thus violating the assumption of negligible residence time.

The wall atoms are arranged in a face-centred cubic (FCC) configuration with a lattice parameter of 3.92 Å. Each wall is bounded by an outer edge of rigid wall atoms, inhibiting any wall movement, thereby maintaining the integrity of the defined system. Surface roughness is defined by imposing a power spectrum that maps directly onto crystal lattice coordinates, establishing a one-to-one correspondence between spectrum values and lattice locations to generate the desired roughness pattern. Moreover, periodic boundary conditions are implemented in the non-confined dimensions, with the roughness features seamlessly connected from one edge of the simulation box to the other. This consistent and connected roughness landscape ensures uniform GSIs across the entire simulation domain.

Two distinct groups of gas–surface combinations have been considered: helium-gold (He-Au) and argon-platinum (Ar-Pt), with each combination investigated under various rough surface power spectra. The interatomic interactions were modelled using the standard 12-6 Lennard-Jones (LJ) potential with a cut-off distance $r_c = 15$ Å, and the velocity-Verlet algorithm with a time step of 1 femtosecond (fs) was utilised to integrate molecular trajectories. The parameterised length σ and energy ε scales for He-Au and Ar-Pt interactions, again obtained from Liao et al. (2018) and Spijker et al. (2010) respectively, are listed in Table 5.1.

Each MD simulation run consists of two parts: equilibration and production. During equilibration, a Nosé–Hoover thermostat maintains both gas molecules and wall atoms at a constant temperature, with a 100 fs time constant in the NVT ensemble. Two temperatures, 300 K and 600 K, are adopted, representing typical room temperature conditions of MEMS/NEMS devices and a test of scattering dynamics at elevated temperatures, respectively. Following equilibration, the thermostat on the gas molecules is deactivated to prevent any bias in their scattering dynamics, and gas–gas interactions are disabled, ensuring GSIs remain unaffected by the presence of possible gas adsorbed layers. The production run yields extensive Lagrangian data, from which scattering information of interest can be extracted. A virtual plane shown in Fig. 6.3, positioned at $r_c + h_{\max}$ parallel to the plane of the average coordinates of the first layer of wall atoms, is used to flag atoms as they enter and exit the near-wall region, thereby defining the scattering events. Here, $h_{\max}$ represents the maximum height of the surface roughness. The inclusion of $h_{\max}$ extends the near-wall region to include the influence of every wall atom. This extension does not affect the scattering dynamics since gas–gas interactions are disabled.

6.5 Results and Discussion

In this section, the expected features of surface roughness in the MD studies are verified, elaborating on the computation of the PDWF from the PES measurement (Section 6.5.1). Following this, the constants within the proposed SK are calibrated to best align with TMACs and NEACs across varying roughness intensities (Section 6.5.2). Section 6.5.3 demonstrates that the proposed SK accurately predicts scattering dynamics under different test conditions. Finally, comparing macroscopic quantities derived from SK outcomes with those produced by rough explicit walls further demonstrates the better prediction of the proposed model over other existing SKs (Section 6.5.4).

6.5.1 Surface Roughness in MD and the Computation of PDWF

A sample rough surface is generated within the MD setup using the surface power spectrum method, which provides the coordinates of the interfacial wall atoms, as shown in Fig. 6.4(a). Subsequently, Fig. 6.4(b) displays the corresponding PES measurement for this rough surface. In this study, the potential energy experienced by a molecule is mapped onto a grid and calculated as an ensemble average during the MD production run. The PES is then measured as a contour level where the potential energy is zero, $U(\boldsymbol{r}) = 0$, which, according to standard LJ potentials, signifies coordinates approximately one molecular diameter (σ) away from the wall atoms' centre of mass. Upon comparison, Figs. 6.4(a,b) exhibit a close resemblance with an expected shift of σ in the normal direction. After adjusting their coordinate origins to a zero mean, a radial average on the calculated discrete Fourier transform is performed for both surface topographies in Figs. 6.4(a,b) to derive their power spectra, as shown in Fig. 6.4(c).

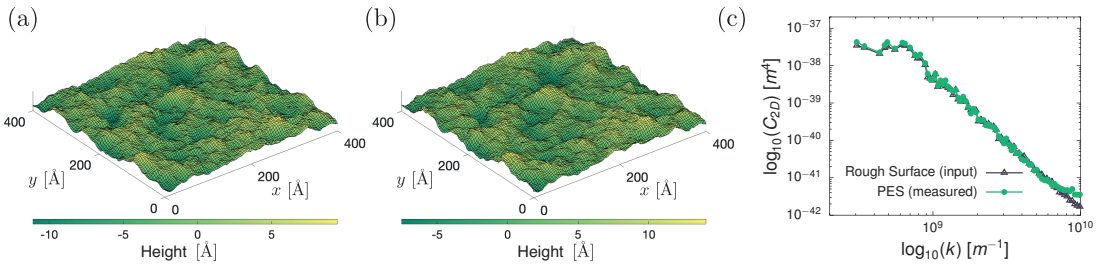

Figure 6.4: (a) Coordinates of a sample random rough surface, with a root mean square (RMS) of 3 Å and Hurst exponent $H_q = 0.8$; (b) PES measurement corresponding to the rough surface, obtained from the MD simulation of He-Au system at an equilibrium temperature of 300 K; (c) Comparison of the two power spectra measured from the atom surface coordinates of panel (a) and the PES coordinates (defined at $U(\boldsymbol{r}) = 0$) of panel (b).

The similarities between the input and PES-derived spectra, despite some minor differences near the crystal structure dimension a, show that the measured PES resembles quite well the atom-defined roughness. In the computation of the PDWF, which is a wavevector-weighted moment of the spectrum formulated by Eq. (6.5), the measured PES is used because it reflects the actual irregularities felt by gas molecules. However, the results in Fig. 6.4 indicate that the error would be small had the PDWF been calculated using the roughness arising from the surface-atom positions. This approach of using PES wavevectors, determined when the molecule is near the bottom of the potential well, also follows the methodologies proposed by Beeby (1971, 1972) and Goodman (1977) for evaluating classical DWF.

6.5.2 Calibration of Scattering Model

The proposed SK hinges on two sets of parameters: $\{\alpha_{t,0}, \alpha_{E_n,0}\}$, which feature the scattering dynamics from a thermal, smooth surface, and $\{\kappa, C_n\}$, which account for the surface roughness effects. The first two parameters are obtained by evaluating TMAC and NEAC from MD simulations on a thermal smooth FCC surface without any defects at the periodic boundaries, while the remaining two parameters are calibrated by fitting Eq. (6.7) and Eq. (6.5) with the TMAC and NEAC values corresponding to various intensity of surface roughness, also determined by MD simulations. These ACs are presented in Fig. 6.5 for the sample cases of He-Au and Ar-Pt systems at two distinct temperatures (solid symbols), where the x-error bars indicate the discrepancy between the PDWF given by the input and measured spectra. It can be observed that the errors in the Ar-Pt system are more pronounced, attributable to its smaller GSI molecular diameter σ. This smaller diameter leads to increased corrugation of PES near the wall lattice structure, resulting in more significant discrepancies. Linear fitting curves were applied to the measured PES spectra points (based on Eq. (6.5) where κ is the fitting constant) for the tangential component, revealing a satisfactory agreement across different temperatures and systems. A summary of all parameters extracted from these MD simulations is listed in Table 6.1 for further reference.

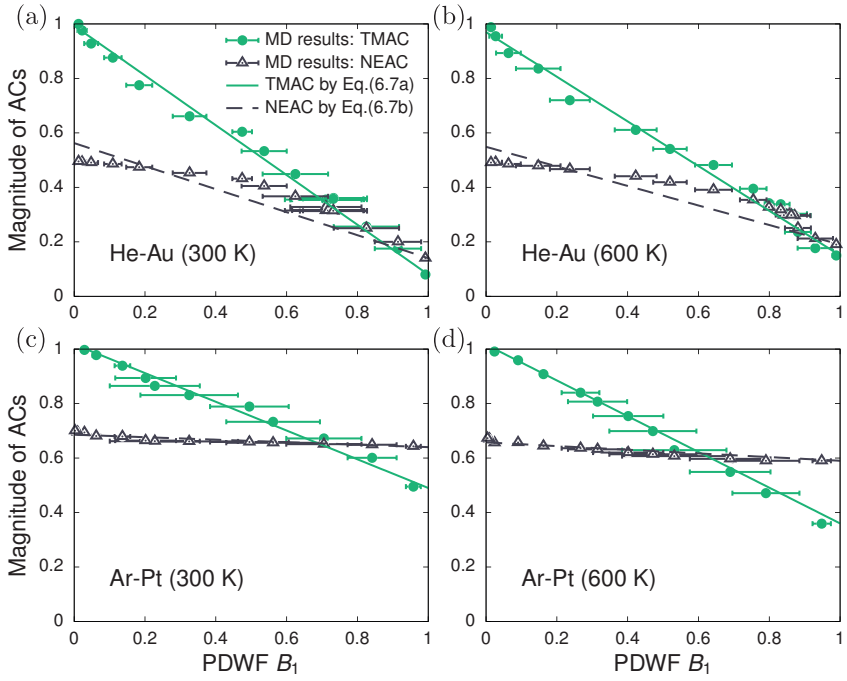

Figure 6.5: Variation of the general accommodation coefficients with PDWF given by MD results for the He-Au system at (a) 300 K and (b) 600 K; the Ar-Pt system at (c) 300 K and (d) 600 K.

Table 6.1: Reference values for the intrinsic accommodation coefficients ($\alpha_{t,0}, \alpha_{E_n,0}$) and the calibrated constants (κ, C_n).

	$\alpha_{t,0}$		$\alpha_{E_n,0}$		κ		C_n	
	300 K	600 K	300 K	600 K	300 K	600 K	300 K	600 K
He-Au	0.08	0.15	0.14	0.19	5.31e-06	5.43e-06	0.47	0.44
Ar-Pt	0.49	0.36	0.64	0.59	5.03e-06	5.24e-06	0.09	0.11

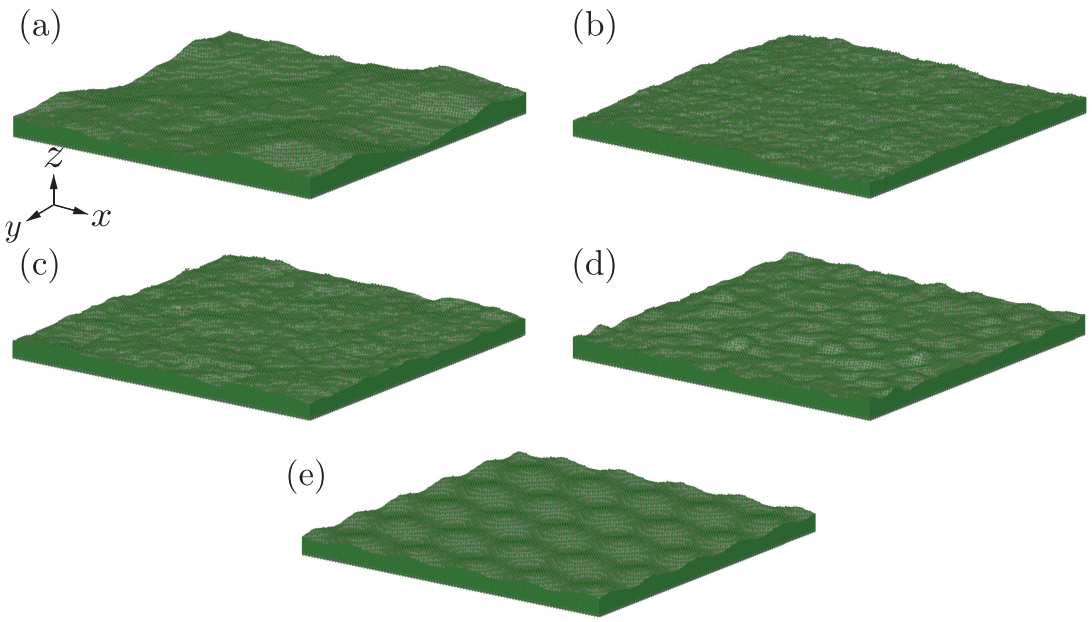

Figure 6.6: MD visualisations of random rough surfaces chosen with different spectra, but having the same PDWF = 0.7. (a–d) correspond to Cases A–D, and (e) corresponds to the sinusoidal rough surface.

Two remarks are worth making regarding the results reported in Fig. 6.5. First, the slope of NEAC is consistently smaller than that of TMAC, regardless of the temperature and gas–surface combination. This highlights the slower accommodation of energy compared to momentum and indicates a lower influence of roughness on the normal component, thereby necessitating the introduction of the parameter C_n in Eq. (6.6). Second, unlike the constant κ that seems to universally fit all data sets for the tangential component, the parameter C_n does not, and is dependent on the gas–surface combinations.

6.5.3 Scattering Dynamics on Rough Surfaces at Constant PDWF

In this section, the scattering dynamics are assessed and the role of the PDWF in the proposed SK model is investigated. Diverse rough surface spectra are first constructed, all corresponding to the same PDWF value of 0.7, represented by five cases: four random rough surfaces (denoted as cases A–D) and one sinusoidal rough surface. Their visualisation in the MD domain is presented in Fig. 6.6, and their spectra are shown in Fig. 6.7(a). Gas molecules re-emitted from these surfaces with varied roughness but the same PDWF should, in principle, exhibit similar scattering dynamics. In these simulations, the tangential and normal scattering components are treated as decoupled, dividing incident molecules into distinct monoenergetic beams. This is achieved by selecting molecules whose tangential (or normal) velocity components are within the range of $[\xi', \xi' + \Delta\xi']$. Subsequently, the beam ACs and the re-emission probabilities of

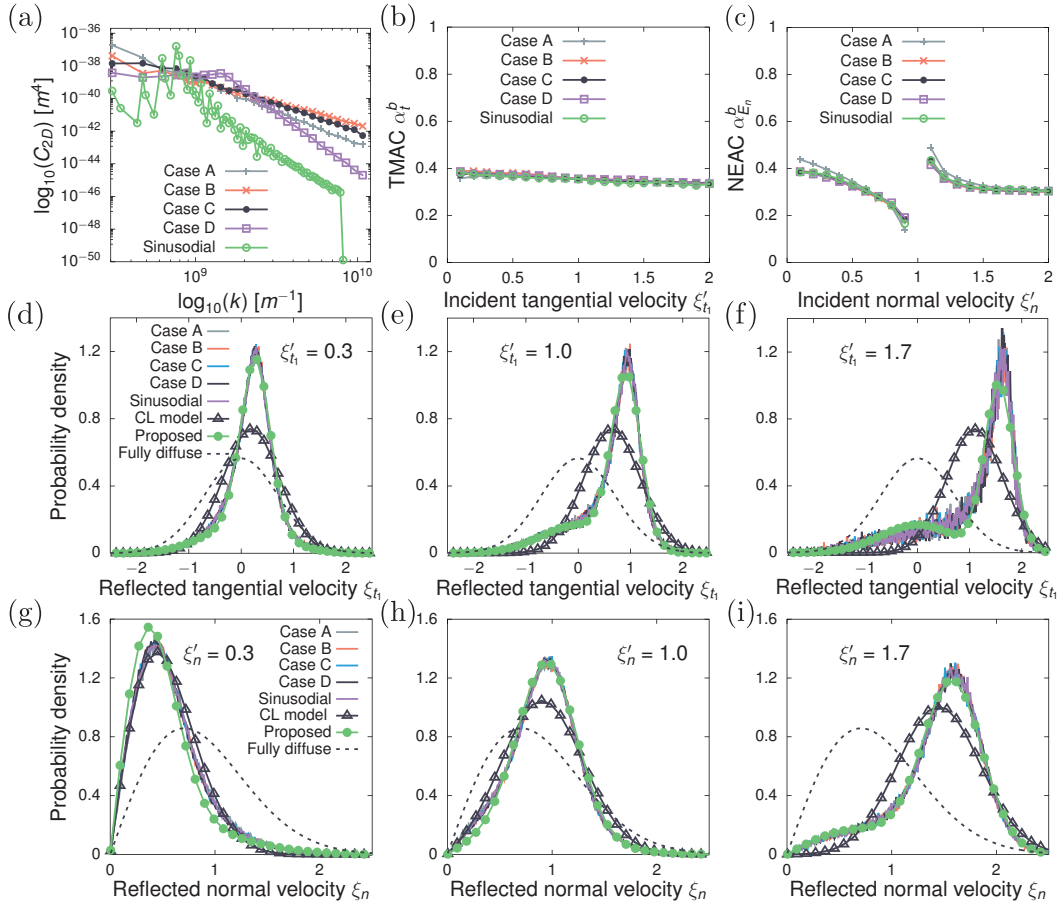

Figure 6.7: (a) Rough surfaces chosen with different spectra, but having the same PDWF = 0.7. The impact of the roughness of the chosen surfaces on scattering dynamics is shown through (b) beam TMACs, and (c) beam NEACs from the He-Au system at an equilibrium temperature of 300 K; comparison of the reflected velocity distribution for the (d-f) tangential and (g-i) normal velocities for monoenergetic beams predicted by MD and all scattering models. Velocities of the beams are normalised by the most probable speed $\sqrt{2RT}$.

the velocity components within each range are determined. These numerical MD results are then compared with the theoretical predictions given by the proposed SK. In addition, for a more comprehensive analysis, comparisons are also made with SKs available in the existing literature.

Figs. 6.7(b,c) provide a comparison between the beam TMAC and NEAC measurements. It is apparent that the magnitude and velocity dependence of these ACs align quite closely. While beam ACs may largely depend on the impinging velocity (Yamamoto et al., 2007), this dependence is very weak in the systems simulated in this work. Hence, general ACs are employed here for predicting scattering patterns for simplicity. Finally, numerical artefacts in the normal component are observed around the most probable speed in Fig. 6.7(c), as also noted by Yamamoto et al. (2007) and Spijker et al. (2010).

Figs. 6.7(d-f) present a comparison between the tangential scattering patterns of monoenergetic beams and those predicted by various SKs, including the fully diffuse, the CL, and the proposed model. Representative incident velocities, ξ_{t_1}', are set at 0.3, 1.0, and 1.7. As can be seen, the scattering patterns obtained from surfaces with diverse spectra but identical PDWFs show considerable similarity, reinforcing the idea that PDWF is the key metric governing scattering on rough surfaces. It is evident that surfaces with different PDWFs will result in varying ACs, as seen in Fig. 6.5. Moreover, the proposed SK model best captures all the MD scattering patterns, incorporating two fractions representing the CL model (associated with weak perturbations) and the fully diffuse model (associated with hard collisions). However, when applied independently, neither the CL nor the fully diffuse model can well capture these patterns.

In the normal direction, as shown in Fig. 6.7(g-i), the proposed scattering model continues to offer the best agreement with the MD data, notwithstanding a minor deviation at the incident velocity $\xi_n' = 0.3$, attributed to the utilisation of general ACs. However, such discrepancies are expected to have a negligible impact on macroscopic quantities, given the small weighting of gas molecules at this incident velocity.

Numerical scattering experiments were also conducted under various temperature conditions and gas–surface combinations. Similar qualitative trends were observed across all the systems studied, the details of which are presented in Appendix D.

6.5.4 Validation of the New SK under Heat and Flow

The final aspect of validating the proposed SK model involves assessing the accuracy of macroscopic flow profiles across a parallel channel. Here, MD results from explicit physical walls will serve as the benchmark for comparison. Two problems are considered separately: (a) the force-driven Poiseuille flow, and (b) the Fourier flow problem. In the Poiseuille flow scenario, an external force is applied to each gas atom in the streamwise direction, with the magnitude maintained small enough to keep the flow within the linear regime. The Fourier flow problem, on the other hand, involves only applying a temperature change across the channel, allowing for an examination of how scattering dynamics influence temperature jumps at the walls.

For the MD benchmark simulations with explicit walls, gas–gas interactions are switched off, indicating that the flow systems are at an infinite Knudsen number ($Kn \to \infty$). This setup confirms that the influence on gas flow is solely due to GSIs. All SK models, including fully diffuse, Maxwell, CL, and the proposed model, were implemented in LAMMPS. In these MD simulations, the explicit atomic walls are replaced with stochastic walls, where the SK models determine the reflection behaviour of incoming gas molecules, and the omission of wall atoms significantly reduces computational demands. It is important to emphasise that within kinetic theory, SKs are implemented at virtual planes, the sites of scattering measurements.

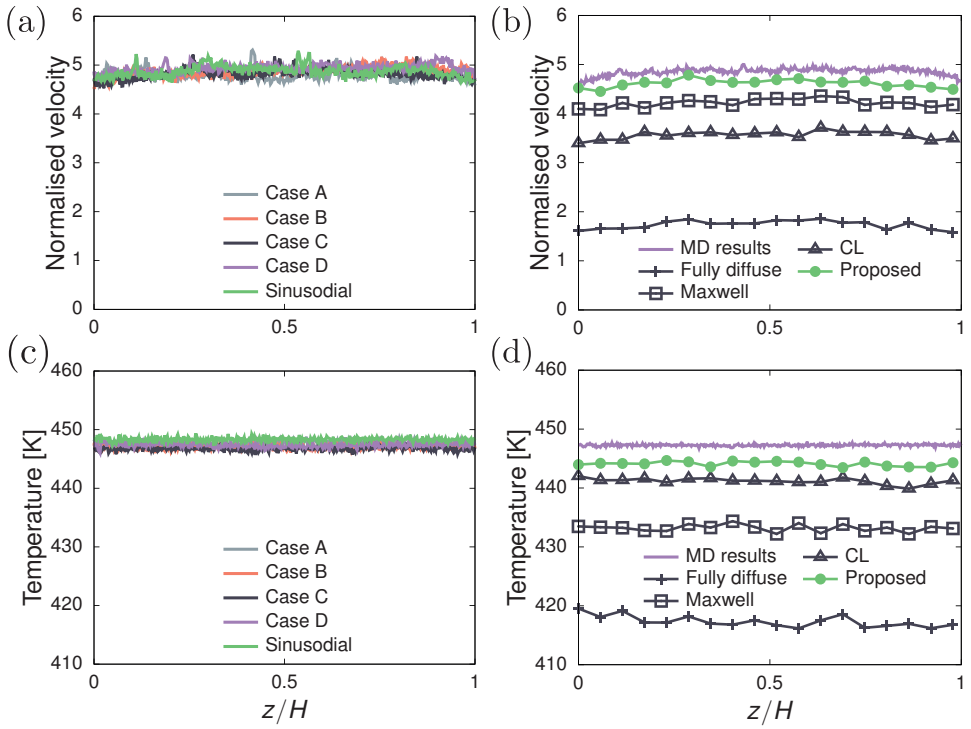

Figure 6.8: Comparison of normalised velocity profiles for Poiseuille gas flow in the He-Au system at 300 K: (a) from MD simulations with explicitly constructed wall atoms and deactivated gas–gas interactions ($Kn \to \infty$), where $z/H \in [0,1]$ indicates the region between virtual planes; and (b) from MD simulations employing stochastic walls, i.e., SKs, with active gas–gas interactions ($Kn \approx 461$). Temperature profiles for a Fourier flow problem: (c) explicitly constructed wall atoms (bottom wall set at 600 K and top wall at 300 K); and (d) stochastic walls.

The distance between these planes defines the effective channel height H, which is chosen to be sufficiently large to prevent confinement effects (Corral-Casas, Chen, Borg & Gibelli, 2024; Corral-Casas, Li, Borg & Gibelli, 2022; Shan, Su, Gibelli & Zhang, 2023; Sheng et al., 2020). Due to code limitations within LAMMPS, gas–gas interactions had to be maintained in the stochastic wall simulations. However, the lateral dimensions of the system were ensured to be sufficiently large to effectively maintain a high Knudsen number.

Fig. 6.8(a) presents normalised velocity profiles of gas flow within channels formed by different rough walls but under the same PDWF= 0.7, i.e., cases A-D and sinusoidal. For different cases considered, the velocity profiles within the effective channel H remain flat and in agreement with each other, consolidating the exclusive impact of scattering dynamics on velocity slip. Fig. 6.8(b) shows the average of velocity profiles obtained from the MD simulations using explicit physical walls, and compares it with those using SK stochastic walls. While the comparison reveals that a very small curvature exists in the velocity profile, caused by the Knudsen number not being truly infinite, there are significant discrepancies between the results of the different SKs. The proposed SK gives a better agreement with the benchmark MD results.

Figs. 6.8(c-d) show results similar to those in Figs. 6.8(a-b), albeit for the Fourier flow problem. As expected, in Fig. 6.8(c), the temperature profiles and temperature jumps given by the MD simulations of physical walls are similar. Notably, Fig. 6.8(d) reveals that both the CL model and the proposed model provide close predictions to the benchmark MD simulations than the other SKs. This closer agreement between CL and the proposed model may be attributed to the characteristics of the Fourier flow problem, particularly its relative insensitivity to the tangential scattering component, which is more affected by roughness.

6.6 Conclusions

This work investigated the impact of nanoscale roughness on gas–surface scattering. Existing scattering kernels (SKs) do not contain enough information of the surface roughness features, and the quantitative relationship between the ACs, the gas scattering patterns and the roughness remain unclear. To address this, a new SK has been proposed, as a simple linear combination of the Cercignani–Lampis (CL) and Maxwell fully diffuse models. This combination is grounded in the rationale that the CL term accurately describes the gas scattering dynamics upon a thermal, smooth surface (dominated by weak perturbations from gas–phonon collisions), whilst the Maxwell fully diffuse term captures the hard collisions resulting from the irregularities of rough surfaces. In this work it was found that the weighting coefficient between the two models is elegantly described by a proposed pseudo-Debye–Waller factor (PDWF), inspired by an analogy that roughness can be seen as waves superimposed on flat planes. The PDWF was evaluated via the power spectrum of the static potential energy surface (PES), which can be easily obtained by molecular dynamics (MD) simulations or experiments. The accuracy of various SKs were assessed using high-fidelity MD simulations, demonstrating that the proposed SK delivers the best agreement with the benchmark MD simulations across the range of tested systems with varied roughness, temperature, and gas–surface combinations.

Chapter 7

Concluding Remarks

7.1 Summary

This thesis sheds light on the dynamics of GSIs at the nanoscale, where the physical landscape is molecular in nature and dominated by the inhomogeneity introduced by the presence of the solid. To effectively capture the dynamical behaviours, detailed investigations using established modelling tools are needed, as conventional approximations underpinning prevalent scattering models are inadequate to capture the complex wall physics. This complexity is largely attributed to our limited understanding of the intermolecular potential between gas molecules and wall atoms, coupled with the vibration of wall atoms, both of which affect the intrinsic structure of the surface layers. The research presented in this thesis employs MD simulations using a standard LJ fluid confined between two explicitly modelled walls with thermal motion, inherently capturing the essential physics and deterministically simulating the dynamics of GSIs. This high-fidelity approach provides an effective representation of scattering experiments and allows for direct comparison with the predictions of conventional scattering models, especially under small perturbations consistent with the linear regime.

The first study focused on the scattering dynamics of methane from organic kerogen surfaces, characterised by porosity, roughness, adsorption, and elevated pressures/temperatures. These factors result in distinct methane scattering behaviours in shale reservoirs, diverging from those observed on controllable metal surfaces. A key finding of this study is that the assumption of instantaneous and local interactions, which supports the use of conventional SKs, holds for scattering on porous kerogen surfaces when the flow is steady and low-speed. While most prevalent SKs are found unable to capture the detailed scattering patterns on kerogen surfaces, the Maxwell model satisfactorily predicts velocity profiles and overall mass flow rates across a broad range of Knudsen numbers. These findings affirm the applicability of the Maxwell model for modelling gas transport near kerogen or other mineral surfaces and establish a foundation for exploring individual factors influencing scattering dynamics, such as physisorption and surface roughness.

The inhomogeneity of the surface layer (potential) due to adsorbed gas molecules, as well as the development of SKs that account for adsorption, have been largely overlooked. Yet, evidence from experiments, theory analyses, and simulations suggests that disregarding adsorbed molecules oversimplifies scattering dynamics, leading to inaccuracies in fluid flow predictions. To address this limitation, a SK is proposed that linearly combines the Cercignani-Lampis and Maxwell fully diffuse models, using the Langmuir isotherm as a weighting factor. The rationale behind this modelling approach is that the CL term effectively describes the scattering process from a clean, smooth surface at thermal equilibrium, whereas the Maxwell fully diffuse term is expected to capture the effect of gas–gas interactions when an adsorbed gas layer forms next to the surface. While this new model has shown the best capture of scattering dynamics in MD simulations compared to other widely used models, further work may be needed to incorporate the physics of the adsorbed layer, making it a more effective boundary model for heat and flow transport in tightly confined nanochannels.

Another contributor to the inhomogeneity of the surface layer stems from nanoscale surface irregularities, caused by the height variation of wall atoms on the order of a few nanometres. Considerable efforts have been made to explore how these irregularities influence rarefied gas transport. However, existing SKs, which fundamentally govern the transport, often omit detailed information on surface roughness, leaving the quantitative relationships among accommodation coefficients, gas scattering patterns, and surface roughness to be further clarified. To address this, a SK is developed, again as a linear combination of the CL and Maxwell fully diffuse models. The CL term models smooth surfaces at thermal equilibrium, while the Maxwell term accounts for collisions brought by nanoscale irregularities. The weighting coefficient between the two models is described by a proposed pseudo Debye–Waller factor, viewing roughness as wave-like distortions on flat surfaces. High-fidelity MD simulations confirmed the accuracy of the proposed model across various conditions, showing the best agreement with MD benchmarks in systems with varying roughness, temperatures, and gas–surface combinations. The proposed SK can, therefore, be readily applied to study rarefied gas transport systems, such as those in aerospace and MEMS/NEMS, where interface roughness is considered random and multiscale.

The focus of the investigation into GSIs in this thesis adheres to the principle underpinning SKs: simplicity with constraints. This simplicity is rooted in the general form formulated by Cercignani (1988) and Kuščer et al. (1971), which underlies other models through linear combinations summing to unity. The proposed models aim to integrate realistic physics into SK theory, simplifying the complex phenomena of GSIs for more manageable analysis, understanding and seamless integration into rarefied gas computational methods, such as in direct simulation Monte Carlo (DSMC) and direct velocity methods (DVM). On the other hand, constraints in SK theory primarily arise from the property of reciprocity, which is seemingly invalidated in many flow situations (Bärwinkel & Schippers, 1989), thereby limiting

the scope of gas flow scenarios that can be considered. To capture more detailed GSIs and thereby improve rarefied flow transport modelling, the reciprocity constraint must sometimes be relaxed, although this will require further investigation. Below are proposed future research directions to continue contributing towards progress in this field.

7.2 Future Work

This thesis research has focused on developing new SKs models by incorporating the key physics of the surface features being modelled. The adaptability of the simulation setup allows its application to further problems, such as investigating the role of long-range attractive interactions in GSIs and their impact on nanoscale flow transport.

Conventionally, SKs presuppose that the scattering process is instantaneous and local. However, interactions between gas molecules and wall atoms may span across the entire characteristic flow length in nanoscale confinements, such as shown in Fig. 7.1(a). This necessitates accounting for the residence time and displacement during scattering to reflect the time of flight and the distance traversed within the potential field, respectively, rendering these factors important to be considered. Moreover, as shown in Fig. 7.1(b), the presence of attractive forces can lead to the adsorption of gas molecules onto the surface, challenging the prevailing assumption of negligible residence time. Consequently, it becomes imperative to incorporate the influence of long-range interactions, considering time-delay and non-local effects, in the further development of kinetic boundary conditions for nanochannels.

The proposed SK in Chapter 5 effectively captures the impact of physisorption on scattering dynamics. However, its extension to account for temporal variations, c.f. Brancher et al. (2020); Takata et al. (2021), could further enhance the understanding of unsteady flow problems, such as evacuation speed prediction in vacuum technologies. Additionally, physisorbed molecules often exhibit mobility as they travel along the surface layer, thus introducing surface diffusion shown in Fig. 7.1(b) as an important transport mechanism in nanoscale confined spaces. While the decisive factor for this mechanism is known to be the thermal motion of adsorbate with respect to the minimum energy difference between adjacent adsorption sites (Barth, 2000), addressing this problem in its full complexity, including variations in gas–surface species and lattice structures, remains a significant challenge.

On the other hand, physisorption and the related surface diffusion can be modelled within the physical framework proposed by Cercignani (1972, 1988). This framework has been illustrated in Fig. 2.4. Rather than suppressing long-range interactions, it is now necessary to take them into account, potentially causing non-instantaneous and non-local scattering effects. This consideration naturally prompts the question: Could extending Cercignani's physical framework — a kinetic boundary condition integrating a stochastic equation or even a simple

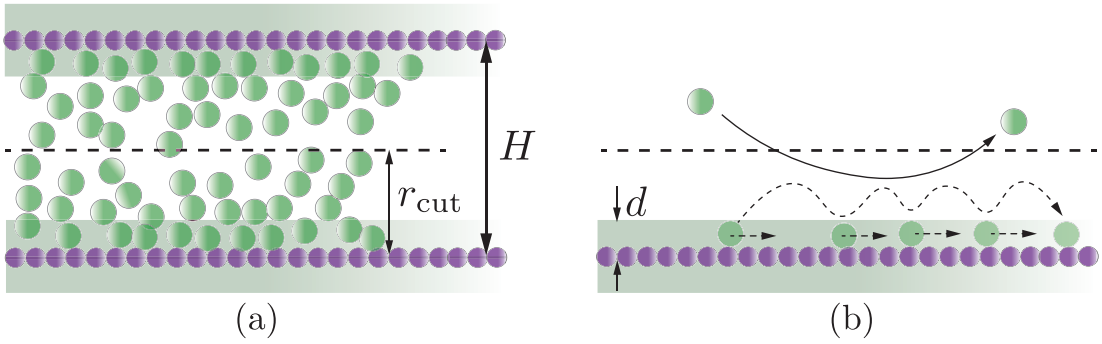

Figure 7.1: (a) GSIs for dense gas flows in nanochannels. (b) GSIs under surface diffusion.

CL model, supplemented with long-range attractive forces — enable more accurate predictions of molecular motion within the surface layer? This line of inquiry is particularly compelling given that the indicator of attractive forces, the potential energy depth, is widely used in GSI studies (Liang et al., 2018; Tully, 1990; Yamanishi, Matsumoto & Shobatake, 1999) to assess whether gas molecules scatter, re-enter, or become trapped by the surface. Furthermore, kinetic treatments of surface diffusion (Aoki et al., 2011; Krylov, 2003; Krylov, Beenakker & Tringides, 1999) have already incorporated the FP model (as seen in the derivation of the CL model), including the closely related Langevin systems and BGK-like models, for particle-substrate-bath coupling. This FP approach may offer a more comprehensive description of surface migration, particularly compared to the traditional transition state theory (TST) (Barth, 2000; Krylov et al., 1999). While TST is limited to accounting for single hops to neighbouring adsorption sites and fails to consider longer jumps that naturally occur in the weak adsorption limit, the FP approach is capable of capturing both scenarios.

Another fascinating area of research is the macroscopic phenomenon of velocity slip in molecularly confined channels, emerging from boundary-induced inhomogeneity (Hadjiconstantinou, 2024). This inhomogeneity is accentuated by the consideration of long-range interactions, leading to a naturally more pronounced stratification within the surface layer. At the molecular level, the slip phenomenon results from a complex interplay of the aforementioned gas–surface scattering, surface diffusion, and gas–gas interactions. These microscopic factors, while individually significant, are collectively shaped by long-range attractive forces, a fact often considered in isolation within existing slip models (Corral-Casas et al., 2024; Martini, Roxin, Snurr, Wang & Lichter, 2008; Maxwell, 1879; Myong, 2004; Shan et al., 2022; G. J. Wang & Hadjiconstantinou, 2019). It would, therefore, be interesting to explore whether the influence of long-range forces on GSIs could be successfully unified and incorporated within kinetic theory, thereby contributing to the straightforward description of velocity slip in the Navier-Stokes framework.

Appendix A

Implementation of Scattering Kernels

The general form of SKs can be readily implemented in particle-based simulations, such as MD and direct simulation Monte Carlo (DSMC), using an adapted polar form of the Box-Muller algorithm. This adaptation was initially depicted through a geometrical representation of the CL model by Lord (1991), who also expanded the CL model's applicability by incorporating the internal degrees of freedom for polyatomic gas molecules. This expansion led to the development of what is sometimes referred to as the Cercignani-Lampis-Lord (CLL) model. The geometrical representation can be uniformly applied to both the normal and tangential velocity components, as well as the angular velocity components. This is demonstrated in Fig. A.1, where the molecular states correspond to points within the diagram. The corresponding algorithm for implementing the general form, following the symbols from Eq. (2.28), is listed in Table A.1 for further reference.

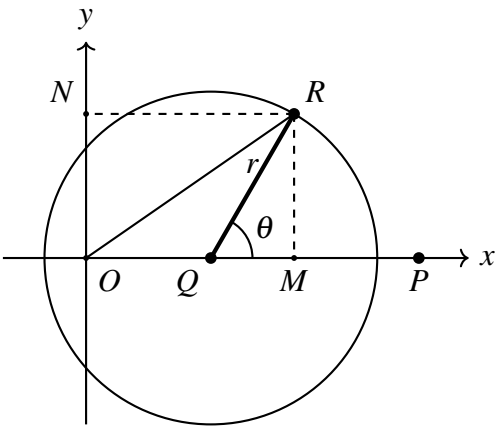

Figure A.1: Geometrical representation of the general form of SKs. Point P represents the incident state, while point Q indicates the average state of the re-emitted molecules. The ratio between OQ and OP is related to the accommodation of momentum; specifically, $OQ/OP = \mu$, in accordance with the form of Eq. (2.30). Alternatively, $OQ/OP = q$ corresponds to the tangential components, and $OQ/OP = \sqrt{p}$ for the normal component, as per the form of Eq. (2.28). Point R indicates the actual state of the re-emitted molecules, with the probability of this state distributed according to a 2-D Gaussian distribution centred on Q. Moreover, r represents the distance QR, and θ is the angle at PQR. The projections of QR onto the axes thus represent the reflected velocity components.

Auxiliary: U_i $(i = 1, 2, 3...)$ are independent samples chosen from the uniform distribution on the unit interval [0, 1]; $q \in [-1, 1]$ and $p \in [0, 1]$ as per form of Eq. (2.28).

Tangential components	**Normal component**
$\theta_1 = 2\pi U_1$ $r_1 = \sqrt{-2\ln U_2} \cdot \sqrt{1-q^2}$	$\theta_2 = 2\pi U_3$ $r_2 = \sqrt{-2\ln U_4} \cdot \sqrt{1-p}$
$\langle \xi_{t_1} \rangle = \xi'_{t_1} q$ $\langle \xi_{t_2} \rangle = \xi'_{t_2} q$	$\langle \xi_n \rangle = \xi'_n \sqrt{p}$
$\xi_{t_1} = \langle \xi_{t_1} \rangle + r_1 \cos(\theta_1)$ $\xi_{t_2} = \langle \xi_{t_2} \rangle + r_1 \sin(\theta_1)$	$\xi_n = \sqrt{[\langle \xi_n \rangle + r_2 \cos(\theta_2)]^2 + [r_2 \sin(\theta_2)]^2}$

Table A.1: Algorithm equations for the general form of SKs. The surface is assumed to be isotropic; therefore, it possesses equivalent scattering dynamics for the two tangential velocity components. Velocities are normalised by the reference speed $\sqrt{RT}$.

Appendix B

Generating Random Rough Surfaces Based on Specified Power Spectral Density

This appendix provides a concise description of the algorithm used to generate a random rough surface with a specified power spectral density (PSD). The algorithm ensures that the generated surface has the desired statistical properties, including a specified root-mean-square (RMS) roughness and fractal characteristics controlled by the Hurst exponent H.

Algorithm Steps

1. **Input Parameters**
   - RMS roughness σ.
   - Hurst exponent H.
   - Surface length $\mathscr{L}$ (assumed equal in x and y directions).
   - Number of pixels N_x, N_y in x and y directions.
   - Optional roll-off wave vector k_{roll} (default to 0 if not specified).
2. **Prepare Grid and Wave Vectors**
   - Ensure N_x and N_y are even.
   - Compute pixel width (i.e., the lattice constant):

$$a = \frac{\mathscr{L}}{N_x}$$

   - Define wave vectors:

$$k_x = \frac{2\pi}{\mathscr{L}}\left(-\frac{N_x}{2}, -\frac{N_x}{2}+1, \ldots, \frac{N_x}{2}-1\right)$$

$$k_y = \frac{2\pi}{\mathscr{L}}\left(-\frac{N_y}{2}, -\frac{N_y}{2}+1, \ldots, \frac{N_y}{2}-1\right)$$

   - Create 2D grid:

$$K_X, K_Y = \text{meshgrid}(k_x, k_y)$$

- Compute radial wave vector magnitude:

$$k_{i,j} = \sqrt{K_X^2 + K_Y^2} \quad \text{where} \quad i,j \in \mathbb{Z} \quad \text{and} \quad 1 \leq i,j \leq N_x$$

3. **Compute the Power Spectral Density** $C(k)$
   - For each $k_{i,j}$, compute:

$$C(k) = C_{i,j} = \begin{cases} k_{\text{roll}}^{-2(H+1)}, & \text{if } k_{i,j} < k_{\text{roll}} \\ k_{i,j}^{-2(H+1)}, & \text{if } k_{i,j} \geq k_{\text{roll}} \end{cases}$$

   - Set zero-frequency component to zero:

$$C_{\frac{N_y}{2},\frac{N_x}{2}} = 0$$

4. **Scale PSD to Match Desired RMS Roughness**
   - Compute initial RMS:

$$\text{RMS}_{\text{initial}} = \sqrt{\sum_{i,j} C_{i,j} \left(\frac{(2\pi)^2}{\mathscr{L}_x \mathscr{L}_y} \right)}$$

   - Compute scaling factor:

$$\text{const} = \frac{\sigma}{\text{RMS}_{\text{initial}}}$$

   - Scale PSD:

$$C_{i,j} = C_{i,j} \times \text{const}^2$$

5. **Compute Fourier Magnitudes** $|\hat{h}_A|$
   - Convert PSD to Fourier magnitudes:

$$|\hat{h}_A|_{i,j} = \sqrt{\frac{C_{i,j}}{\left(\frac{a^2}{N_x N_y (2\pi)^2} \right)}}$$

   - Enforce conjugate symmetry on $|\hat{h}_A|$:
     - Set specific elements to zero:

$$|\hat{h}_A|[0,0] = |\hat{h}_A|[0,N_x/2] = |\hat{h}_A|[N_y/2,0] = |\hat{h}_A|[N_y/2,N_x/2] = 0$$

     - Mirror the magnitudes to enforce symmetry.

6. **Generate Random Phases** $\phi_{i,j}$
   - Assign random phases uniformly in $[-\pi,\pi]$.

- Enforce conjugate symmetry:

$$\phi_{N_y-i,N_x-j} = -\phi_{i,j}$$

- Set specific elements to zero:

$$\phi[0,0] = \phi[0,N_x/2] = \phi[N_y/2,0] = \phi[N_y/2,N_x/2] = 0$$

7. **Form Complex Fourier Coefficients**
   - Combine magnitudes and phases:

$$\hat{h}_A = |\hat{h}_A| \times e^{i\phi}$$

8. **Generate Surface Height Profile**
   - Perform inverse Fourier transform:

$$z = \mathrm{Re}\left\{\mathrm{IFFT2}\left(\hat{h}_A\right)\right\}$$

   - z is the real-valued surface height profile.

Notes

- **Conjugate Symmetry**: Ensures that the inverse Fourier transform yields a real-valued surface.
- **Random Phases**: Introduce randomness while maintaining the specified statistical properties.
- **Scaling**: Adjusts the PSD to match the desired RMS roughness σ.
- **Roll-off Wavevector** k_{roll}: Defines a cutoff frequency below which the PSD becomes constant.

Appendix C

Rough Surfaces: On the Impact of Penetration Depths

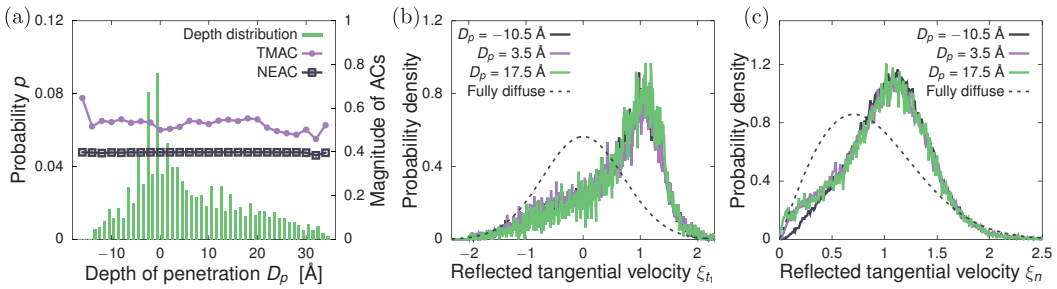

Figure C.1: (a) Depth of penetration distribution for gas molecules on a rough surface with RMS = 10 Å and $H_q = 1.0$ (PDWF ≈ 0.54). Re-emission probability distribution for a monoenergetic molecular beam, with example cases of (b) tangential impinging velocity $\xi'_{t_1} = 1.3$ and (c) normal impinging velocity $\xi'_n = 1.3$.

Figs. C.1(a-c) demonstrate consistent scattering dynamics independent of stratum depth. This is showcased both via the ACs (Fig. C.1(a)), and the gas re-emission probability density distributions for tangential and normal components (Fig. C.1(b,c)), which convey more detailed information of the scattering patterns at different depths. Notably, the tangential scattering patterns are asymmetric, diverging from the symmetry intrinsic to the CL and fully diffuse reflection models, suggesting the coexistence of different collision patterns in GSIs.

Appendix D

Rough Surfaces: On the Impact of Temperatures

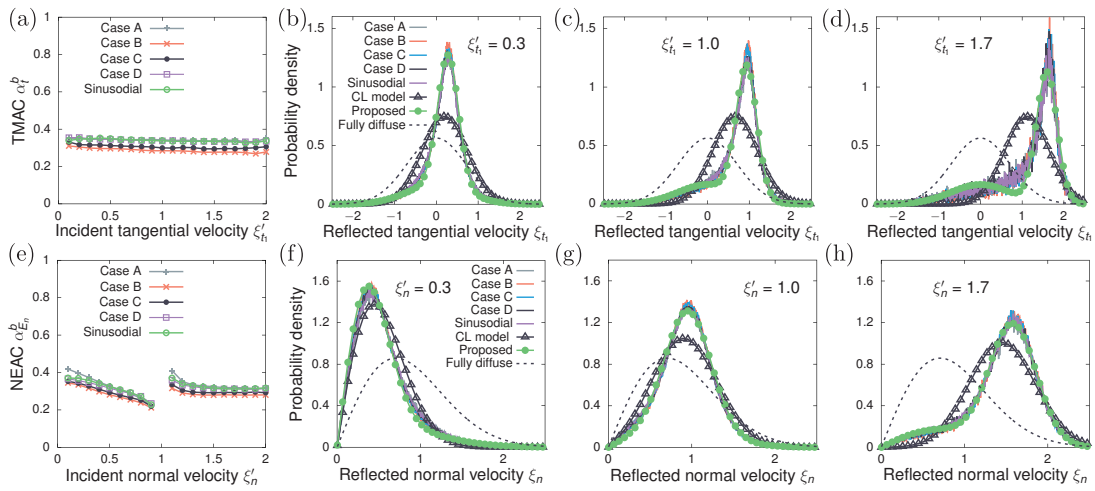

Figure D.1: (a) Beam TMACs and (b-d) tangential reflected velocity distributions for representative monoenergetic beams in the He-Au system are displayed, all at an equilibrium surface temperature of 600 K, and are predicted by existing scattering models and explicit MD, under surface roughness spectra with diverse characteristics yet maintaining a consistent magnitude of DWF= 0.7. (e) Beam NEACs and (f-h) normal reflected velocity distributions are derived from the aforementioned MD systems. Velocities of the beams are normalised by the most probable speed $\sqrt{2RT}$.

Figs. D.1-D.3 show the scattering dynamics for the He-Au system at 600 K, and Ar-Pt system at 300 K and 600 K, respectively. Simulations are conducted on the same surfaces as described in Section 6.5.3, i.e., cases A-D and one sinusoidal rough surface with diverse spectra but the same PDWF = 0.7. For these results, three remarks are worth stressing. First, the temperature is insignificant on the roughness larger than the lattice structure, as further supported by the similar slope of general TMACs in Fig. 6.5. The temperature primarily affects the scattering dynamics through gas–phonon collisions, which are already accounted for in the framework of the CL model. Second, the Ar-Pt system displays a more evident velocity-dependence behaviour compared to He-Au, especially concerning the tangential velocity components. Yet,

one may reasonably expect that this dependence has minimal impact on the transport of low speed flows, provided the general ACs are accurately calibrated. Third, the performance of the proposed model decrease in the context of the Ar-Pt system. Although appearing smooth, the Ar-Pt system still displays minor PES corrugations due to small σ, leading to the so-called classical rainbow scattering (Billing, 2000; Goodman & Wachman, 1976; Manson & Miret-Artés, 2022); the resulting effects can be incorporated, albeit introducing additional complexity to the proposed SK model.

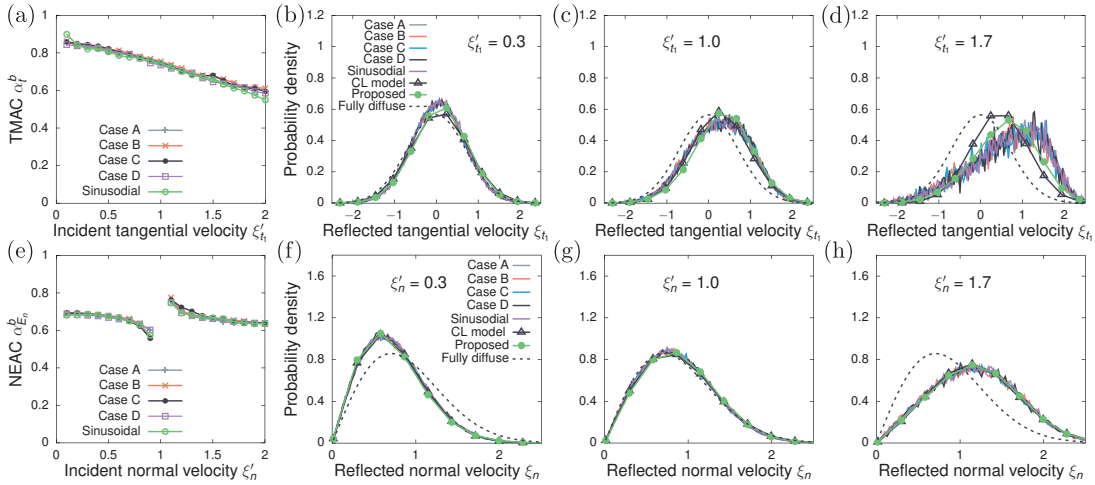

Figure D.2: (a) Beam TMACs and (b-d) tangential reflected velocity distributions for representative monoenergetic beams in the Ar-Pt system are displayed, all at an equilibrium surface temperature of 300 K, and are predicted by existing scattering models and explicit MD, under surface roughness spectra with diverse characteristics yet maintaining a consistent magnitude of DWF= 0.7. (e) Beam NEACs and (f-h) normal reflected velocity distributions are derived from the aforementioned MD systems. Velocities of the beams are normalised by the most probable speed $\sqrt{2RT}$.

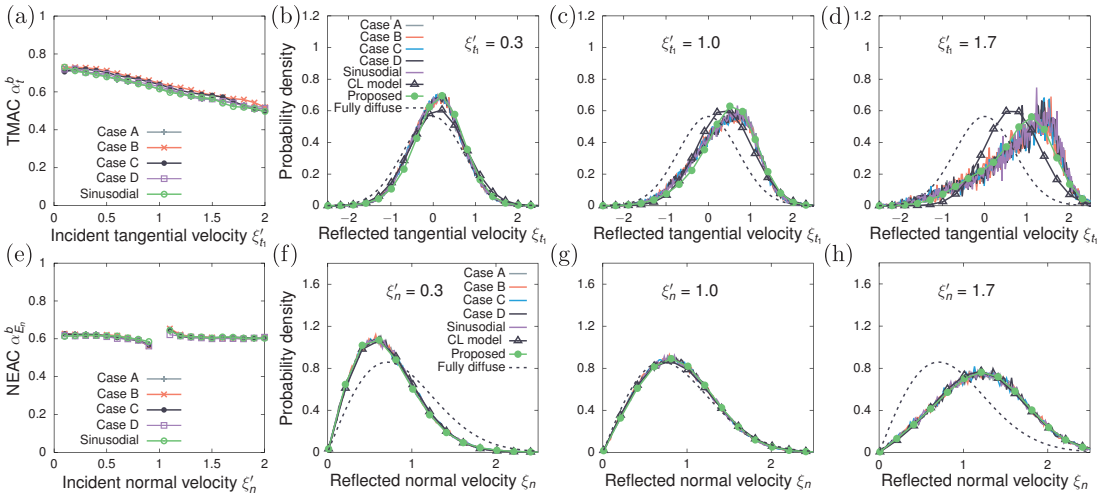

Figure D.3: (a) Beam TMACs and (b-d) tangential reflected velocity distributions for representative monoenergetic beams in the Ar-Pt system are displayed, all at an equilibrium surface temperature of 600 K, and are predicted by existing scattering models and explicit MD, under surface roughness spectra with diverse characteristics yet maintaining a consistent magnitude of DWF= 0.7. (e) Beam NEACs and (f-h) normal reflected velocity distributions are derived from the aforementioned MD systems. Velocities of the beams are normalised by the most probable speed $\sqrt{2RT}$.

References

Agrawal, A. & Prabhu, S. (2008). Survey on measurement of tangential momentum accommodation coefficient. *J. Vac. Sci. Technol. A*, *26*(4), 634–645.

Allen, M. P. & Tildesley, D. J. (2017). *Computer Simulation of Liquids.* Oxford University Press.

Aoki, K., Charrier, P. & Degond, P. (2011). A hierarchy of models related to nanoflows and surface diffusion. *Kinet. Relat. Models*, *4*(1), 53-85.

Aoki, K. & Giovangigli, V. (2019). Kinetic model of adsorption on crystal surfaces. *Phys. Rev. E*, *99*(5), 052137.

Aoki, K. & Giovangigli, V. (2021). Kinetic theory of chemical reactions on crystal surfaces. *Phys. A: Stat. Mech. Appl.*, *565*, 125573.

Aoki, K., Giovangigli, V., Golse, F. & Kosuge, S. (2024). The physisorbate-layer problem arising in kinetic theory of gas–surface interaction. *J. Stat. Phys.*, *191*(5), 53.

Aoki, K., Giovangigli, V. & Kosuge, S. (2022). Boundary conditions for the Boltzmann equation from gas–surface interaction kinetic models. *Phys. Rev. E*, *106*(3), 035306.

Arkilic, E. B., Breuer, K. S. & Schmidt, M. A. (2001). Mass flow and tangential momentum accommodation in silicon micromachined channels. *J. Fluid Mech.*, *437*, 29–43.

Arya, G., Chang, H. & Maginn, E. J. (2003b). Molecular simulations of Knudsen wall-slip: effect of wall morphology. *Mol. Simul.*, *29*(10-11), 697–709.

Arya, G., Chang, H.-C. & Maginn, E. J. (2003a). Knudsen diffusivity of a hard sphere in a rough slit pore. *Phys. Rev. Lett.*, *91*(2), 026102.

Barker, J. A. & Auerbach, D. J. (1984). Gas–surface interactions and dynamics; thermal energy atomic and molecular beam studies. *Surf. Sci. Rep.*, *4*(1-2), 1–99.

Barth, J. V. (2000). Transport of adsorbates at metal surfaces: from thermal migration to hot precursors. *Surf. Sci. Rep.*, *40*(3-5), 75–149.

Bärwinkel, K. & Schippers, S. (1989). Nonreciprocity in noble-gas metal–surface scattering. *Prog. Astronaut. Aeronaut.*, *116*, 487–501.

Basdanis, T., Tatsios, G. & Valougeorgis, D. (2022). Gas–surface interaction in rarefied gas flows through long capillaries via the linearized Boltzmann equation with various boundary conditions. *Vacuum*, *202*, 111152.

Bass, F. G. & Fuks, I. M. (2013). *Wave Scattering from Statistically Rough Surfaces: International Series in Natural Philosophy* (Vol. 93). Elsevier.

Beeby, J. (1971). The scattering of helium atoms from surfaces. *J. Phys. C: Solid State Phys.*, *4*(18), L359.

Beeby, J. (1972). The scattering of atoms from surfaces: the one-phonon contribution. *J. Phys. C: Solid State Phys.*, *5*(24), 3438.

Beenakker, J., Borman, V. & Krylov, S. Y. (1994). Molecular transport in the nanometer regime. *Phys. Rev. Lett.*, *72*(4), 514.

Beenakker, J., Borman, V. & Krylov, S. Y. (1995). Molecular transport in subnanometer pores: zero-point energy, reduced dimensionality and quantum sieving. *Chem. Phys. Lett.*, *232*(4), 379–382.

Beenakker, J. & Krylov, S. Y. (1997). One-dimensional surface diffusion: Density dependence in a smooth potential. *J. Chem. Phys.*, *107*(10), 4015–4023.

Bergmann, P. G. & Lebowitz, J. L. (1955). New approach to nonequilibrium processes. *Phys. Rev.*, *99*(2), 578.

Bhatnagar, P. L., Gross, E. P. & Krook, M. (1954). A model for collision processes in gases. i. small amplitude processes in charged and neutral one-component systems. *Phys. Rev.*, *94*(3), 511.

Billing, G. D. (2000). *Dynamics of Molecule Surface Interaction.* John Wiley & Sons.

Bird, G. A. (1994). *Molecular Gas Dynamics and the Direct Simulation of Gas Flows.* Oxford University Press.

Blanchard, D. & Ligrani, P. (2007). Slip and accommodation coefficients from rarefaction and roughness in rotating microscale disk flows. *Phys. Fluids.*, *19*(6).

Blanchard, R. C. (1986). Rarefied flow lift-to-drag measurements of the shuttle orbiter. In *15th Congress of International Council of Aeronautical Sciences* (pp. 1421–1430).

Boltzmann, L. E. (1872). Further studies on the thermal equilibrium of gas molecules. In S. G. Brush & N. S. Hall (Eds.), *The Kinetic Theory of Gases. An Anthology of Classic Papers with Historical Commentary* (pp. 262–349). Imperial College Press.

Bora, C., Flater, E., Street, M., Redmond, J., Starr, M., Carpick, R. & Plesha, M. (2005). Multiscale roughness and modeling of mems interfaces. *Tribol. Lett.*, *19*, 37–48.

Borg, M. K., Lockerby, D. A. & Reese, J. M. (2014). The fade mass-stat: a technique for inserting or deleting particles in molecular dynamics simulations. *J. Chem. Phys.*, *140*(7).

Borg, M. K., Macpherson, G. B. & Reese, J. M. (2010). Controllers for imposing continuum-to-molecular boundary conditions in arbitrary fluid flow geometries. *Mol. Simul.*, *36*(10), 745–757.

Borman, V., Krylov, S. & Prosyanov, A. (1988). Theory of nonequilibrium phenomena at a gas-solid interface. *Sov. Phys. JETP*, *67*(10), 2110–2121.

Borman, V., Krylov, S. Y. & Prosyanov, A. (1990). Fundamental role of unbound surface particles in transport phenomena along a gas-solid interface. *Sov. Phys. JETP*, *70*(6), 1013–1022.

Bousige, C., Ghimbeu, C. M., Vix-Guterl, C., Pomerantz, A. E., Suleimenova, A., Vaughan, G., ... others (2016). Realistic molecular model of kerogen's nanostructure. *Nat. Mater.*, *15*(5), 576–582.

Box, G. E. & Muller, M. E. (1958). A note on the generation of random normal deviates. *Ann. Math. Statist.*, *29*(2), 610–611.

Brancher, R. D., Stefanov, S., Graur, I. & Frezzotti, A. (2020). A kinetic model for gas adsorption-desorption at solid surfaces under non-equilibrium conditions. *Vacuum*, *174*, 109166.

Brull, S., Charrier, P. & Mieussens, L. (2013). Gas–surface interaction and boundary conditions for the Boltzmann equation. *arXiv preprint arXiv:1306.4309*.

Brull, S., Charrier, P. & Mieussens, L. (2014). Gas–surface interaction and boundary conditions for the Boltzmann equation. *Kinet. Relat. Models*, 7(2), 219-251.

Brull, S., Charrier, P. & Mieussens, L. (2016). Nanoscale roughness effect on Maxwell-like boundary conditions for the Boltzmann equation. *Phys. Fluids*, *28*(8), 082004.

Brunauer, S., Emmett, P. H. & Teller, E. (1938). Adsorption of gases in multimolecular layers. *J. Am. Chem. Soc.*, *60*(2), 309–319.

Bruno, D., Cacciatore, M., Longo, S. & Rutigliano, M. (2000). Gas–surface scattering models for particle fluid dynamics: a comparison between analytical approximate models and molecular dynamics calculations. *Chem. Phys. Lett.*, *320*(3-4), 245–254.

Butt, H., Graf, K. & Kappl, M. (2003). Adsorption. In *Physics and Chemistry of Interfaces* (p. 177-205). John Wiley & Sons, Ltd.

Cao, B., Chen, M. & Guo, Z. (2005). Temperature dependence of the tangential momentum accommodation coefficient for gases. *Appl. Phys. Lett.*, *86*(9), 091905.

Cao, B., Sun, J., Chen, M. & Guo, Z. (2009). Molecular momentum transport at fluid–solid interfaces in MEMS/NEMS: a review. *Int. J. Mol. Sci.*, *10*(11), 4638–4706.

Cao, B.-Y., Chen, M. & Guo, Z.-Y. (2006). Effect of surface roughness on gas flow in microchannels by molecular dynamics simulation. *Int. J. Eng. Sci.*, *44*(13-14), 927–937.

Cardillo, M. J. (1981). Gas–surface interactions studied with molecular beam techniques. *Annu. Rev. Phys. Chem.*, *32*(1), 331–357.

Celestini, F. & Mortessagne, F. (2008). Cosine law at the atomic scale: toward realistic simulations of Knudsen diffusion. *Phys. Rev. E*, *77*(2), 021202.

Cercignani, C. (1969). *Mathematical Methods in Kinetic Theory* (Vol. 1). Springer.

Cercignani, C. (1972). Scattering kernels for gas–surface interactions. *Transp. Theory Stat. Phys.*, *2*(1), 27–53.

Cercignani, C. (1988). The Boltzmann Equation and Its Applications. Springer.

Cercignani, C. (1989). Kinetic theory with "bounce-back" boundary conditions. *Transp. Theory Stat. Phys.*, *18*(1), 125–131.

Cercignani, C. (2000). *Rarefied Gas Dynamics: From Basic Concepts to Actual Calculations.* Cambridge University Press.

Cercignani, C. (2003). Ivan kuščer and gas–surface interaction. *Transp. Theory Stat. Phys.*, *32*(3-4), 215–226.

Cercignani, C. & Lampis, M. (1971). Kinetic models for gas–surface interactions. *Transp. Theory Stat. Phys.*, *1*(2), 101–114.

Chapman, S. & Cowling, T. G. (1952). *The Mathematical Theory of Non-Uniform Gases.* Cambridge University Press.

Chen, G. (2005). *Nanoscale Energy Transport and Conversion: A Parallel Treatment of Electrons, Molecules, Phonons, and Photons.* Oxford University Press.

Chen, Y., Gibelli, L., Li, J. & Borg, M. K. (2023). Impact of surface physisorption on gas scattering dynamics. *J. Fluid Mech.*, *968*, A4.

Chen, Y., Li, J., Datta, S., Docherty, S. Y., Gibelli, L. & Borg, M. K. (2022). Methane scattering on porous kerogen surfaces and its impact on mesopore transport in shale. *Fuel*, *316*, 123259.

Chew, A. D. (2009). Comment on "Survey on measurement of tangential momentum accommodation coefficient"[J. Vac. Sci. Technol. A 26, 634 (2008)]. *J. Vac. Sci. Technol. A*, *27*(3), 591–592.

Corral-Casas, C., Chen, Y., Borg, M. K. & Gibelli, L. (2024). Density and confinement effects on fluid velocity slip. *Phys. Rev. Fluids*, *9*(3), 034201.

Corral-Casas, C., Gibelli, L., Borg, M. K., Li, J., Al-Afnan, S. F. & Zhang, Y. (2021). Self-diffusivity of dense confined fluids. *Phys. Fluids*, *33*(8), 082009.

Corral-Casas, C., Li, J., Borg, M. K. & Gibelli, L. (2022). Knudsen minimum disappearance in molecular-confined flows. *J. Fluid Mech.*, *945*, A28.

Cowling, T. (1974). On the Cercignani–Lampis formula for gas–surface interactions. *J. Phys. D Appl. Phys.*, *7*(6), 781.

Dadzie, S. K. & Méolans, J. G. (2004). Anisotropic scattering kernel: Generalized and modified Maxwell boundary conditions. *J. Math. Phys.*, *45*(5), 1804–1819.

Darabi, H., Ettehad, A., Javadpour, F. & Sepehrnoori, K. (2012). Gas flow in ultra-tight shale strata. *J. Fluid Mech.*, *710*, 641–658.

Darrozes, J. & Guiraud, J. (1966). Généralisation formelle du théorème H en présence de parois. applications. *Comptes rendus hebdomadaires des séances de l'Académie des sciences série A*, *262*(24), 1368.

Deng, J., Zhang, J., Liang, T., Zhao, J., Li, Z. & Wen, D. (2022). A modified Cercignani–Lampis model with independent momentum and thermal accommodation coefficients for gas molecules scattering on surfaces. *Phys. Fluids*, *34*(10).

Epstein, M. (1967). A model of the wall boundary condition in kinetic theory. *AIAA J.*, *5*(10), 1797–1800.

Falk, K., Coasne, B., Pellenq, R., Ulm, F.-J. & Bocquet, L. (2015). Subcontinuum mass transport of condensed hydrocarbons in nanoporous media. *Nat. Commun.*, *6*(1), 1–7.

Finger, G. W., Kapat, J. S. & Bhattacharya, A. (2007). Molecular dynamics simulation of adsorbent layer effect on tangential momentum accommodation coefficient. *J. Fluids Eng.*, *129*(1), 31–39.

Freeman, C., Moridis, G. & Blasingame, T. (2011). A numerical study of microscale flow behavior in tight gas and shale gas reservoir systems. *Transp. Porous Media*, *90*(1), 253–268.

Freundlich, H. (1922). *Kapillarchemie: eine Darstellung der Chemie der Kolloide und verwandter Gebiete*. akademische Verlagsgesellschaft.

Frezzotti, A. & Gibelli, L. (2008). A kinetic model for fluid–wall interaction. *Proc. Inst. Mech. Eng. Pt. C J. Mechan. Eng. Sci.*, *222*(5), 787–795.

Gad-el Hak, M. (1999). The Fluid Mechanics of Microdevices—The Freeman Scholar Lecture. *J. Fluids Eng.*, *121*(1), 5-33.

Gallis, M. A., Torczynski, J. R., Plimpton, S. J., Rader, D. J. & Koehler, T. (2014). Direct simulation Monte Carlo: The quest for speed. *AIP Conf. Proc*, *1628*(1), 27-36.

Glauber, R. J. (1955). Time-dependent displacement correlations and inelastic scattering by crystals. *Phys. Rev.*, *98*(6), 1692.

Goldberger, M. L. & Watson, K. M. (2004). *Collision Theory*. Courier Corporation.

Goodman, F. O. (1971). Review of the theory of the scattering of gas atoms by solid surfaces. *Surf. Sci.*, *26*(1), 327–362.

Goodman, F. O. (1974). Thermal accommodation. *Prog. Surf. Sci.*, *5*, 261–375.

Goodman, F. O. (1977). On the use of a Debye-Waller-type factor in gas–surface scattering theory. *Surf. Sci.*, *65*(1), 37–40.

Goodman, F. O. & Wachman, H. Y. (1976). *Dynamics of Gas–Surface Scattering*. Academic Press, New York.

Gorji, M. H. & Jenny, P. (2014). A gas–surface interaction kernel for diatomic rarefied gas flows based on the Cercignani-Lampis-Lord model. *Phys. Fluids*, *26*(12), 122004.

Graur, I., Perrier, P., Ghozlani, W. & Méolans, J. G. (2009). Measurements of tangential momentum accommodation coefficient for various gases in plane microchannel. *Phys. Fluids*, *21*(10).

Gui, C., Elwenspoek, M., Tas, N. & Gardeniers, J. G. (1999). The effect of surface roughness on direct wafer bonding. *J. Appl. Phys.*, *85*(10), 7448–7454.

Guo, C., Xu, J., Wu, K., Wei, M. & Liu, S. (2015). Study on gas flow through nano pores of shale gas reservoirs. *Fuel*, *143*, 107–117.

Hadjiconstantinou, N. G. (2024). Molecular mechanics of liquid and gas slip flow. *Annu. Rev. Fluid Mech.*, *56*, 435–461.

Ho, M. T., Zhu, L., Wu, L., Wang, P., Guo, Z., Ma, J. & Zhang, Y. (2019). Pore-scale simulations of rarefied gas flows in ultra-tight porous media. *Fuel*, *249*, 341–351.

Huang, X., Gu, L., Li, S., Du, Y. & Liu, Y. (2022). Absolute adsorption of light hydrocarbons on organic-rich shale: An efficient determination method. *Fuel*, *308*, 121998.

Hurlbut, F. & Sherman, F. (1968). Application of the nocilla wall reflection model to free-molecule kinetic theory. *Phys. Fluids*, *11*(3), 486–496.

Jin, Z. & Firoozabadi, A. (2015). Flow of methane in shale nanopores at low and high pressure by molecular dynamics simulations. *J. Chem. Phys.*, *143*(10), 104315.

Karniadakis, G., Beskok, A. & Aluru, N. (2005). *Microflows and Nanoflows: Fundamentals and Simulation* (Vol. 29). Springer Science & Business Media.

Kittel, C. (2005). *Introduction to Solid State Physics*. John Wiley & Sons, Inc.

Klinc, T. & Kuščer, I. (1972). Slip coefficients for general gas–surface interaction. *Phys. Fluids*, *15*(6), 1018–1022.

Knudsen, M. (1911). Die molekulare wärmeleitung der gase und der akkommodationskoeffizient. *Annalen der Physik*, *339*(4), 593–656.

Knudsen, M. (1934). *The Kinetic Theory of Gases: Some Modern Aspects*. London, Methuen.

Kogan, M. N. (1969). *Rarefied Gas Dynamics*. Plenum Press, New York.

Kremer, G. M. (2010). *An Introduction to the Boltzmann Equation and Transport Processes in Gases*. Springer Science & Business Media.

Krivoglaz, M. A. (1967). *Teoriya Rasseyaniya Rentgenovskih Lučei i Teplovyh Neitronov real'nymi Kristallami*. Nauka.

Krylov, S. Y. (2003). Molecular transport in sub-nano-scale systems. *AIP Conf. Proc.*, *663*(1), 735-742.

Krylov, S. Y., Beenakker, J. & Tringides, M. (1999). On the theory of surface diffusion: kinetic versus lattice gas approach. *Surf. Sci.*, *420*(2-3), 233–249.

Krylov, S. Y., Prosyanov, A. & Beenakker, J. (1997). One dimensional surface diffusion. ii. density dependence in a corrugated potential. *J. Chem. Phys.*, *107*(17), 6970–6979.

Kundt, A. & Warburg, E. (1875). Ueber reibung und wärmeleitung verdünnter gase. *Annalen der Physik*, *232*(10), 177-211.

Kuščer, I. (1971). Reciprocity in scattering of gas molecules by surfaces. *Surf. Sci.*, *25*(2), 225–237.

Kuščer, I. (1978). Phenomenological aspects of gas–surface interaction. In E. Cohen & W. Fiszdon (Eds.), *Fundamental Problems in Statistical Mechanics IV* (pp. 441–467). Ossolineum, Warsaw.

Kuščer, I. & Vidav, I. (1975). Properties of surface scattering operators. *Zeitschrift für angewandte Mathematik und Physik ZAMP*, *26*(2), 165–170.

Kuščer, I. (1974). Phenomenology of gas–surface accommodation. In M. Becker & M. Fiebig (Eds.), *9th International Symposium on Rarefied Gas Dynamics* (p. E.1-1-21).

Kuščer, I., Mozina, J. & Krizamič, F. (1971). The Knudsen model of thermal accommodation. In D. Dini, C. Cercignani & S. Nocilla (Eds.), *7th International Symposium on Rarefied Gas Dynamics* (p. 97).

Landau, L. D. & Lifshitz, E. M. (2013). *Statistical Physics: Volume 5* (Vol. 5). Elsevier.

Langmuir, I. (1916). The constitution and fundamental properties of solids and liquids. Part I. solids. *J. Am. Chem. Soc.*, *38*(11), 2221–2295.

Lebowitz, J., Frisch, H. & Helfand, E. (1960). Nonequilibrium distribution functions in a fluid. *Phys. Fluids*, *3*(3), 325–338.

Lebowitz, J. L. & Bergmann, P. G. (1957). Irreversible gibbsian ensembles. *Ann. Phys.*, *1*(1), 1–23.

Lebowitz, J. L. & Frisch, H. L. (1957). Model of nonequilibrium ensemble: Knudsen gas. *Phys. Rev.*, *107*(4), 917.

Li, J. (2019). Efficient prediction of gas permeability by hybrid DSBGK-LBM simulations. *Fuel*, *250*, 154–159.

Li, J., Ho, M. T., Borg, M. K., Cai, C., Li, Z.-H. & Zhang, Y. (2021). Pore-scale gas flow simulations by the DSBGK and DVM methods. *Comput. Fluids*, 105017.

Liang, T. & Li, Q. (2019). Accurate modeling of Knudsen diffusion in nanopores using a physical-based boundary model. *J. Appl. Phys.*, *126*(8), 084304.

Liang, T., Li, Q. & Ye, W. (2018). A physical-based gas–surface interaction model for rarefied gas flow simulation. *J. Comput. Phys.*, *352*, 105–122.

Liao, M., Grenier, R., To, Q., de Lara-Castells, M. & Leonard, C. (2018). Helium and argon interactions with gold surfaces: Ab initio-assisted determination of the He–Au pairwise potential and its application to accommodation coefficient determination. *J. Phys. Chem. C*, *122*(26), 14606–14614.

Liu, Y., Hou, J. & Wang, C. (2020). Absolute adsorption of CH4 on shale with the simplified local-density theory. *SPE Journal*, *25*(01), 212–225.

Livadiotti, S., Crisp, N. H., Roberts, P. C., Worrall, S. D., Oiko, V. T., Edmondson, S., ... others (2020). A review of gas–surface interaction models for orbital aerodynamics applications. *Prog. Aerosp. Sci.*, *119*, 100675.

Logan, R. M. & Keck, J. C. (1968). Classical theory for the interaction of gas atoms with solid surfaces. *J. Chem. Phys.*, *49*(2), 860–876.

Logan, R. M. & Stickney, R. (1966). Simple classical model for the scattering of gas atoms from a solid surface. *J. Chem. Phys.*, *44*(1), 195–201.

Lord, R. G. (1991). Some extensions to the Cercignani–Lampis gas–surface scattering kernel. *Phys. Fluids A*, *3*(4), 706–710.

Lord, R. G. (1995). Some further extensions of the Cercignani–Lampis gas–surface interaction model. *Phys. Fluids*, *7*(5), 1159–1161.

Ma, J., Sanchez, J. P., Wu, K., Couples, G. D. & Jiang, Z. (2014). A pore network model for simulating non-ideal gas flow in micro-and nano-porous materials. *Fuel*, *116*, 498–508.

Manson, J. & Miret-Artés, S. (2022). Atom–surface scattering in the classical multiphonon regime. *Phys. Chem. Chem. Phys.*, *24*(28), 16942–16972.

Martini, A., Roxin, A., Snurr, R. Q., Wang, Q. & Lichter, S. (2008). Molecular mechanisms of liquid slip. *J. Fluid Mech.*, *600*, 257–269.

Maxwell, J. C. (1879). VII. On stresses in rarefied gases arising from inequalities of temperature. *Phil. Trans. R. Soc. Lond.*(170), 231–256.

Menzel, D. & Kouptsidis, J. (1974). Energy transfer by single collisions and by trapping in thermal accommodation. In M. Becker & M. Fiebig (Eds.), *9th International Symposium on Rarefied Gas Dynamics* (p. E.14-1-11).

Méolans, J. G. & Dadzie, S. K. (2005). Scattering kernel for polyatomic molecules. *J. Math. Phys.*, *46*(6).

Miret-Artés, S. & Pollak, E. (2012). Classical theory of atom–surface scattering: The rainbow effect. *Surf. Sci. Rep.*, *67*(7-8), 161–200.

Moghaddam, R. N. & Jamiolahmady, M. (2017). Study of slip flow in unconventional shale rocks using lattice Boltzmann method: Effects of boundary conditions and TMAC. *Transp. Porous Media*, *120*(1), 115–139.

Muiño, R. D. & Busnengo, H. F. (2013). *Dynamics of Gas–Surface Interactions.* Springer.

Myong, R. S. (2004). Gaseous slip models based on the Langmuir adsorption isotherm. *Phys. Fluids*, *16*(1), 104–117.

Nejad, S. M., Nedea, S., Frijns, A. & Smeulders, D. (2020). The influence of gas–wall and gas–gas interactions on the accommodation coefficients for rarefied gases: A molecular dynamics study. *Micromachines*, *11*(3), 319.

Nocilla, S. (1961). On the interaction between stream and body in free-molecule flow. In L. Talbot (Ed.), *2nd International Symposium on Rarefied Gas Dynamics* (p. 169-207).

Nocilla, S. (1963). The surface re-emission law in free-molecule flow. In J. A. Laurmann (Ed.), *3rd International Symposium on Rarefied Gas Dynamics* (Vol. 1, p. 327-346).

Obliger, A., Ulm, F.-J. & Pellenq, R. (2018). Impact of nanoporosity on hydrocarbon transport in shales' organic matter. *Nano Lett.*, *18*(2), 832–837.

Ohwada, T., Sone, Y. & Aoki, K. (1989). Numerical analysis of the poiseuille and thermal transpiration flows between two parallel plates on the basis of the Boltzmann equation for hard-sphere molecules. *Phys. Fluids A*, *1*(12), 2042–2049.

Ozhgibesov, M., Leu, T., Cheng, C. & Utkin, A. (2013). Studies on argon collisions with smooth and rough tungsten surfaces. *J. Mol. Graph. Model.*, *45*, 45–49.

Péraud, J.-P. M. & Hadjiconstantinou, N. G. (2011). Efficient simulation of multidimensional phonon transport using energy-based variance-reduced Monte Carlo formulations. *Phys. Rev. B*, *84*(20), 205331.

Perrier, P., Hadj-Nacer, M., Méolans, J. G. & Graur, I. (2019). Measurements and modeling of the gas flow in a microchannel: influence of aspect ratios, surface nature, and roughnesses. *Microfluid. Nanofluidics*, *23*(8), 97.

Persson, B. N., Albohr, O., Tartaglino, U., Volokitin, A. & Tosatti, E. (2004). On the nature of surface roughness with application to contact mechanics, sealing, rubber friction and adhesion. *J. Phys. Condens. Matter*, *17*(1), R1.

Pilinski, M. D., Argrow, B. M., Palo, S. E. & Bowman, B. R. (2013). Semi-empirical satellite accommodation model for spherical and randomly tumbling objects. *J. Spacecraft Rockets.*, *50*(3), 556–571.

Plimpton, S. (1995). Fast parallel algorithms for short-range molecular dynamics. *J. Comput. Phys.*, *117*(1), 1–19.

Rettner, C., Auerbach, D., Tully, J. & Kleyn, A. (1996). Chemical dynamics at the gas–surface interface. *J. Phys. Chem.*, *100*(31), 13021–13033.

Rettner, C. T., Schweizer, E. K. & Mullins, C. B. (1989). Desorption and trapping of argon at a 2H–W (100) surface and a test of the applicability of detailed balance to a nonequilibrium system. *J. Chem. Phys.*, *90*(7), 3800–3813.

Saltsburg, H. & Smith Jr, J. N. (1966). Molecular-beam scattering from the (111) plane of silver. *J. Chem. Phys.*, *45*(6), 2175–2183.

Sazhin, O. V., Borisov, S. F. & Sharipov, F. (2001). Accommodation coefficient of tangential momentum on atomically clean and contaminated surfaces. *J. Vac. Sci. Technol. A*, *19*(5), 2499–2503.

Seidl, M. & Steinheil, E. (1974). Measurement of momentum accommodation coefficients on surfaces characterized by auger spectroscopy, sims and leed. In M. Becker & M. Fiebig (Eds.), *9th International Symposium on Rarefied Gas Dynamics* (p. E9.1-E9.12).

Shan, B., Su, W., Gibelli, L. & Zhang, Y. (2023). Molecular kinetic modelling of non-equilibrium transport of confined van der Waals fluids. *J. Fluid Mech.*, *976*, A7.

Shan, B., Wang, P., Wang, R., Zhang, Y. & Guo, Z. (2022). Molecular kinetic modelling of nanoscale slip flow using a continuum approach. *J. Fluid Mech.*, *939*.

Shan, B., Wang, R., Guo, Z. & Wang, P. (2021). Contribution quantification of nanoscale gas transport in shale based on strongly inhomogeneous kinetic model. *Energy*, *228*, 120545.

Sharipov, F. (2002). Application of the Cercignani–Lampis scattering kernel to calculations of rarefied gas flows. i. plane flow between two parallel plates. *Eur. J. Mech. B Fluids*, *21*(1), 113–123.

Sharipov, F. (2003). Application of the Cercignani–Lampis scattering kernel to calculations of rarefied gas flows. ii. slip and jump coefficients. *Eur. J. Mech. B Fluids*, *22*(2), 133–143.

Sharipov, F. (2015). *Rarefied Gas Dynamics: Fundamentals for Research and Practice*. John Wiley & Sons.

Sharipov, F. & Moldover, M. R. (2016). Energy accommodation coefficient extracted from acoustic resonator experiments. *J. Vac. Sci. Technol. A*, *34*(6).

Sharipov, F. & Seleznev, V. (1998). Data on internal rarefied gas flows. *J. Phys. Chem. Ref. Data*, *27*(3), 657–706.

Shen, C. (2006). *Rarefied Gas Dynamics: Fundamentals, Simulations and Micro Flows*. Springer Science & Business Media.

Shen, S. & Kuščer, I. (1971). Symmetry of accommodation coefficients and the parametric representation of gas–surface interaction. In D. Dini, C. Cercignani & S. Nocilla (Eds.), *7th International Symposium on Rarefied Gas Dynamics* (p. 109).

Sheng, Q., Gibelli, L., Li, J., Borg, M. K. & Zhang, Y. (2020). Dense gas flow simulations in ultra-tight confinement. *Phys. Fluids*, *32*(9), 092003.

Simon, S. H. (2013). *The Oxford Solid State Basics*. Oxford University Press.

Smoluchowski, M. (1898). XIV. On conduction of heat by rarefied gases. *The London, Edinburgh, and Dublin Philosophical Magazine and Journal of Science*, *46*(279), 192-206.

Sofos, F. D., Karakasidis, T. E. & Liakopoulos, A. (2009). Effects of wall roughness on flow in nanochannels. *Phys. Rev. E*, *79*(2), 026305.

Sone, Y. (2007). *Molecular Gas Dynamics: Theory, Techniques, and Applications*. Boston, MA: Birkhäuser Boston.

Spijker, P., Markvoort, A. J., Nedea, S. V. & Hilbers, P. A. (2010). Computation of accommodation coefficients and the use of velocity correlation profiles in molecular dynamics simulations. *Phys. Rev. E*, *81*(1), 011203.

Stacy, L. J. (1923). A determination by the constant deflection method of the value of the coefficient of slip for rough and for smooth surfaces in air. *Phys. Rev.*, *21*(3), 239.

Struchtrup, H. (2005). *Macroscopic Transport Equations for Rarefied Gas Flows*. Springer Berlin Heidelberg.

Struchtrup, H. (2013). Maxwell boundary condition and velocity dependent accommodation coefficient. *Phys. Fluids*, *25*(11), 112001.

Su, W., Liu, H., Zhang, Y. & Wu, L. (2017). Rarefaction cloaking: Influence of the fractal rough surface in gas slider bearings. *Phys. Fluids.*, *29*(10), 102003.

Sun, H. & Faghri, M. (2003). Effect of surface roughness on nitrogen flow in a microchannel using the direct simulation Monte Carlo method. *Numer. Heat Transf.; A: Appl.*, *43*(1), 1–8.

Sun, J. & Li, Z.-X. (2008). Effect of gas adsorption on momentum accommodation coefficients in microgas flows using molecular dynamic simulations. *Mol. Phys.*, *106*(19), 2325–2332.

Sun, J. & Li, Z.-X. (2011). Three-dimensional molecular dynamic study on accommodation coefficients in rough nanochannels. *Heat Transf. Eng.*, *32*(7-8), 658–666.

Swope, W. C., Andersen, H. C., Berens, P. H. & Wilson, K. R. (1982). A computer simulation method for the calculation of equilibrium constants for the formation of physical clusters of molecules: Application to small water clusters. *J. Chem. Phys.*, *76*(1), 637–649.

Székely, L. & Guttman, A. (2005). New advances in microchip fabrication for electrochromatography. *Electrophoresis*, *26*(24), 4590–4604.

Takata, S., Akasobe, S. & Hattori, M. (2021). A revisit to the Cercignani–Lampis model: Langevin picture and its numerical simulation. In *Recent Advances in Kinetic Equations and Applications* (pp. 345–365).

Thomas, L. & Lord, R. (1974). Comparative measurements of tangential momentum and thermal accommodations on polished and on roughened steel spheres. In K. Karamcheti (Ed.), *8th International Symposium on Rarefied Gas Dynamics* (p. 405-412).

Trott, W. M., Castañeda, J. N., Torczynski, J. R., Gallis, M. A. & Rader, D. J. (2011). An experimental assembly for precise measurement of thermal accommodation coefficients. *Rev. Sci. Instrum.*, *82*(3).

Tully, J. C. (1980). Theories of the dynamics of inelastic and reactive processes at surfaces. *Annu. Rev. Phys. Chem.*, *31*(1), 319–343.

Tully, J. C. (1990). Washboard model of gas–surface scattering. *J. Chem. Phys.*, *92*(1), 680–686.

Tysanner, M. W. & Garcia, A. L. (2004). Measurement bias of fluid velocity in molecular simulations. *J. Comput. Phys.*, *196*(1), 173–183.

Vincenti, W. G. & Kruger, C. H. (1965). *Introduction to Physical Gas Dynamics.* New York: Wiley.

Waldmann, L. (1977). Theory of boundary conditions for the Boltzmann equation. *Zeitschrift für Naturforschung A*, *32*(6), 521–531.

Wang, G. J. & Hadjiconstantinou, N. G. (2019). Universal molecular-kinetic scaling relation for slip of a simple fluid at a solid boundary. *Phys. Rev. Fluids*, *4*(6), 064201.

Wang, J., Chen, L., Kang, Q. & Rahman, S. S. (2016). The lattice Boltzmann method for isothermal micro-gaseous flow and its application in shale gas flow: A review. *Int. J. Heat Mass Transf.*, *95*, 94–108.

Wang, P., Ho, M. T., Wu, L., Guo, Z. & Zhang, Y. (2018). A comparative study of discrete velocity methods for low-speed rarefied gas flows. *Comput. Fluids*, *161*, 33–46.

Wang, R., Datta, S., Li, J., Al-Afnan, S. F., Gibelli, L. & Borg, M. K. (2023). Interfacial adsorption kinetics of methane in microporous kerogen. *Langmuir*, *39*(10), 3742–3751.

Wang, R., Li, J., Gibelli, L., Guo, Z. & Borg, M. K. (2021). Sub-nanometre pore adsorption of methane in kerogen. *Chem. Eng. J.*, *426*, 130984.

Wang, S., Javadpour, F. & Feng, Q. (2016a). Fast mass transport of oil and supercritical carbon dioxide through organic nanopores in shale. *Fuel*, *181*, 741–758.

Wang, S., Javadpour, F. & Feng, Q. (2016b). Molecular dynamics simulations of oil transport through inorganic nanopores in shale. *Fuel*, *171*, 74–86.

Welander, P. (1954). On the temperature jump in a rarefied gas. *Ark. Fys.*, 7, 507–553.

Wenski, T. E., Olson, T., Rettner, C. T. & Garcia, A. L. (1998, 07). Simulations of air slider bearings with realistic gas–surface scattering. *J. Tribol.*, *120*(3), 639-641.

Williams, M. (1971). A phenomenological study of gas–surface interactions. *J. Phys. D Appl. Phys.*, *4*(9), 1315.

Wu, L., Ho, M. T., Germanou, L., Gu, X.-J., Liu, C., Xu, K. & Zhang, Y. (2017). On the apparent permeability of porous media in rarefied gas flows. *J. Fluid Mech.*, *822*, 398–417.

Wu, L., Liu, H., Reese, J. M. & Zhang, Y. (2016). Non-equilibrium dynamics of dense gas under tight confinement. *J. Fluid Mech.*, *794*, 252–266.

Wu, L. & Struchtrup, H. (2017). Assessment and development of the gas kinetic boundary condition for the Boltzmann equation. *J. Fluid Mech.*, *823*, 511–537.

Yakunchikov, A., Kovalev, V. & Utyuzhnikov, S. (2012). Analysis of gas–surface scattering models based on computational molecular dynamics. *Chem. Phys. Lett.*, *554*, 225–230.

Yamaguchi, H., Hanawa, T., Yamamoto, O., Matsuda, Y., Egami, Y. & Niimi, T. (2011). Experimental measurement on tangential momentum accommodation coefficient in a single microtube. *Microfluid. Nanofluidics*, *11*, 57–64.

Yamamoto, K., Takeuchi, H. & Hyakutake, T. (2006). Characteristics of reflected gas molecules at a solid surface. *Phys. Fluids*, *18*(4), 046103.

Yamamoto, K., Takeuchi, H. & Hyakutake, T. (2007). Scattering properties and scattering kernel based on the molecular dynamics analysis of gas-wall interaction. *Phys. Fluids*, *19*(8), 087102.

Yamanishi, N., Matsumoto, Y. & Shobatake, K. (1999). Multistage gas–surface interaction model for the direct simulation Monte Carlo method. *Phys. Fluids*, *11*(11), 3540–3552.

Yang, Y., Wang, K., Zhang, L., Sun, H., Zhang, K. & Ma, J. (2019). Pore-scale simulation of shale oil flow based on pore network model. *Fuel*, *251*, 683–692.

Yu, H., Xu, H., Fan, J., Wang, F. & Wu, H. (2020). Roughness factor-dependent transport characteristic of shale gas through amorphous kerogen nanopores. *J. Phys. Chem. C*, *124*(23), 12752–12765.

Yu, H., Zhang, Y., Yang, F. & Li, H. (2020). Molecular dynamics study on scattering characteristics of nitrogen molecules from platinum surface by molecular beam method. *AIP Advances*, *10*(9), 095028.

Zhang, C., Chen, Y., Deng, Z. & Shi, M. (2012). Role of rough surface topography on gas slip flow in microchannels. *Phys. Rev. E*, *86*(1), 016319.

Zhang, L., Shan, B., Zhao, Y. & Guo, Z. (2019). Review of micro seepage mechanisms in shale gas reservoirs. *Int. J. Heat Mass Transf.*, *139*, 144–179.

Ziarani, A. S. & Aguilera, R. (2012). Knudsen's permeability correction for tight porous media. *Transp. Porous Media*, *91*(1), 239–260.